LONG WAVES GENERATION AND COASTAL AMPLIFICATION DUE TO ATMOSPHERIC PRESSURE DISTURBANCES

A THESIS SUBMITTED TO
THE GRADUATE SCHOOL OF NATURAL AND APPLIED SCIENCES
OF
MIDDLE EAST TECHNICAL UNIVERSITY

BY

AYŞE DUHA METİN

IN PARTIAL FULFILLMENT OF THE REQUIREMENTS
FOR
THE DEGREE OF MASTER OF SCIENCE
IN
CIVIL ENGINEERING

AUGUST 2016

Approval of the thesis:

LONG WAVES GENERATION AND COASTAL AMPLIFICATION DUE TO ATMOSPHERIC PRESSURE DISTURBANCES

submitted by **AYŞE DUHA METİN** in partial fulfillment of the requirements for the degree of **Master of Science in Civil Engineering Department, Middle East Technical University** by,

Prof. Dr. Gülbin Dural Ünver
Dean, Graduate School of **Natural and Applied Sciences** _____

Prof. Dr. İsmail Özgür Yaman
Head of Department, **Civil Engineering** _____

Prof. Dr. Ahmet Cevdet Yalçıner
Supervisor, **Civil Engineering Department, METU** _____

Assist. Prof. Dr. Gülizar Özyurt Tarakcıoğlu
Co-Supervisor, **Civil Engineering Department, METU** _____

Examining Committee Members:

Prof. Dr. Lale Balas _____
Civil Engineering Dept., Gazi University

Prof. Dr. Ahmet Cevdet Yalçıner _____
Civil Engineering Dept., METU

Assoc. Prof. Dr. Utku Kanoğlu _____
Engineering Science Dept., METU

Assist. Prof. Dr. Gülizar Özyurt Tarakcıoğlu _____
Civil Engineering Dept., METU

Assist. Prof. Dr. Cüneyt Baykal _____
Civil Engineering Dept., METU

Date: 12.08.2016

I hereby declare that all information in this document has been obtained and presented in accordance with academic rules and ethical conduct. I also declare that, as required by these rules and conduct, I have fully cited and referenced all material and results that are not original to this work.

Name, Last Name : Ayşe Duha Metin

Signature :

ABSTRACT

LONG WAVES GENERATION AND COASTAL AMPLIFICATION DUE TO ATMOSPHERIC PRESSURE DISTURBANCES

Metin, Ayşe Duha
M.S., Department of Civil Engineering
Supervisor: Prof. Dr. Ahmet Cevdet Yalçıner
Co-Supervisor: Assist. Prof. Dr. Gülizar Özyurt Tarakcıoğlu

August 2016, 88 pages

The cause of the occurrence of ebb or abnormal waves which are occasionally observed on the coasts is related to the spatial and temporal changes of atmospheric pressure. Because, low atmospheric pressure leads to static water level rise in a part of the marine area and high atmospheric pressure leads to static water level drop in another zone, water level throughout the entire marine area is deformed. This deformation moves as wave, sometimes amplifies on the shore. Due to the changes of atmospheric pressure, the respective small amplitude long waves propagate along the entire marine area. This type of waves can propagate through long distances and can also be amplified due to resonant effects in the enclosed basins and nearshore/offshore coastal morphology. The investigation of the amplification of the long-period waves which occurred by the spatial and temporal changes of atmospheric pressure is the one of the objectives of this study. For the different types of regular shaped basins, tests are conducted by numerical modeling solving nonlinear shallow water equations. In the tests, basins with flat, triangular, shelf, upward and downward sloping sections are simulated by using high pressure zone propagating with certain velocity (faster, equal or slower than wave velocity). The

change in the sea level is calculated and compared with the theoretical outcomes. Finally, the time histories of water surface fluctuations at selected numerical gauge points are computed in each simulation and compared to identify the effects of different bottom topographies on the amplification of long waves.

Keywords: Meteotsunami, atmospheric pressure disturbances, long waves, modeling, basin

ÖZ

ATMOSFERİK BASINÇ HAREKETLERİNE BAĞLI UZUN PERİYOTLU DALGALARIN OLUŞUMU VE KIYILARDA YÜKSELMELERİ

Metin, Ayşe Duha
Yüksek Lisans, İnşaat Mühendisliği Bölümü
Tez Yöneticisi: Prof. Dr. Ahmet Cevdet Yalçıner
Ortak Tez Yöneticisi: Assist. Prof. Dr. Gülizar Özyurt Tarakcıoğlu

Ağustos 2016, 88 sayfa

Kıyılarda zaman zaman gözlenen deniz çekilmeleri ya da olağan dışı dalgaların oluşma nedeni atmosferik basıncın alansal ve zamansal değişimleri ile ilgilidir. Deniz alanının bir kısmında düşük atmosferik basıncın su seviyesinde yükselmeye neden olması, bir başka alanda ise yüksek atmosferik basıncın su seviyesinde alçalmaya neden olması, bütün su yüzeyinde alansal deformasyona sebep olur. Bu deformasyon dalga olarak hareket eder, bazen kıyılarda büyür ve rüzgarsız ortamlarda daha belirgin olarak gözlenebilir. Atmosferik basıncın mekansal ve zamansal değişiminden dolayı, küçük genlikli uzun periyotlu dalgalar tüm deniz alanı boyunca ilerlerler. Bu tip dalgalar uzun mesafelerde ilerlerken, kapalı basenlerde, kıyıya yakın yerlerdeki ya da açık denizlerdeki morfolojide rezonans etkisiyle büyüyebilirler. Bu sebeple, kıyı alanlarında beklenmeyen davranışlar gösterebilirler. Atmosferik basınç farklılığından dolayı oluşan uzun periyotlu dalgaların, kıyıya doğru ilerlerken büyümesinin araştırılması bu çalışmanın başlıca odaklarından biridir. Diğer yandan atmosferik basıncın zamansal değişimi başka deyişle basıncın hareketi ile denizde oluşturduğu dalganın hareketi arasındaki ilişki de bu çalışmada incelenmiştir.

Farklı düzgün şekilli batimetrilerde, farklı derinlikteki test çalışmaları yürütülerek, doğrusal olmayan sığ su denklemleriyle sayısal çözümleme yapılmıştır. Bu test çalışmalarında düz tabanlı, üçgen kesitli, şelf, yükselen eğimli ve alçalan eğimli basenler, farklı basınç hızları (dalgadan yavaş basınç hızı, dalgaya eşit basınç hızı ve dalgadan hızlı basınç hızı) kullanılarak benzetimler yapılmıştır. Dalga özellikleri hesaplanarak kuramsal çözümlerle karşılaştırılmıştır. Her benzetimde belirlenen sayısal ölçüm noktalarında, su yüzeyindeki dalgalanmaların zaman geçmişleri hesaplanmıştır. Böylece, farklı deniz tabanı topoğrafyalarının, uzun periyotlu dalgaların büyümesi üzerindeki etkileri de araştırılmıştır.

Anahtar Kelimeler: Meteotsunami, atmosferik basınç hareketleri, uzun periyotlu dalgalar, modelleme, basen

< *to my beloved family* >

ACKNOWLEDGEMENTS

I would like to thank the many people who have supported me both academically and personally during my studies. First of all, I would like to express my great sincere gratitude to my supervisor, *Prof. Dr. Ahmet Cevdet Yalçıner*, for his guidance, patience and encouragement during my research. I am also grateful to him for giving me a chance to participate in international conferences (AGU and EGU) and give oral presentations. It means too much to me because these opportunities made me very self-confident in academy and caused to discover myself. He also taught me calmness, to be positive and problem solving person not only in academic but also in social life.

Special thanks to *Prof. Dr. Efim Pelinovsky* and *Dr. Andrey Zaytsev* for their significant contributions to my research and valuable collaboration.

I would also like to thank *Assist. Prof. Dr. Gülizar Özyurt Tarakcıoğlu* for her contribution to my studies and supports.

I am thankful to *Dr. Işıkhan Güler*, and *Assist. Prof. Dr. Cüneyt Baykal* for their contributions to my coastal and ocean engineering education background with their valuable experiences.

I particularly thank *Prof. Dr. Ayşen Ergin* for her guidance to notice the beauty of the nature, love the people and be a kind person. I am very proud of to be the one of the student of her.

I specially thank the members of the Coastal Engineering family, *Arif Kayışlı*, *Nuray Çimen* and *Yusuf Korkut* for their valuable support and sincerity.

The support I received from my dear friends *Ebru Demirci*, *Naeimeh Sharghivand*, *Çağıl Kirezci*, *Bora Yalçıner*, *Deniz Can Aydın*, *Gökhan Güler*, *Rozita Kian*, *Sena Acar* and *Güney Doğan* means a lot to me and I am really grateful to have such perfect friendships. I would also like to express my gratitude my officemate, *Nilay Doğulu*, for her support, experiences and patience. She is not only a friend for me but also sister with whom I spend most of the time.

Finally, I would like to express greatest thank my dear family for their support every step of my life. My mother, *Serap Metin*, always provides me with different perspective, keeps me focused on the important things and motivates me to be successful in life. Special thanks to her love, patience and support. My father, *Yaşar Temel Metin*, is my role model for his diligence and strength against to life. He supports my every decision and gives a chance to be a person who I am. I would also like to thank my brother, *Rıfat Furkan Metin*, for his love and belief to me. There are no words to express my gratitude to my family.

I would like to acknowledge that this study partly supported by the Scientific and Technological Research Council of Turkey (TÜBİTAK) Research Grant No: 213M534, "New Tools for Risk Assessment and Modeling of Marine Natural Hazards in the Coastlines of Black Sea".

TABLE OF CONTENTS

LIST OF TABLES

TABLES

LIST OF FIGURES

FIGURES

CHAPTER 1

INTRODUCTION

The word tsunami means harbor wave and it becomes a part of our language by Japanese after 1896 Meiji Sanriku earthquake and tsunami. In fact, Greek historian Thucydides (426 B.C.) described tsunami-like event in the Maliakos gulf of eastern Greece but he did not use specific word for this situation. Thucydides (n.d., as cited in Antonopoulos, 1992) stated that when earthquake was occurred, sea was withdrawn, then quickly receded along with devastating impact and inundation occurred. However, he was associated this tsunami-like event only with earthquake. Nowadays, it is known that tsunamis have different generation mechanisms.

Tsunamis are the destructive long waves which can either occur from under the ocean (e.g. earthquakes, sub-marine landslides and/or volcanic eruptions) or from above the ocean (e.g. meteorological events, asteroid impacts). Furthermore, the generation and propagation of the long waves and their effects on the coastal and harbor regions are the important subjects in the coastal and ocean engineering and science. The series of waves which are formed in the deep ocean due to the various impacts propagate towards the shore. The important characteristics of the tsunamis are their large wave heights and high speeds. During propagation to the shore, wave heights are getting higher due the decrease in the depth of the ocean. Also, travelling speed of the waves can be as fast as planes through the deep ocean and speed slow down while waves approach to the shore.

Generally, tsunamis have 40 km to 200 km wave length and wave period in between 3.5 min to 20 min or longer (Wu, 1981). But, these characteristics certainly depend on the generation mechanisms of the tsunamis. The generation and propagation of

tsunamis can be affected by sea bottom and the wave characteristics; so that the devastating consequences of the tsunamis at coastlines vary.

Tsunamis generated by earthquakes and landslides have been studied by many researchers, but there are limited studies related to the meteorological origin tsunamis. In this thesis, particularly the meteorological tsunamis, or meteotsunamis are investigated. Meteotsunamis are the displacement of water body due to the atmospheric pressure disturbances which can be observed in the oceans all over the world and are entitled with local names such as “rissaga” (Baleric Island), “marubbio” (Sicily), “milghuba” (Malta), “abiki” (Nagasaki Bay) and “Seebär” (Baltic Sea) (Monserrat and Rabinovich, 2006).

Characteristics of this type of meteorological origin events are similar to ordinary tsunamis. Rabinovich and Monserrat (1996) stated that meteorological origin long waves have same wave period with typical tsunamis (a few minutes to 2-3 hours) and they can cause loss of human life and devastating destructions at coastal zones like ordinary tsunamis. In other words, the only difference of the meteorological tsunamis is that unless underwater impact, they are generated due to the meteorological forces from above the ocean. Also, meteotsunamis can have different source mechanisms such as spatial and temporal pressure distributions, atmospheric gravity waves and squall lines. The aim of this thesis is to investigate the possible effects of meteotsunamis due to the spatial and temporal pressure distributions by considering the influential parameters (e.g. bathymetry, pressure velocity) and to develop a numerical model.

The content of the thesis is constituted as in the following. In Chapter 2, details of approaches associated with the meteotsunamis are given by reviewing literature. In Chapter 3, applied method is described giving problem statement and numerical model NAMI-DANCE-P is described. Also, model is verified by using regular shape flat bathymetry. Chapter 4 includes the numerical tests simulations, results and discussions. Finally, in Chapter 5, general summaries, conclusions and future recommendations are presented.

CHAPTER 2

LITERATURE SURVEY

2.1. Recent Observations

Meteotsunamis are observed at certain regions all over the world. These meteorological origin waves are documented in scientific literature by many of researchers and given as follows: East Coast (Churchill et al., 1995; Sallenger et al., 1995; Pasquet and Vilibić, 2013; Lipa et al., 2013), Gulf of Mexico (Paxton and Sobien, 1998), The Great Lakes (Ewing et al., 1954; Donn, 1959; Bechle and Wu, 2014), Atlantic Ocean (Mercer, 2002; Candella, 2009; Dragani et al., 2009), Adriatic Sea (Vučetić et al., 2009; Šepić et al., 2012), Mediterranean (Airy, 1878; Monserrat et al., 1991; Rabinovich and Monserrat, 1996; Vilibić et al., 2008), the Aegean Sea (Papadopoulos, 1993), Black Sea (Vilibić, 2010), East China Sea (Hibiya and Kajiura, 1982; Tanaka, 2010), Sea of Japan (Park et al., 1986) and Yellow Sea (Wang et al., 1987; Cho et al., 2013). Moreover, Pattiaratchi and Wijeratne (2015) listed meteotsunamis according to their maximum wave height then related figure (2.1) and table (2.1) are given in the following.

The one of the devastating wave is observed in Nagasaki Bay on March 31, 1979. Hibiya and Kajiura (1982) investigated these destructive events which called as an “abiki” phenomenon in their research study. They stated that during the event atmospheric pressure disturbance are measured at a few surrounding stations and it means that pressure disturbance was moving eastward with a certain average velocity. Thereafter, they examined the real case by numerical simulation and proved the large water level oscillations in Nagasaki Bay that reached 2.78 m due to the

propagation of the pressure disturbance. The average depth of the Nagasaki Bay is 20 m (shallow) and it is a narrow bay and therefore the wave which is spawned due to the pressure disturbance was amplified. Accordingly, the authors expressed that eigenoscillations on the shelf were observed and water wave resonantly amplified, in addition to resonance effect, shoaling and reflection in the bay could also be triggered the amplification. However, they thought that to explain the generation and behavior in the East China Sea, atmospheric pressure disturbances are not sufficient for a quantitative study.

Figure 2.1. Meteotsunami events in literature (Pattiaratchi and Wijeratne, 2015)

There is another destructive meteotsunami event occurred on June 15, 2006 in the Balearic Islands. Vilibić et al. (2008) analyzed that tsunami-like event observed on Ciutadella Harbor called as “rissaga” through numerical modeling. They agreed to cause of this rissaga event is the travelling atmospheric pressure disturbance.

Table 2.1. List of meteotsunamis in the literature with maximum wave heights (retrieved from Pattiaratchi and Wijeratne, 2015)

No.	Location	Max. Wave Height (m)
1	British Columbia andWashington State	0.17
2	San Diego, CA	0.05
3	Chicago, Great Lakes (USA)	3.0
4	Newfoundland, Canada	1.0
5	Boothbay, ME	4.0
6	NE Atlantic coast of USA	0.5
7	Daytona Beach, FL	3.0
8	Eastern Gulf of Mexico	>3.0
9	Arraial do Cabo, Brazil	0.60
10	Buenos Aires coast, Argentina	0.62
11	Portugal/France	0.20
12	west coast, UK	0.40
13	Ireland	>1.0
14	Scotland, UK	0.20
15	Southern North Sea	0.80
16	Baltic Sea	2.0
17	Finland, Baltic Sea	2.0
18	Balearic Islands	5.0
19	Sicily, Italy	~1.5
20	Malta	~1.0
21	Crotia	6.0
22	Greece	0.80
23	Black Sea	3.2
24	Odessa, Black Sea	2.0
25	Dwarskersbos, South Africa	2.9
26	West coast of India	0.40
27	Sri Lanka	0.20
28	Longkou Harbour, China	2.9
29	South Korea	1.6
30	Nagasaki Bay, Japan	4.8
31	Kural Islands	0.37
32	Taiwan	0.5
33	West Australia	1.1
34	Burnie, Tasmania	0.6
35	New Zealand	1.0

According to eyewitnesses, a sudden wave struck to the coast with more than 4 meters and caused huge economic losses. The speed of the currents reached to 4 m/s at harbor and maximum wave height is found as 2.5 m from the numerical model. The authors clarified that the difference between the wave heights gathered from numerical model and eyewitnesses report can be observed due to the lack of the bathymetry data. On the other hand, they also stated that even during the most powerful event, atmospheric pressure disturbance can cause maximum 2-6 cm change in the water surface elevation. Accordingly, atmospheric oscillations can generate notable sea-levels only in the case of occurrence of the resonance between the atmosphere and the ocean.

Vilibić and Šepić (2009) overviewed destructive meteorological origin events observed in the Adriatic Sea in their study. First one is the Vela Luka flood observed in 1978 which has around 3 m water surface elevation. In literature, scientists argued on the causes of the generation of this event and different hypotheses are asserted such as earthquake-generated, submarine landslide generated and cyclone based tsunami event. In the study, the latter thesis is found more close to the reality which is explained by meteorological tsunami like event and effect of resonance. Secondly, meteotsunami was seen in the Ist Island in 1984 and 2007. In the both two different time events, 4 m waves hit the island. As another damaging event in the Adriatic Sea, Stari Grad Bay meteotsunami where almost 3.5 m wave height is observed in 2003 is reported. Also, the Mali Lošinj flood in 2008 caused disruptive results by 2 m wave heights. Accordingly, this flood is related to atmospheric disturbances and resonance process.

On 7 May 2007, tsunami-like event was observed in the Bulgarian Black Sea. The only thing known about this event is its non-seismic and unknown origin. The maximum water surface elevation which was observed during the event was 3 meters and in many places near the Bulgarian coasts wave anomalies were detected. Accordingly, two hypotheses are formed concerning to generation mechanism. One of them is that tsunami-like event generated by a submarine landslide and the other

one is the formation of the abnormal waves due to the atmospheric pressure disturbances.

Ranguelov et al. (2008) studied the first hypothesis which was generation of the sea disturbance by a landslide. Although, the authors are sure of that there is no seismic movement during the event in conformity with seismic network centre in Bulgaria (NOTSSI – National Observation Telemetric Seismic System of Information), they doubt that the atmospheric pressure disturbances cannot be the reason of this event. According to the barographic records, in the morning of 7 May abrupt change in the atmospheric pressure was recorded. Nevertheless, in the paper landslide effect was researched as a possible cause of the event. To explain this preference, authors stated that such events tend to occur in short time intervals, at most in the order of the years, but in the Bulgarian coasts, there were not such anomalies in the water for a long time. At the end of the study, they found that in the case of submarine landslide, the frequency and the amplitude of the calculated waves were in agreement with the observations.

On the other hand, Vilibić et al. (2010) studied the same event (7 May 2007) considering the generation mechanism as an atmospheric pressure differences. They emphasized that due to the records of sudden air pressure variations, propagation of the atmospheric pressure was clearly visible. Also, during the event at the Bulgarian shoreline, no abnormal waves at certain locations (e.g. around Emine) has been observed, but maximum waves have been observed in the modeling of the landslide generated tsunami-like event study. Therefore, atmospheric pressure variations and propagation are given as possible causes of that event. Besides, in the latter study, due to the lack of the resolution and quality of the data and bathymetry, rough estimation was made and it was necessary to explain that the event can be classified as a meteotsunami. Also, this study can be a sample for evaluating the unclassified less destructive tsunami-like events related to their source mechanism.

One of the interesting tsunami-like chained events was observed on June 23-27, 2014 in the Mediterranean and Black Seas with an influenced area from Spain to Ukraine. Šepić et al. (2015) demonstrated that the cause of these long period waves was the atmospheric pressure disturbances. This event differs from the other tsunami-like events because it is the first reported example where the series of waves were propagating in a certain direction affecting the different areas on specific dates. The first destructive wave was observed in Ciutadella Inlet (Spain) with a height of 1 m on June 23. After 2 days, destructive tsunami-like waves were observed in the Adriatic Sea. On June 25, the strongest wave heights recorded as 3 m in Vela Luka Bay. On the same day, 1.5 m tidal bore struck to the Mazara del Vallo inlet in the evening hours. Then, on June 26, maximum 1 m wave height was seen in the Adriatic Sea. Lastly, on 27 June 2014, wave height of 1-2 m suddenly hit Odessa coast on a calm and sunny day. Also, shores nearby the Odessa, in particular Ukraine were affected from this event. In general, in the Mediterranean and Black Seas earthquake generated tsunamis are recorded. However, in this tsunami-like case no seismic record exists; therefore a possible cause of that event was investigated which is air pressure disturbances. One of the interesting points in that situation is that although meteotsunamis frequently occur in the Mediterranean and Adriatic Seas, in the Black Sea few events are reported in the history with an “unknown origin”. Second is that the event can be a proof to propagation of atmospheric pressure disturbances over a thousand kilometers expanse with a certain velocity.

On the other hand, some recession events at west and south coasts of Turkey draw an attention. The main factor behind these events might be meteorological disturbances (Metin et al., 2016). For last eleven years, the related events are reported in the Figure 2.2 and Table 2.2. In the figure, dates and locations of events are shown. In the table, events are listed on a chronological order. Also, there are some successive events observations. For example, in 2008, the around 40 m wave recession event is observed at Gümüşlük and Şarköy at the same time. Similarly, in 2011, in Marmaris (15 m), Çanakkale (50-60 m) and Gümüşlük (10 m) recessions are recorded. The relation between these events and atmospheric pressure disturbances should be investigated.

Table 2.2. List of recession events at the coasts of Turkey

Çanakkale	13.Jan.05
Marmaris&Gökova	14.Jan.05
Marmara/Yalova	24. Jan.06
Marmara/Tekirdağ	29. Jan.06
Marmara/Tekirdağ-Şarköy	30.Dec.06
Bodrum/Gümüşlük	4. Jan.07
Marmara/Tekirdağ	8. Jan.07
Bodrum/Gümüşlük	22.Feb.08
Marmara/Yenice-Şarköy	22.Feb.08
Çanakkale	25.Oct.08
Balıkesir/Erdek	10. Jan.09
Marmaris/Uzunyalı	12. Jan.09
Marmara/Tekirdağ-Çorlu	30. Jan.09
Balıkesir/Erdek	9.Feb.11
Marmaris/Uzunyalı	13.Mar.11
Çanakkale	15.Mar.11
Bodrum/Gümüşlük	15.Mar.11
Marmara/Yeniköy	25.May.11
Balıkesir/Erdek	24.Nov.11
Marmaris/Uzunyalı	13.Dec.11
Fethiye	10.Jun.12
Antalya/Damlataş	21.Oct.13
Marmaris/Uzunyalı	11.Dec.13
Çanakkale	15.Mar.14
Balıkesir/Erdek	16.Mar.14
Çanakkale	20.Feb.15
Akyarlar-Muğla	19.Apr.15
Akyaka-Muğla	25.Dec.15
Akyaka-Muğla	26.Dec.15
Marmaris/Uzunyalı	4.Jan.16

Figure 2.2. Map of recession events at the coasts of Turkey (2005-2016)

2.2. Numerical Modeling

Hibiya and Kajiura (1982) applied numerical model which computes water surface elevation (η) and depth-integrated transport components in the x and y directions (Q_x and Q_y) by using leap-frog finite difference method. The model has been developed based on linearized shallow water equation for ideal fluid. Coriolis force, all frictional forces and wind stress term are neglected. The shallow water motion (Eq. 2.1 and Eq.2.2) and continuity equations (Eq.2.3) used in model are in the following.

$$\frac{\partial Q_x}{\partial t} = -gh\frac{\partial}{\partial x}(\eta - \eta^*) \tag{2.1}$$

$$\frac{\partial Q_y}{\partial t} = -gh\frac{\partial}{\partial y}(\eta - \eta^*) \tag{2.2}$$

Then substituting $\eta^* = -p/(\rho g)$ where p atmospheric pressure disturbance is ρ average sea water density and g is the gravitational acceleration in the equation 2.1 and 2.2, and solving the equations together following equation is obtained.

$$\frac{\partial \eta}{\partial t} = -\left(\frac{\partial Q_x}{\partial x} + \frac{\partial Q_y}{\partial y}\right) \tag{2.3}$$

The model was applied for two domains where one of them is the nested domain and grid intervals specified as 4 km for bigger region and 2 km for nested region. Also, time interval (Δt) is determined to be 3 sec. On the other hand, pressure wave linearly increase to the crest by Δp = 3 mb by a width of 169 km, then linear decrease is observed. The total width of the pressure wave is 241 km. It is propagating with a constant 31.33 m/sec velocity in the direction 5.6 degrees north of east. At the end of the simulations, general characteristics of the calculated results and the observations are in agreement.

SCHISM (Semi-implicit Cross-scale Hydroscience Integrated System Model) is another hydrodynamic model that can be used to solve atmospherically induced meteotsunamis. The model is the derivation of the SELFE model and it has been developed by Dr. Joseph Zhang. The model is based on unstructured (mix of triangular and quadrangular) grid model with semi-implicit time stepping and finite element structure (Zhang et al., 2016). Šepić et al. (2016) performed numerical simulations by using SCHISM in 2-D mode and the equations are shown below.

$$\frac{\partial \eta}{\partial t} + \nabla\left(H\vec{U}\right) = 0 \tag{2.4}$$

$$\frac{\Delta \vec{U}}{\Delta t} = -\nabla\left(\frac{p_a}{\rho_0} + g\eta\right) - f\vec{k} \times \vec{U} + \frac{\vec{\tau}_w - \chi\vec{U}}{\rho_0 H} + \vec{F}_{hd} + \hat{\alpha} g \nabla\psi + \vec{R}_s \tag{2.5}$$

The continuity (2.4) and momentum (2.5) equations are written in the Cartesian form, where η is water surface elevation, H is the total water depth, $\vec{U}$ is the velocity, p_a is the atmospheric pressure, ρ_0 is density of water, f is Coriolis constant, $\vec{k}$ is the

vertically upward unit vector, $\vec{\tau}_w$ is the wind stress, $\chi\vec{U}$ is the bottom friction, and $\vec{F}_{hd}$ represents horizontal momentum diffusion. Also, tidal potential, radiation stress and wind stress are neglected. Therefore, sea level differences are calculated considering only the atmospheric pressure disturbance. This model was applied to the real case, multi-meteotsunami event observed on 23-27 June, 2014. The bathymetric field is discretized by triangular elements with resolution 2.5 km in open sea and 450 m near the shorelines. Time step of the simulations was determined as 60 seconds. Air pressure disturbance data were specified in different ways. Also, the pressure data were inputted to the numerical model assuming that the propagation of the pressure is in constant velocity and direction. 1025 different simulations were conducted by combination of different velocities and directions and single simulation duration was 18 hours. At the end of the simulations, maximum wave heights are calculated at the places where meteotsunamis occurred. The modelling of waves is reasonable but model underestimated the wave heights for some locations, because combination of the atmospheric pressure forcing and resolution of the bathymetry cannot be well-suited.

Šepić et al. (2009) studied the possible source of the Ist Meteotsunami in 2007. With data analysis, it is obvious that the destructive waves were triggered by a double resonance mechanism with beginning of the atmospheric pressure disturbances. Speed and direction of pressure disturbance were obtained via two methods: the isochronal analysis method and the cross-correlation function analysis method. After data analysis, to determine the cause of the pressure oscillations between two possibilities, the event was simulated through the WRF (Weather Research and Forecasting) numerical model. The numerical model is the 3-D, Euler non-hydrostatic and fully compressive fundamental equation model and it simulates atmospheric processes (Skamarock et al., 2005). Pressure velocity is determined 21-24 m/sec by data analysis and atmospheric numerical modeling. Thereafter, wind speed calculated as 22 m/sec. Finally, as a result of the simulations, it is accepted that the atmospheric pressure disturbance is a ducted gravity wave.

As another model, the 2-D nonlinear shallow water model was used to simulate the abnormal waves observed on 15 June 2006 in the Balearic Islands (Vilibić et al., 2008). The model is developed by momentum equations including air pressure term and continuity equation. Basically, the related equations for the model are in the following.

$$\frac{\partial u}{\partial t} + u\frac{\partial u}{\partial x} + v\frac{\partial u}{\partial y} - fv = -g\frac{\partial \zeta}{\partial x} - \frac{gu\left(u^2+v^2\right)^{\frac{1}{2}}}{C^2(h+\zeta)} - \frac{1}{\rho}\frac{\partial P}{\partial x}; \tag{2.6}$$

$$\frac{\partial v}{\partial t} + u\frac{\partial v}{\partial x} + v\frac{\partial v}{\partial y} - fu = -g\frac{\partial \zeta}{\partial y} - \frac{gv\left(u^2+v^2\right)^{\frac{1}{2}}}{C^2(h+\zeta)} - \frac{1}{\rho}\frac{\partial P}{\partial y}; \tag{2.7}$$

$$\frac{\partial \zeta}{\partial t} + \frac{\partial}{\partial x}[(h+\zeta)u] + \frac{\partial}{\partial y}[(h+\zeta)v] = 0, \tag{2.8}$$

where $\zeta$is the water level elevation, h is the still water depth, $f$is the Coriolis parameter, t is time, u and v are the average mean velocities in the x and y directions, ρ is the water density, P is the atmospheric pressure and C is the Chezy's friction coefficient and expressed by equation 2.9.

$$C = 18\log\left(\frac{0.37h}{z_0}\right), \tag{2.9}$$

where z_0 is the bottom roughness length. The first three equations are solved by using an explicit leapfrog method. For the case study, bathymetry data were taken from GEBCO as coarse grid cells (1.45 km x 1.85 km). At all open boundaries, radiation boundary conditions are applied. Radiation boundary conditions provide to avoid wave reflection towards to the computational domain or wave motions cross the boundaries with small reflections (Broeze and Van Daalen, 1992). Time step, Δt was used as 4 sec for the simulations. Besides, for the regions where the destructive waves have been observed, nested gridding with 10 m was preferred in this study. Atmospheric pressure records were given to the program as an input with a constant speed in a specified direction. Also, data were interpolated linearly at each grid point.

Finally, the model was verified by solving past meteotsunami event, then compared with the event observed on June 2006 by using same parameters.

On the other hand, meteorologically induced tsunami in Ciutadella Harbor in June 2006 was modeled through nested atmospheric and ocean models. Renault et al. (2011) used WRF as an atmospheric model for 2 nested domain (20 km resolution for greater domain, 4 km resolution for inner domain) to determine atmospheric features of the meteotsunami. After 72 hour simulations, model generates atmospheric pressure oscillations propagating by 27 m/sec, afterward, oceanic simulations were conducted by ROMS (Regional Ocean Modeling System) which is 3-D free sea surface, split-explicit fundamental equation model with Boussinessq and hydrostatic approximation finite difference model (http://www.myroms.org/). In the modeling, 1 km resolution was preferred (256×200 grid points) and at the nested domain the resolution was 10 m (401×302 grid points). The higher resolution enabled good sampling of the Ciutadella Harbor. In every 2 minutes, sea level pressure was given to the model. In addition to the sea level pressure, wind forcing was also inputted to the model to observe the effect of the wind in the ocean. The results of the implementation of both atmospheric and oceanic models were in agreement with the general characteristics of the observations. Besides, wind did not have major role in the rissaga event because the results with wind forcing were found similar to those without wind.

Tanaka (2010) investigated air pressure wave bands in the East China Sea meteotsunami observed in February 2009. According to the weather records, low atmospheric pressure was moving over the East China Sea during the event and there were observed local pressure disturbances. As a numerical simulation model of present meteorological tsunami event, WRF model was used. It supports two solvers: the Advanced Research WRF (ARW) and Non-hydrostatic Mesoscale Model (NMM). In this study WRF-ARW was used in the simulation using meteorological dataset. The problem was investigated within three domains where coarser, inner, finer domain grid spacing was 50 km, 10 km and 2.5 km respectively. The forecast simulation duration was 48 hours. In conclusion, large pressure bands were found on

the middle of the East China Sea which propagated and struck to the coasts. Additionally, ocean wave phase velocity was expected as 25-35 m/sec and it was almost as high as pressure band velocity.

Marcos et al. (2003) studied the effect of pressure velocity and platform characteristics on the coastal amplification of meteotsunamis. In their study, 2-D finite difference numerical model which was developed by the University of Cantabria was used as a numerical model. In this model, the momentum equation includes the air pressure term. Besides, the numeric model solves continuity, momentum and diffusion equations by using finite difference method. The related mass conservation equation (2.10), momentum conversation equations (2.11 and 2.12) and diffusion equation (2.13) are in Cartesian form and given in the following.

$$\frac{\partial(HU)}{\partial x}+\frac{\partial(HV)}{\partial y}+\frac{\partial \eta}{\partial t}=0, \tag{2.10}$$

$$\frac{\partial(UH)}{\partial t}+\frac{\partial(U^2H)}{\partial x}+\frac{\partial(UVH)}{\partial y}=fVH-\frac{1}{\rho_0}\frac{\partial P_a}{\partial x}-gH\frac{\partial \eta}{\partial x}-\frac{g}{2\rho_0}H^2\frac{\partial \rho_0}{\partial x}-\frac{g}{\rho_0}\int_{-h}^{\eta}\left[\frac{\partial}{\partial x}\int_z^{\eta}\rho' dz\right]dz+$$
$$\tau_{xz(\eta)}-\tau_{xz(-h)}+H\varepsilon_h\left[\frac{\partial^2 U}{\partial x^2}+\frac{\partial^2 U}{\partial y^2}\right]+2H\frac{\partial \varepsilon_h}{\partial x}\frac{\partial U}{\partial x}+H\frac{\partial \varepsilon_h}{\partial y}\left[\frac{\partial U}{\partial y}+\frac{\partial V}{\partial x}\right], \tag{2.11}$$

$$\frac{\partial(VH)}{\partial t}+\frac{\partial(V^2H)}{\partial y}+\frac{\partial(UVH)}{\partial x}=-fUH-\frac{1}{\rho_0}\frac{\partial P_a}{\partial y}-gH\frac{\partial \eta}{\partial y}-\frac{g}{2\rho_0}H^2\frac{\partial \rho_0}{\partial y}-\frac{g}{\rho_0}\int_{-h}^{\eta}\left[\frac{\partial}{\partial y}\int_z^{\eta}\rho' dz\right]dz+$$
$$\tau_{yz(\eta)}-\tau_{yz(-h)}+H\varepsilon_h\left[\frac{\partial^2 V}{\partial x^2}+\frac{\partial^2 V}{\partial y^2}\right]+2H\frac{\partial \varepsilon_h}{\partial y}\frac{\partial V}{\partial y}+H\frac{\partial \varepsilon_h}{\partial x}\left[\frac{\partial U}{\partial y}+\frac{\partial V}{\partial x}\right], \tag{2.12}$$

$$\frac{\partial C}{\partial t}+U\frac{\partial C}{\partial x}+V\frac{\partial C}{\partial y}=\frac{1}{H}\frac{\partial}{\partial x}\left(HD_x\frac{\partial C}{\partial x}\right)+\frac{1}{H}\frac{\partial}{\partial y}\left(HD_y\frac{\partial C}{\partial y}\right), \tag{2.13}$$

where U and V are the depth-averaged velocity, H is the total depth, η is the free surface, h is water depth, ε_h and ε_z are the horizontal and vertical eddy viscosity coefficients, respectively, P_a is air pressure, f is the Coriolis parameter, D_x and D_y are the horizontal diffusivity constants and C is the constant which is calculated by using equations given in Mellor (1991). The equations were solved through an implicit finite difference technique, except non-linear terms. The simulations were

conducted for both actual (meteotsunami in Ciutadella Inlet in 1997) and idealized bathymetries. The grid size was 500 m and time step was 5 seconds. In the upper and lower boundaries of the bathymetries radiation conditions, in the left and right boundaries reflection boundary conditions were used.

As a result of these simulations, it was observed that atmospheric pressure disturbances were created standing waves where their periods were controlled by bathymetric conditions and their energy were depended on pressure wave speed. The optimum energy transfer was seen when phase speed was 25 m/sec which equals to wave velocity. Also, for this event, numerical model results were in agreement with observations.

2.3. Resonance by Coupling of Ocean Wave Motion and Atmospheric Pressure Forcing

The standing water level variations in bounded or partially bounded basin are called as seiches. The agitation of the basin depends on basin geometry and water depth and these fluctuations occur at eigen periods (natural resonant periods) of the basin. Sea level fluctuations at shore are generally categorized according to their frequency or generation mechanisms. In fact, these two parameters are related with each other because generation mechanisms determine the frequency range of the wave. As the same generation mechanisms create fluctuations in different frequencies, also different generation mechanisms can cause oscillations with same frequencies. Furthermore, atmospheric pressure forcing can affect the water level in a wide frequency range. The natural periods of seiches could be from a few minutes to few hours. The most important factors triggered seiches are nonlinear relations of wind waves and atmospheric disturbances (Rabinovich, 2009).

The special energy sources such as atmospheric gravity waves, pressure jumps, frontal passages, squalls and storms which generate the seiches affect the amplitudes of the seiches. Whatever the generation mechanism is, only few hPa pressure changes are observed in the atmosphere which leads to just few cm variations in the

sea level. Metin et al. (2015) specified that when air pressure decreases gradually, the water level in sea region rises and vice versa (so-called inverse barotropic effect). It means that when depression in air pressure is order of 1 hPa, sea level rise is order of 1 cm. Therefore, significant water levels can be observed only when the resonance occurs between ocean wave motion and atmospheric pressure forcing. Kian et al. (2015) stated that when the governing frequencies of the seiches coincide with one of the periods of free oscillations in the basin, resonance and amplification occur and can cause a problem of the management of coastal structures and their utilization.

The most important three external resonance mechanisms are (i) Proudman resonance, (ii) Greenspan resonance and (iii) shelf resonance (Monserrat et al., 2006). In general, the possible cause of the development of strong waves generated due to air pressure disturbances is energy transfer from the atmosphere to the sea by resonant effects. In the following, three different types of resonance effects are reviewed shortly.

(i) Proudman resonance

Pattiaratchi and Wijeratne (2015) specified that Proudman resonance is estimated as a main cause of meteotsunamis happening all over the world. Proudman resonance occurs when the atmospheric pressure movement velocity, V, coincide with ocean wave celerity, c, which means V=c. Analytical theory of the Proudman resonance is defining the movement of the atmospheric pressure disturbance over the uniform fluid by using linearized depth-averaged equations by ignoring friction, Coriolis and advection terms. The changes in the water surface level due to air pressure disturbances depend on the Froude number (Fr) which can be defined as Fr=V/c. The equation (2.14) is Proudman expression in the non-dimensional case.

$$\frac{\eta}{\eta_s} = \frac{1}{1-Fr^2} \tag{2.14}$$

where η is the change in the sea surface level, η_s is the stationary case. When the V is equal to the c, maximum deformation in water level is unrestrained due to lack of

damping and then resonance is observed. Šepić et al. (2015) stated that when the Fr≈1.0, during movement of the ocean waves, atmospheric energy is absorbed and therefore strong amplification is seen.

(ii) Greenspan resonance

Greenspan resonance is similar to Proudman resonance where the air pressure velocity in alongshore direction (V_l) is close by to propagation phase speed of *j*th mode of edge waves (c_j). The analytical theory suggested by Munk et. al. (1956) for solid state which means that air pressure disturbance is steady and it was extended to unsteady state by Greenspan (1956) using linear shallow water equations by considering numerous modes on the continental shelf. The amplification of the wave due to Greenspan resonance depends on wave height is formed due to air pressure disturbance, beach slope and speed of propagation.

(iii) Shelf resonance

When period or wavelength of the atmospherically induced ocean wave and continental shelf region resonant are equal, shelf resonance is observed. Atmospheric pressure disturbance cause the initial change in water surface level, and restoring force (gravity) try to keep a level surface. Then observed oscillations depend on only the geometry such as length, water depth, topographic funneling and bed slope.

On the other hand, as an internal resonance mechanism, harbor resonance has important role on wave amplification near the shore. When natural resonance of a semi enclosed sea area coincides with resonance frequency of incoming wave then strong amplification can be observed. The amplified wave depends on the geometry of the sea area. Bailey et al. (2014) stated that in long, narrow and shallow bays, stronger oscillations occur while the system tends to low rate of energy dissipation.

Some remarkable locations have high meteotsunami possibilities which are generally related to continental shelf topography and shoreline geometry. Mainly, internal (harbor resonance) and external factors (Proudman, Greenspan and Shelf resonances) are two important influences for wave amplification. In the case of intensive air pressure disturbances, the disturbance parameters and resonant parameters coincide with each other and destructive events may be observed. As an example, the abiki event on 31 March 1979 in Nagasaki Bay may be used to explain generation mechanisms of meteotsunamis. In the Figure 2.3, physical mechanism of development of destructive meteorological origin waves at Nagasaki Bay is illustrated.

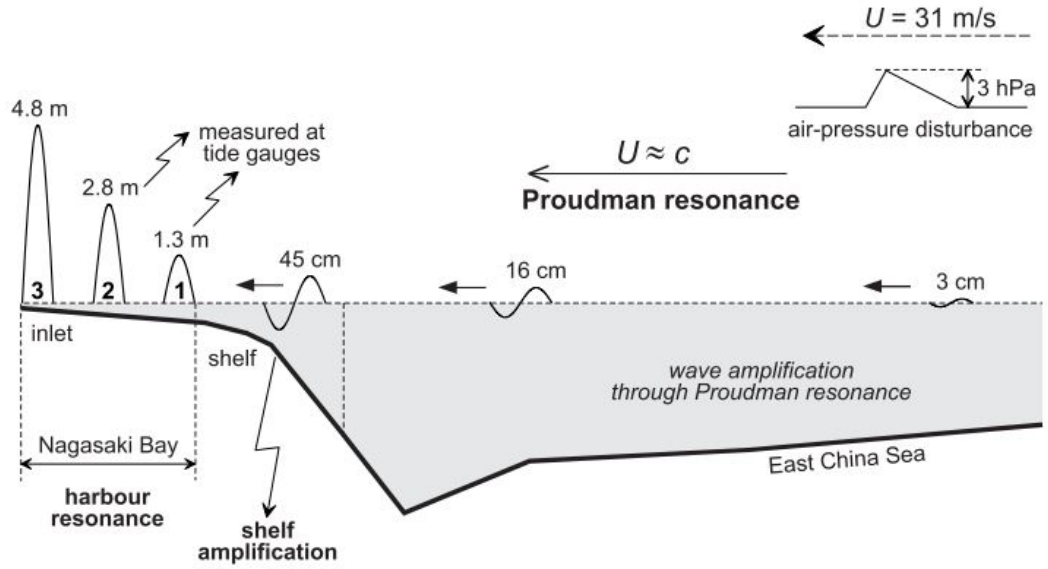

Figure 2.3. Physical mechanism of development of destructive meteorological origin waves at Nagasaki Bay on 31 March 1979 (Monserrat et al., 2006)

CHAPTER 3

PROBLEM AND METHOD

3.1. Wave Generation and Propagation due to Atmospheric Pressure Disturbances

An ocean wave transfers energy from one side to another side. This energy movement generally categorized according to their energy source. Mostly, it is created by wind, tide and tsunami. Additionally, air pressure differences can generate wave. The air pressure force is the pressing down air on the earth surface. The atmospheric air pressure depends on altitude, temperature, air density and time. For instance, when the temperature is lower, the atmospheric air pressure decreases, conversely higher temperature leads to high air pressure. In this problem, the important mechanism is that the flow of the air which is observed from high pressure to low pressure. High atmospheric pressure causes a static water level drop and contrariwise, low atmospheric pressure causes a static water level rise. In general, 1 mbar depression in air pressure causes almost 1 cm rise in mean sea level. Due to the air flow from high pressure to low pressure, water level differences are observed for the certain area between these high and low pressure points. The differences create waves and sometimes amplify towards to the shore.

On the other hand, the bathymetry is an important factor that causes the amplification of the long waves generated by atmospheric pressure disturbances. Different types of bathymetries can lead to different consequences. Similarly, the speed of pressure (V) and speed of wave (c) are two important parameters which govern the characteristics of the generated long waves. In nature, the pressure velocity is slow but sometimes it exceeds 30m/sec. But the wave speed is controlled by the water depth and it may be faster or slower or equal to the pressure speed. Therefore, the shape and propagation

of the generated wave differ. In this study, by combining all of these factors as a case study, wave generation and propagation due to atmospheric pressure movements are separately analyzed in different simulations using different pressure speed and different bathymetry conditions.

The aim of this chapter is to define the analytical solution of the linear shallow water model and numerical solution of nonlinear shallow water model. Thereafter, analytic and numerical models were applied to the certain test cases and it helps to interpret verification of the numerical model and the wave generation and propagation mechanism due to the pressure differences.

3.2. Analytic Solution

A hydrodynamic model is used to identify water motion and it contains set of equations. The long waves generated by atmospheric pressure disturbances can be modelled based on Euler equations for ideal fluid on the non-rotated Earth. In the following equations, well-known Euler equations are revealed for the corresponding boundary conditions at the bottom and ocean surface.

$$\frac{\partial u}{\partial t} + (u\nabla)u + w\frac{\partial u}{\partial z} + \frac{1}{\rho}\nabla p = 0 \tag{3.1}$$

$$\frac{\partial w}{\partial t} + (u\nabla)w + w\frac{\partial w}{\partial z} + \frac{1}{\rho}\frac{\partial p}{\partial z} = -g \tag{3.2}$$

$$\nabla u + \frac{\partial w}{\partial z} = 0 \tag{3.3}$$

Here, u and w are horizontal and vertical components of the velocity, respectively, ρ is density of water, p is pressure, g is the gravitational acceleration, h(x,y) is the varying ocean depth. Also, x and y coordinates are in the horizontal plane and z-axis is aligned upwards vertically. At the solid bottom (z=-h(x,y)),

$$\mathrm{w} - (u\nabla)h = 0 \tag{3.4}$$

At the free surface (z=η(x,y,t)),(where η(x,y,t) is the water surface elevation) the kinematic condition is,

$$w = \frac{d\eta}{dt} = \frac{\partial \eta}{\partial t} + (u\nabla)\eta \tag{3.5}$$

and the dynamic condition is,

$$\mathrm{p} = p_{atm}(\mathrm{x}, \mathrm{y}, \mathrm{t}). \tag{3.6}$$

In the shallow water theory, the primary assumption is that the vertical velocity and acceleration are small in comparison with horizontal ones. Therefore, in equation (3.2), the vertical acceleration term ($\frac{\partial w}{\partial t}$) can be neglected and by integrating Eq. (3.2) and Eq. (3.6), hydrostatic pressure is obtained.

$$\mathrm{p} = p_{atm} + \rho \mathrm{g}(\eta - \mathrm{z}). \tag{3.7}$$

Afterward, solving Eq. (3.1) and Eq. (3.7) together, and ignoring vertical acceleration term once more, the first equation of shallow water equation is found.

$$\frac{\partial \eta}{\partial t} + (u\nabla)u + \rho\nabla\eta = -\frac{\nabla p_{atm}}{\rho} \tag{3.8}$$

The integration of Eq. (3.3) over solid bottom to free surface gives the second equation of shallow water equation,

$$\frac{\partial \eta}{\partial t} + \nabla[(\mathrm{h} + \eta)\mathrm{u}] = 0. \tag{3.9}$$

The equations (3.8 and 3.9) are non-linear and inhomogeneous. The linear versions of these equations are obtained as the following.

$$\frac{\partial u}{\partial t} + g\nabla\eta = -\frac{\nabla p_{atm}}{\rho} \tag{3.10}$$

$$\frac{\partial \eta}{\partial t} + \nabla[\mathrm{hu}] = 0 \tag{3.11}$$

From these linear set of shallow water equations by omitting the u term, the wave equation for the surface elevation can be obtained and shown in Eq. (3.12).

$$\frac{\partial^2 \eta}{\partial t^2} - \nabla(c^2 \nabla \eta) = \nabla\left(\frac{h \nabla p_{atm}}{\rho}\right), \tag{3.12}$$

where long wave propagation speed is

$$c(x, y) = \sqrt{gh(x, y)}. \tag{3.13}$$

The Eq. (3.12) represents the governing linear hydrodynamic model of long waves generated due to atmospheric pressure disturbances. For the constant depth, the equation reduces to the typical wave equation

$$\frac{\partial^2 \eta}{\partial t^2} - c^2 \nabla^2 \eta = \frac{h \nabla^2 p_{atm}}{\rho}. \tag{3.14}$$

Thereafter, by using following variables,

$$\eta = \zeta - \zeta_a, \qquad \zeta_a = \frac{h p_{atm}}{\rho c^2} \tag{3.15}$$

Eq. (3.14) is written in a different form,

$$\frac{\partial^2 \zeta}{\partial t^2} - c^2 \nabla^2 \zeta = \frac{\partial^2 \zeta_a}{\partial t^2}. \tag{3.16}$$

For the case of atmospheric disturbances, the solution of Eq. (3.16) is trivial and the water level defined as,

$$\eta = -\zeta_a = -\frac{h p_{atm}}{\rho c^2}. \tag{3.17}$$

This relation (Eq. (3.17)) is known as “the inverse barometer effect”. It means that low atmospheric pressure can cause the sea level rise and high atmospheric pressure leads to depression in the mean sea level. If pressure is moving, a resonance can be observed between pressure velocity and wave speed. Let consider the one-dimensional pressure model where pressure is varied throughout only the x-axis with a constant velocity, V. Then, the solution of Eq. 3.14 is

$$\eta(x,t) = \frac{c^2}{V^2-c^2}\zeta_a(x-Vt) - \frac{c}{2(V+c)}\zeta_a(x-ct) + \frac{c}{2(V+c)}\zeta_a(x+ct). \tag{3.18}$$

It satisfies the zeroth initial conditions,

$$\eta = 0\,, \quad \frac{\partial \eta}{\partial t} = 0 \tag{3.19}$$

The solution (Eq. 3.18) is a superposition of one bounded wave and two free waves. It implies that bounded wave propagates with the pressure and the other two free waves move independently. If the case of large speed (V→∞), the water surface elevation is low ($\eta \approx c^2\zeta_a/V^2$) and if pressure velocity is slow enough (V→0), the water surface elevation is almost stationary. On the other hand, in the case of equality of pressure velocity and wave speed, there are special situation resonance occurs and highest wave elevation is observed (formally infinite in the model).

If the Eq. (3.18) is simplified, basically the result is

$$\frac{Q}{P} = \frac{V^2-c^2}{2(V-c)c} = \frac{V+c}{2c}\,. \tag{3.20}$$

With this ratio of frontal wave amplitudes (Q) with respect to rear wave (P), the model can be verified. To be more illustrative, sketch of the problem is given in the Figure 3.1.

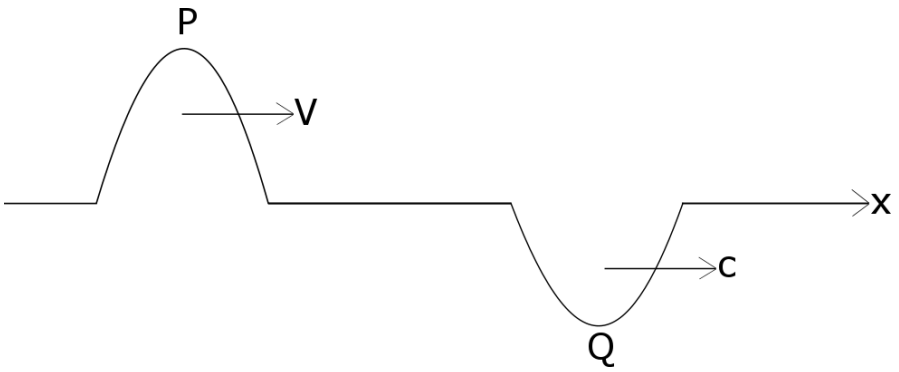

Figure 3.1. General sectional view of the propagation of long wave generated by moving constant atmospheric pressure

3.3. Numerical Model

The disturbances of the atmospheric pressure on the water body can cause the long waves. The three distinctions are important for the long waves: the generation of the wave, propagation of the wave in the deep water and wave propagation in the shallow water and on the shore. Long waves are generally expressed with shallow water equations because the supportive idea behind the shallow water equations is that progressive wave length is bigger than water depth. The wave propagation in the deep water can be explained by linear shallow water equations, while in the shallow water it is defined by non-linear shallow water equations. Non-linearity of this equation means that the surface and bottom stresses, Coriolis force and shoaling cannot be ignored (Eze et. al., 2009).

To solve tsunamis (long wave) mostly generated by earthquakes and landslides, there are several numerical models such as COMCOT (Liu et. al., 1994; 2008), TUNAMI-N2 (Imamura, 1996; Imamura et al., 2006), MOST (Titov and Synolakis, 1998), NAMI DANCE (NAMI DANCE Manual, 2010; Kian et.al., 2014) which use shallow water wave equations; FUNWAVE (Kirby et. al., 1998), GEOWAVE (Watts et. al., 2003) that use Boussinesq equations. The aforementioned numerical models are

developed for numerical solution of co-seismic and/or landslide generated tsunamis without considering atmospheric pressure disturbance.

In the present study, non-linear shallow water equations containing the air pressure forcing term are solved numerically to simulate generation, propagation and coastal amplification of long waves and therefore the atmospheric pressure differences are directly included in the solution. In this direction, a new module is inserted in the tsunami numerical code NAMI DANCE and a new version NAMI DANCE-P is created. NAMI DANCE is developed in collaboration with Ocean Engineering Research Center, Middle East Technical University, Turkey and Institute of Applied Physics, Russian Academy of Science, and Special Research Bureau for Automation of Marine Researches, Far Eastern Branch of Russian Academy of Sciences, Russia. It computes main tsunami hydrodynamic parameters which are (i) maximum positive amplitude, (ii) maximum flow depth, (iii) maximum current velocity, (iv) maximum of momentum flux, (v) maximums of hydrodynamic forces, (vi) maximum negative amplitude, (vii) maximum wave arrival time, (viii) initial wave arrival time and (ix) inundation and withdrawal of tsunami durations (Yalciner et al., 2015).

Generally, in the numerical calculations of NAMI DANCE, when the boundary conditions can be given accurately, the open sea boundary is set in the deep sea. Moreover, gridding distances affect the time efficiency of CPU, coarser grids in the deep sea and finer grids in nearshore should be used. At the boundary of different gridding distances, continuation of calculation is necessary. The wave equation for which CFL condition should be satisfied stability of the numerical calculation is given in equation (3.28).

$$\frac{\Delta x}{\Delta t} = \sqrt{2gh_{max}} \tag{3.21}$$

where Δx and Δt are the spatial and temporal grid lengths, and $h_{max}$is the maximum water depth, it is getting smaller while approaching to the shore. In this equation $c_{max} = \sqrt{gh_{max}}$ is multiplied by $\sqrt{2}$ to be on the safe side. Then, to satisfy the CFL

condition smaller x should be determined with constant Δt. This is the usual approach to specify Δx and Δt, if there is no run-up. In the case of run-up, not only Δx but also Δt are changed to satisfy the CFL condition.

Generally, in the model, wave propagation is solved using following boundary conditions and the kinetic and dynamic conditions at surface and bottom are given in equation (3.22-3.24).

$$p = 0 \quad at\ z = \eta \tag{3.22}$$

$$w = \frac{\partial \eta}{\partial t} + u\frac{\partial \eta}{\partial x} + v\frac{\partial \eta}{\partial y} \quad at\ z = \eta \tag{3.23}$$

$$w = -u\frac{\partial h}{\partial x} - v\frac{\partial h}{\partial y} \quad at\ z = -h \tag{3.24}$$

On the other hand, in open boundary conditions, water surface displacement or discharge flux is used as a forced input at the boundary.

The new version of the model solves the non-linear shallow water equations in both Cartesian and spherical coordinates. The set of two-dimensional equations with atmospheric pressure terms in Cartesian coordinates are given in Eq. 3.25-3.27.

$$\frac{\partial \eta}{\partial t} + \frac{\partial M}{\partial x} + \frac{\partial N}{\partial y} = 0 \tag{3.25}$$

$$\frac{\partial M}{\partial t} + \frac{\partial}{\partial x}\left(\frac{M^2}{D}\right) + \frac{\partial}{\partial y}\left(\frac{MN}{D}\right) + gD\frac{\partial \eta}{\partial x} + \frac{\tau_x}{\rho} + \frac{D}{\rho}\frac{\partial P_{atm}}{\partial x} = 0 \tag{3.26}$$

$$\frac{\partial N}{\partial t} + \frac{\partial}{\partial x}\left(\frac{MN}{D}\right) + \frac{\partial}{\partial y}\left(\frac{N^2}{D}\right) + gD\frac{\partial \eta}{\partial y} + \frac{\tau_y}{\rho} + \frac{D}{\rho}\frac{\partial P_{atm}}{\partial y} = 0 \tag{3.27}$$

where t is time, η is water surface elevation, ρ is the density of water, D is the water depth, P_{atm} is the atmospheric pressure in Pascal, τ_x and $\tau_y$are the bottom shear

stresses and M and N are the discharge fluxes in the x and y directions which are also given in the following.

$$M = \int_{-h}^{\eta} u dz = u(D+\eta) = uD, \;\; N = \int_{-h}^{\eta} v dz = v(D+\eta) = vD \qquad (3.28)$$

In this Eq. (3.28), current velocities u and v are in x and y directions, respectively. The bottom shear stresses are computed with equations below (Eq. 3.29 and Eq. 3.30).

$$\frac{\tau_x}{\rho} = \frac{fn^2}{(\eta+D)^{7/3}} M\sqrt{M^2+N^2} \qquad (3.29)$$

$$\frac{\tau_y}{\rho} = \frac{fn^2}{(\eta+D)^{7/3}} N\sqrt{M^2+N^2} \qquad (3.30)$$

Within the equations (3.29 and 3.30), f denotes the bottom friction and Manning's coefficient, n is calculated by using following equation.

$$n = \sqrt{\frac{f(\eta+D)^{1/3}}{2g}} \qquad (3.31)$$

In the numerical model, for the specified bathymetry and initial sea surface, the additional input is barometric pressures at sea level in Pascal at certain time intervals (preferably in one hour time interval according to the available data). Then, NAMI DANCE-P computes spatial distribution of pressure at every grid at each time step by interpolating the respective pressure values between the inputted pressures at previous hour and next hour.

Accordingly, as an output, NAMI DANCE-P calculates minimum and maximum water surface elevations, current velocities and their directions, momentum fluxes and their directions and water depths for the specified coordinates by using previously user defined time intervals and duration of simulation same by NAMI-DANCE .

3.4. Verification of the Model

In order to verify numerical model and to make sure that the model correctly calculates the water surface elevations due to the effect of atmospheric pressure disturbances, simulations are conducted for regular shaped flat bathymetry using the propagation of a rectangular shaped pressure system (rectangular shaped high pressure band with a constant pressure velocity). In order to verify the performance and accuracy of the numerical solutions tests are performed with regular shaped flat bathymetry (500m constant depth) and with enclosed by North and South solid boundaries (Figure 3.2-3.3). The reason why these types of inputs are selected is the existence of analytical solution. Therefore, the results can be analyzed to compare the results of analytic and numerical solutions.

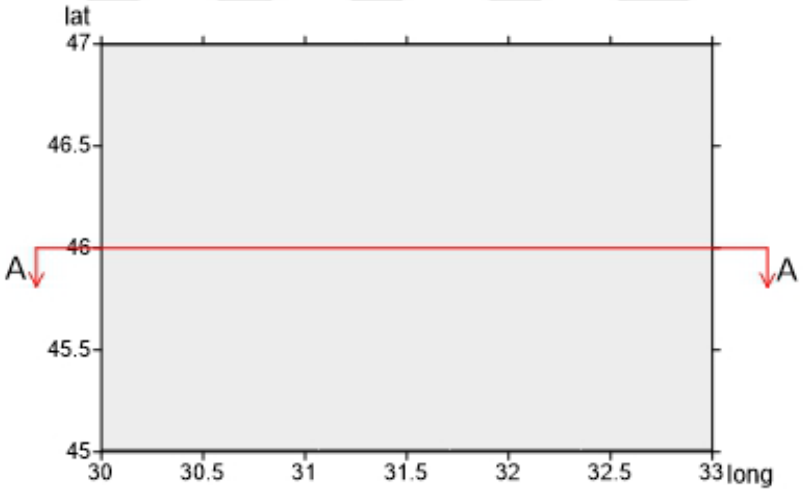

Figure 3.2. Top View of the Flat Bathymetry

The clear verification of the numerical model can be made by comparing the analytical and numerical results using constant pressure speed (V) and constant wave celerity (c). Therefore in the cases different alternatives of V and constant value of c 70 m/sec over 500m constant depth basin are selected. Those will also help to obtain analytical solutions.

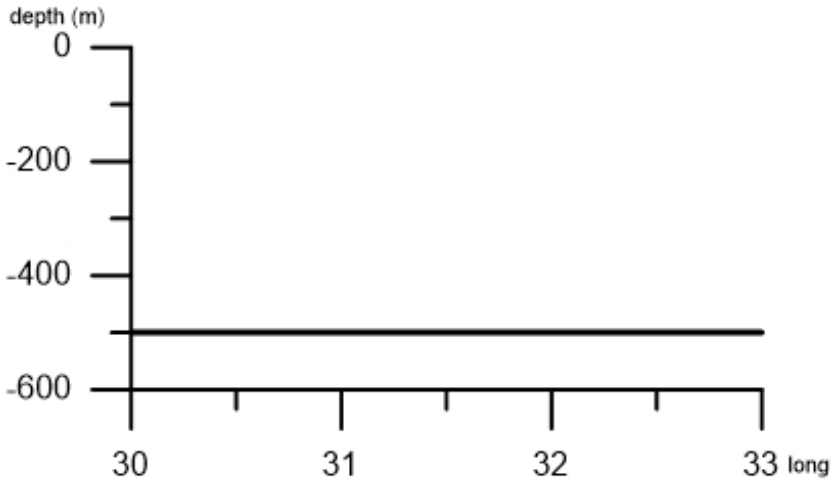

Figure 3.3. Sectional View of the Flat Bathymetry

Three different cases (V is faster, equal and slower than c) are investigated using the same regular shaped flat bathymetry and pressure band. The pressure band which has 46.6 km width, and propagates from left to right with maximum 102000 Pascal pressure and a specified constant velocity is defined. Top and sectional views of the pressure band are shown in Figure 3.4-3.5.

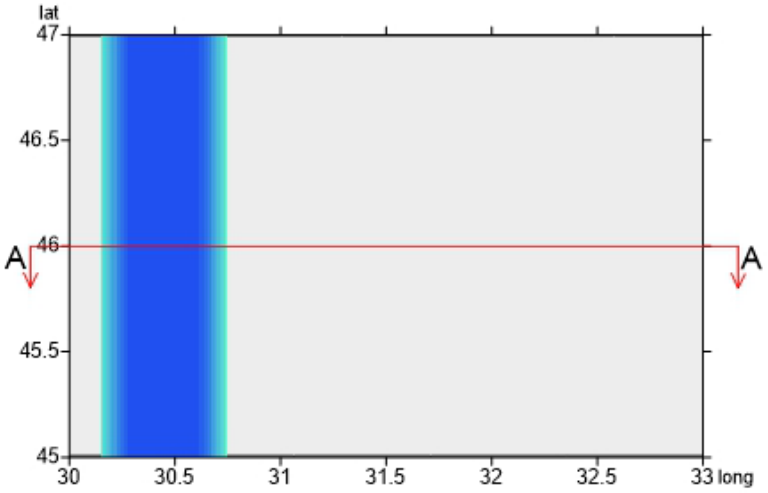

Figure 3.4. Top View of the Pressure Band on the Flat Bathymetry

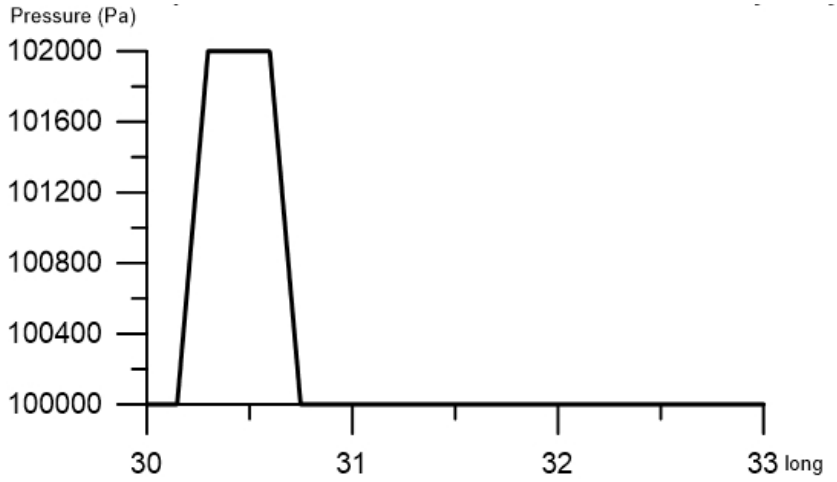

Figure 3.5. A-A Sectional View of the Pressure Band on the Flat Bathymetry

Before the simulations, bathymetry and pressure data are formed in the numerical structure of 200 m spatial grid size. At the beginning of the simulation, pressure data are given to the program as an input by one hour time interval. Then, 3 different tests are conducted by selecting the time step as 1 second and the duration of the simulations are determined as 20 minutes. In the simulations, pressure velocity (V) is selected as 200 m/sec, 70 m/sec and 40 m/sec, respectively. The wave celerity (c) is same for all models and it is 70 m/sec. At the end of the simulations, for every grid points, water surface elevations and current velocities are determined at every 60 seconds. The results of the computed water surface elevations and water velocities are presented as a graph at every 300 second intervals for the three different simulations (Figure 3.6-3.8).

Case 1: Pressure velocity is bigger than the wave celerity (V>c),

Case 2: Pressure velocity equals to wave celerity (V=c),

Case 3: Pressure velocity is smaller than the wave celerity (V<c).

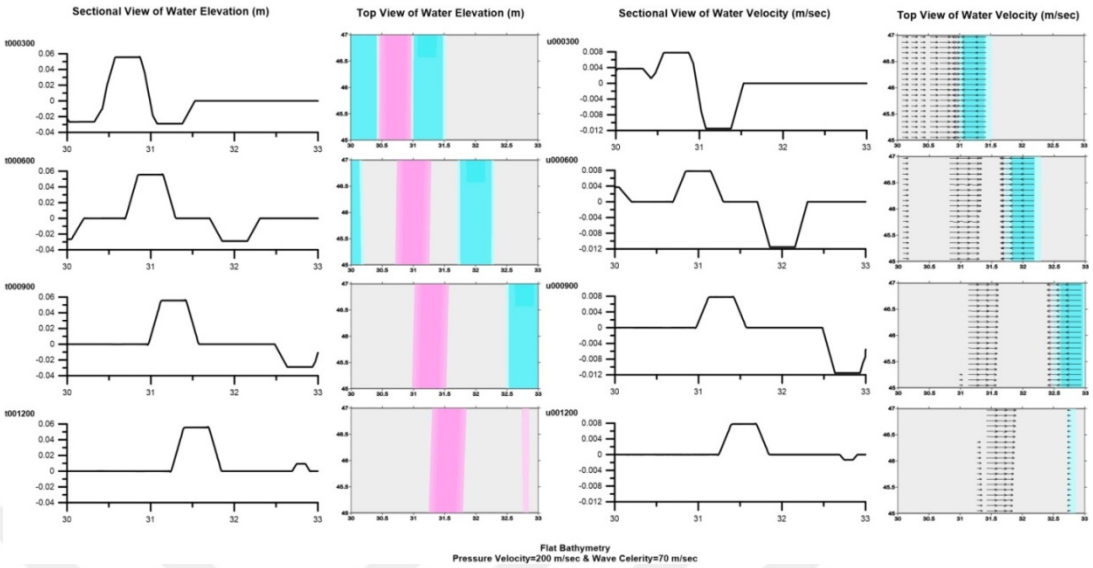

Figure 3.6. Case 1 for the Flat Bathymetry with V=200 m/sec and c=70 m/sec.

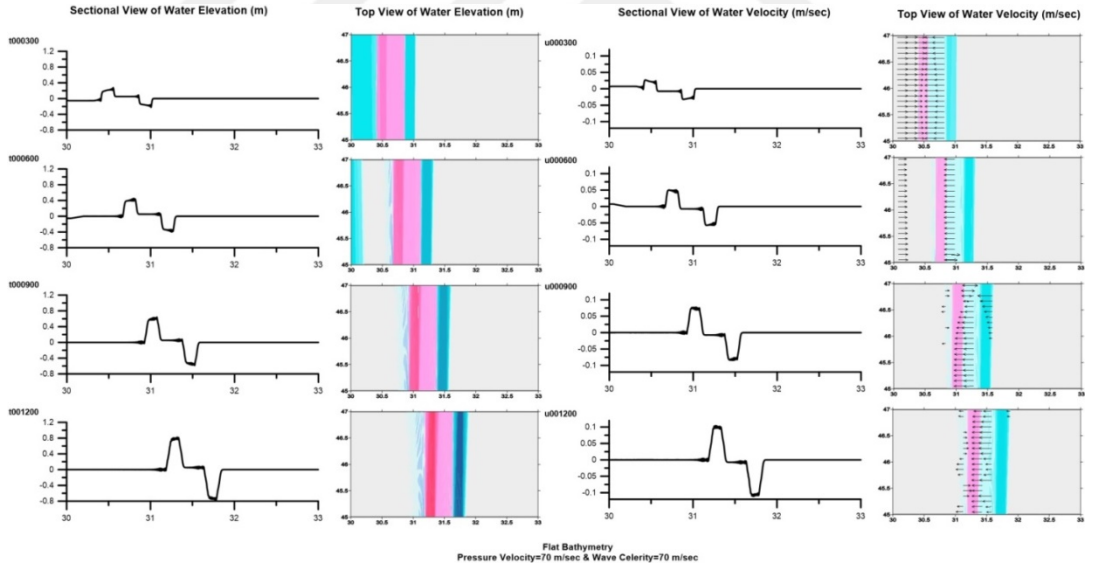

Figure 3.7. Case 2 for the Flat Bathymetry with V=70 m/sec and c=70 m/sec.

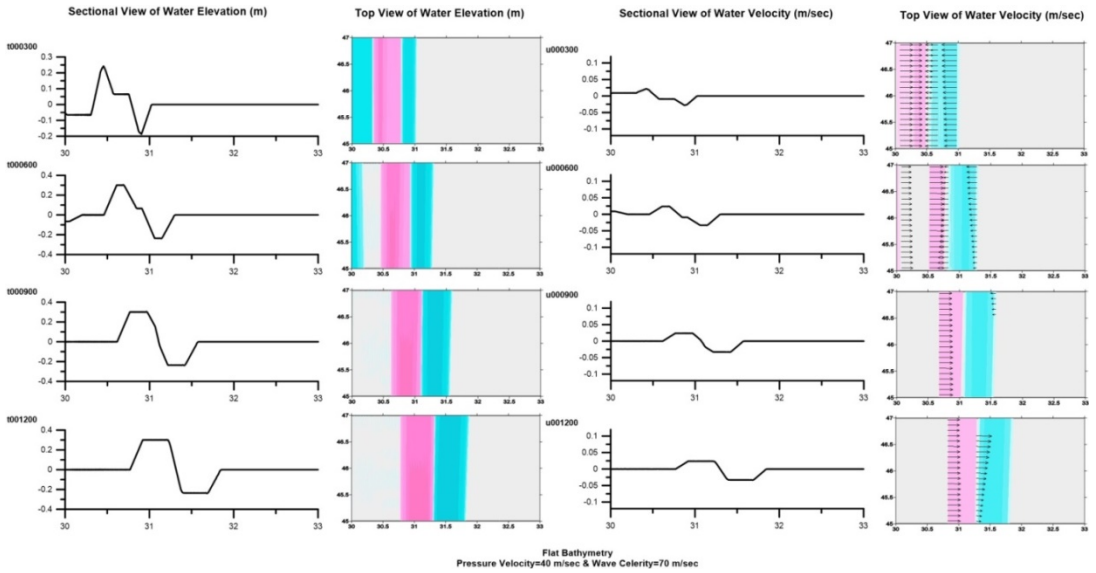

Figure 3.8. Case 3 for the Flat Bathymetry with V=40 m/sec and c=70 m/sec.

To verify the accuracy of the numerical model results, the numerical results are compared with analytic results obtained from Eq. (3.20) at 20 minutes (Table 3.1). For the Case 1, the ratio of the amplitudes of frontal wave due to wave celerity (Q) with respect to rear wave due to pressure (P) at 20 minutes is analytically calculated as 1.92. When the amplitudes obtained from the numerical model are proportioned with each other, this ratio (Q/P) is founded as 1.96. The percent error is 2.1. It means that results are in quite reasonable correlation for the Case 1. Similarly, in the case of pressure velocity equals to wave celerity (Case 2), the Q/P ratio at 20 minutes for both numeric and analytic solutions is calculated as 1. There is almost no percentage error is observed. For the Case 3 (pressure velocity is smaller than wave celerity), the ratio of Q/P is computed as a 0.79 in the analytic solution when the time reaches 20 minutes. On the other hand, for the same conditions, the Q/P ratio is obtained as 0.77, numerically. The percentage error is obtained as 2.5 in Case 3, it means that acceptable correlation. When all numeric and analytic Q/P ratios are compared, it can be stated that values are in consistent with each other and it means that the numerical model makes reasonable calculations. In other words, numeric results are in agreement with the analytic results and also this agreement is verified by using flat

bathymetry. Also, large sizes of figures which show sea states at different time steps for flat bathymetries are given in Appendix-A.

Table 3.1. Comparison of the Numeric and Analytic Q/P values at 20 minutes

	Q/P at t=20 min		
	Case 1 (V>c)	*Case 2 (V=c)*	*Case 3 (V<c)*
Numeric Solution	1.96	1	0.77
Analytic Solution	1.92	1	0.79
% Error	2.1	~ 0	2.5

CHAPTER 4

NUMERICAL TESTS FOR DIFFERENT TYPES OF BASINS

This chapter covers different simulations for different bathymetries to investigate the effects of bathymetries on the amplification of long waves generated by atmospheric pressure differences. Four different bathymetries are determined for the simulations: (i) triangular bathymetry, (ii) stepwise shelf bathymetry, (iii) upward sloping and (iv) downward sloping bathymetry.

4.1. Triangular Bathymetry Simulations

The generated triangular bottom bathymetry has changed from 500 m depth to ground level in two sides of the bathymetry with a 1/200 slope. The top and sectional views of the triangular bathymetry are given in the Figure 4.1 and Figure 4.2.

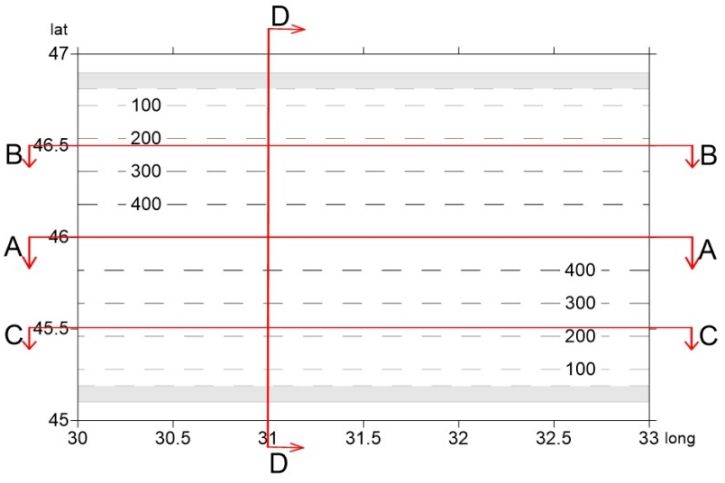

Figure 4.1. Top View of the Triangular Bathymetry

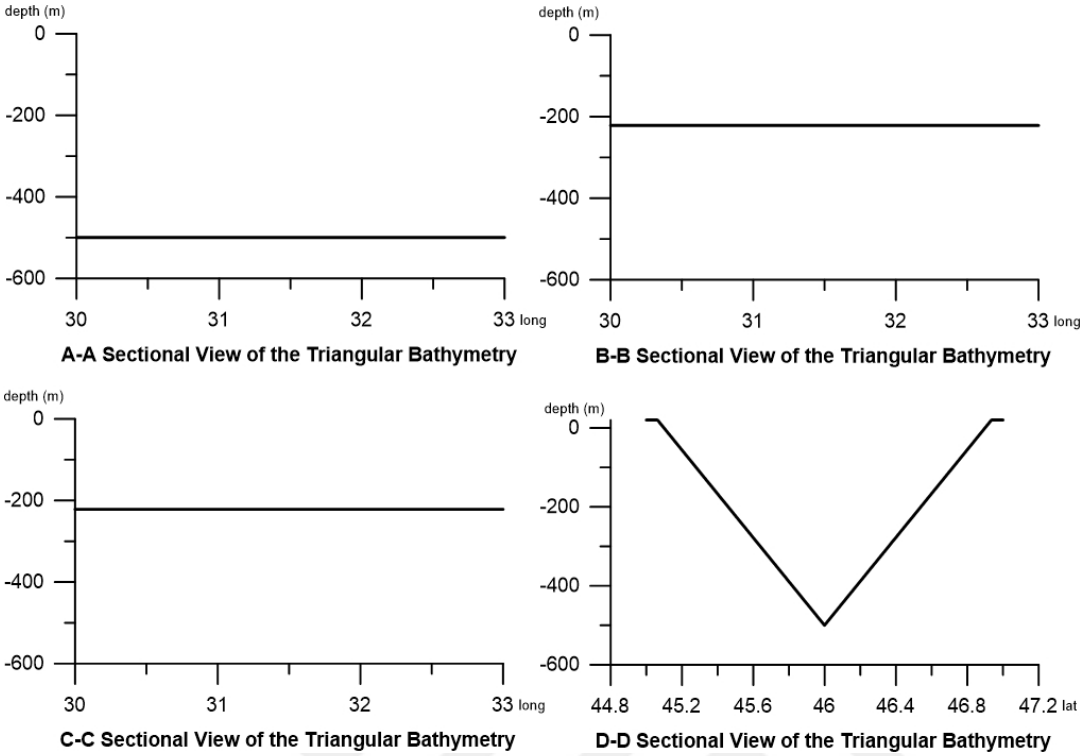

Figure 4.2. Sectional View of the Triangular Bathymetry

The triangular bathymetry is obtained with a 200 m grid size. Then, using the same grid size, pressure data are generated as a 102000 Pascal high pressure band with 46.6 km width. Pressure band is moving from left to the right with a certain velocity which is determined by user in the program. Three different cases are conducted for the triangular bathymetry: in the first case, pressure velocity is determined as faster than wave celerity; for the second case pressure velocity and wave celerity are equal each other; in the third case pressure velocity is selected as slower than wave celerity. The top and sectional view of the pressure band is in the following.

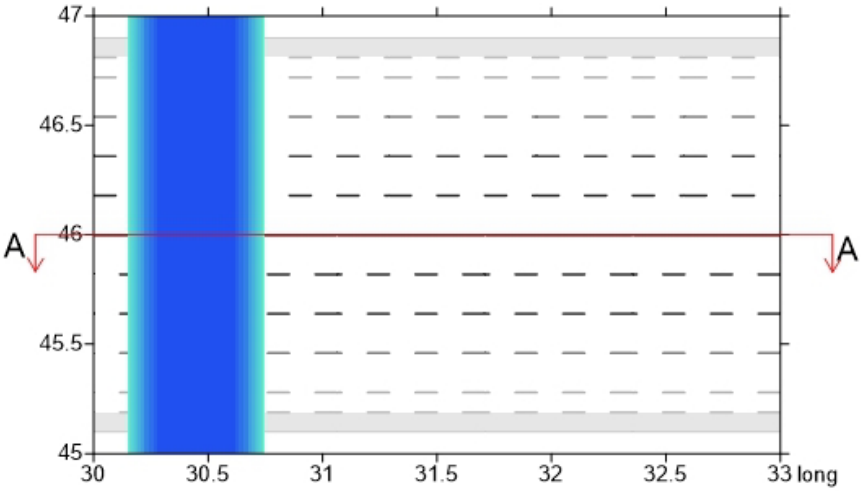

Figure 4.3. Top View of the Pressure Band on the Triangular Bathymetry

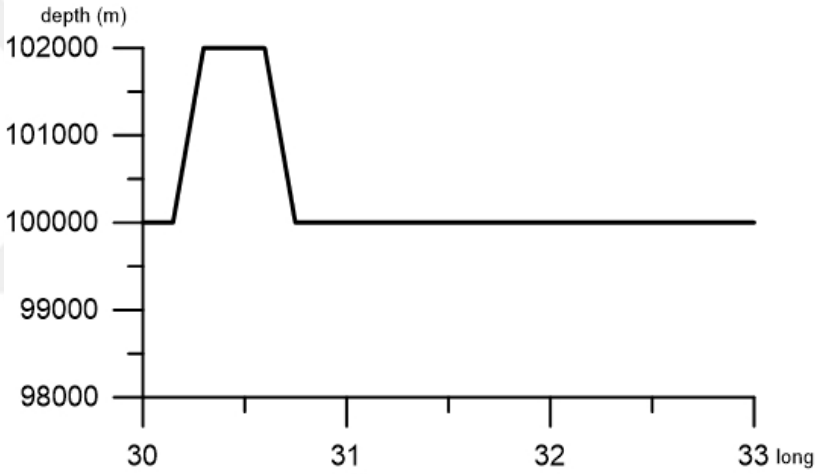

Figure 4.4. A-A Sectional View of the Pressure Band on the Triangular Bathymetry

While pressure propagates towards to the right with a constant speed, numerical program calculates water surface elevations, current velocities and their directions for the specified coordinates by using 1 second time interval and 60 minutes simulation duration. In the Case 1, V is taken as 200 m/sec and bigger than the maximum c is 70 m/sec. The results for the water surface elevations and current velocities are given in the Figure 4.5.

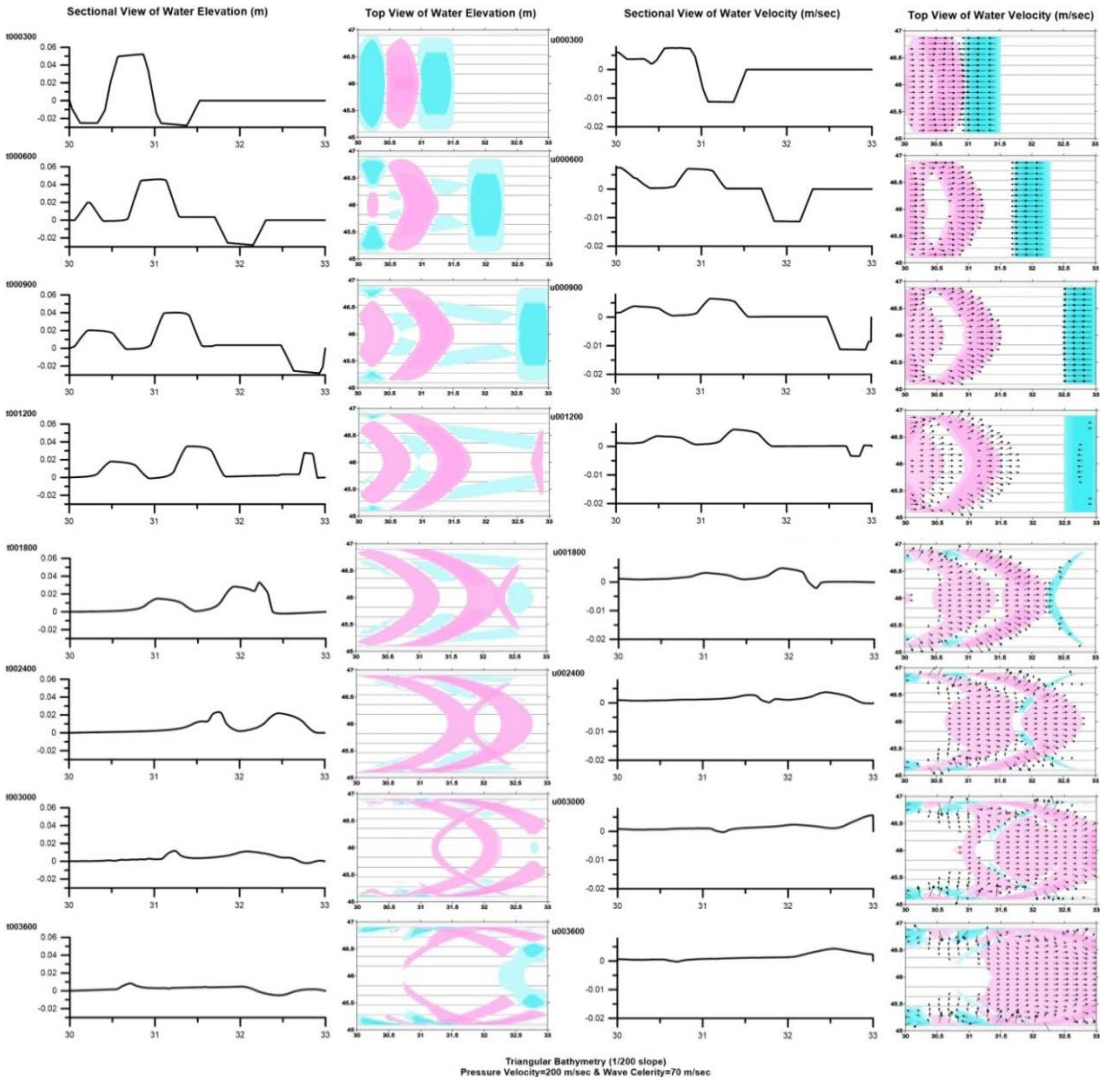

Figure 4.5. Top and Sectional Views of the Water Elevations and Water Velocities on the Triangular Bathymetry (Case 1, V=200 m/sec and c_{max}=70 m/sec)

It is expected that wave move faster in the 500 m water depth and when these results are analyzed, and it was seen that the expectation is satisfied. There are variations in the wave celerity at different coordinates, so that water elevations show instability. While water elevation is around 5 cm at 5 minutes, it approaches to the stagnant water levels at the end of the 1 hour simulation. Similarly, water velocity decreases towards to end of the simulation. In the case of equality of V and c_{max} (Case 2), the highest water surface elevations were observed and results are given in the below Figure 4.6.

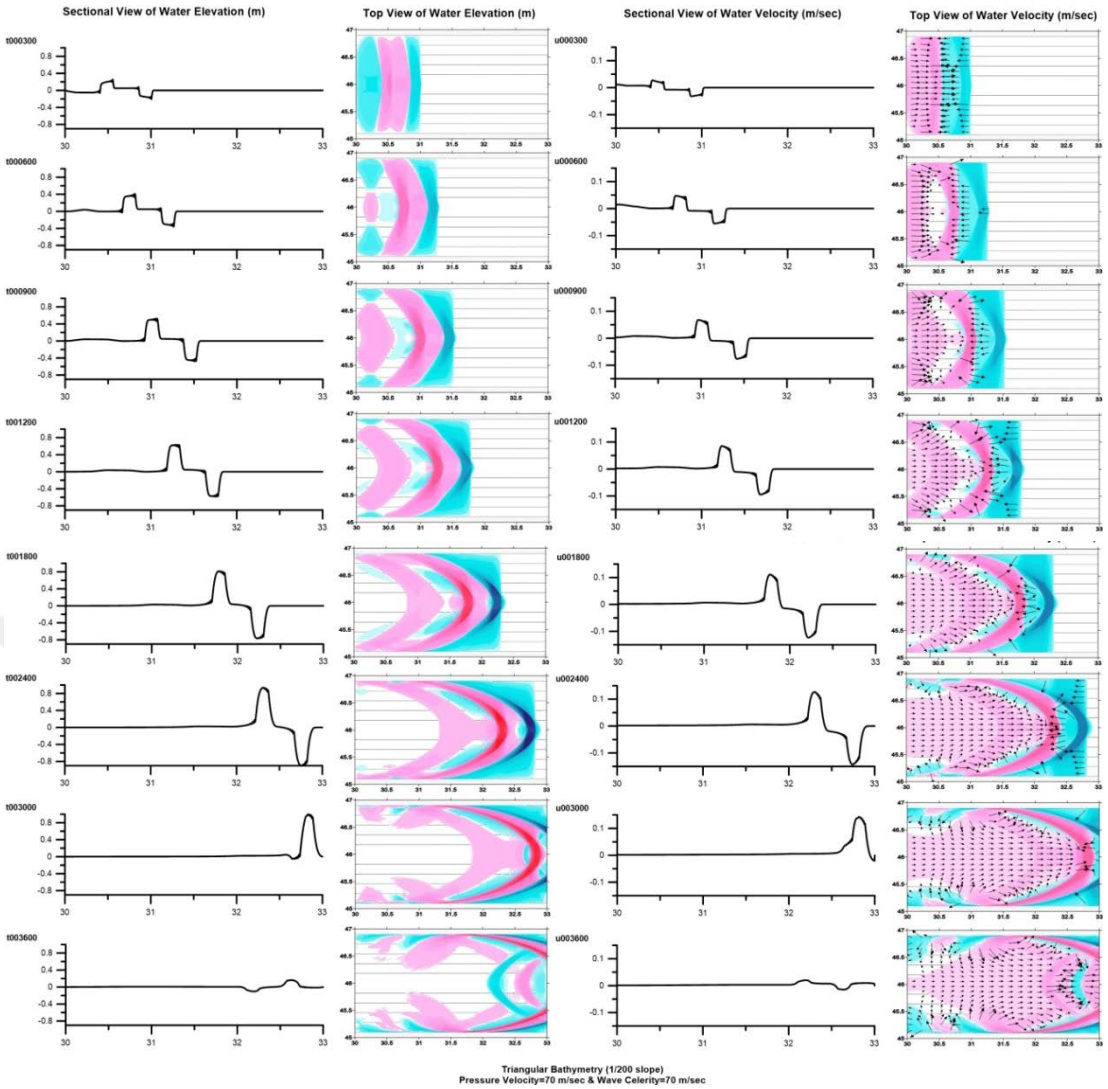

Figure 4.6. Top and Sectional Views of the Water Elevations and Water Velocities on the Triangular Bathymetry (Case 2, V=70 m/sec and c_{max}=70 m/sec)

From the beginning of the pressure movement, waves increasingly proceed until the 1 hour of the simulation. At first, the water surface elevation level was around 20 cm; then at 50 minutes, it reached up almost 1 meter. The maximum water velocity was around 15 cm/sec and was reached to it at the end of the simulation. On the other hand, in the Case 3, pressure velocity propagates with 40 m/sec behind the maximum wave celerity from left to right. The below figure (Figure 4.7) shows water surface elevation and water velocity as a result of Case 3 is in the following.

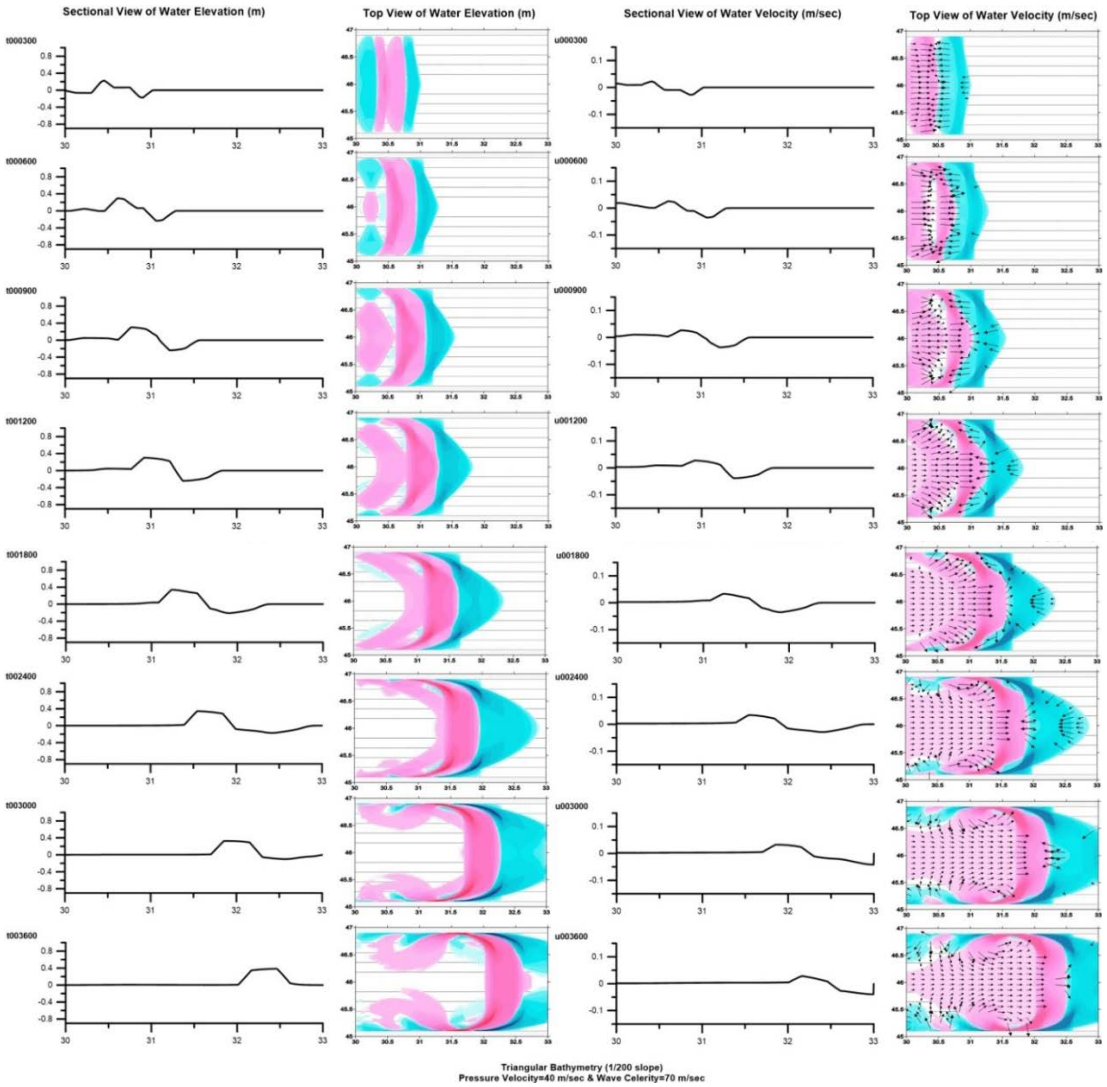

Figure 4.7. Top and Sectional Views of the Water Elevations and Water Velocities on the Triangular Bathymetry (Case 3, V=40 m/sec and c_{max}=70 m/sec)

At the beginning of the simulation, 22 cm wave height amplifies up to 38 cm at the center of the bathymetry. During the simulation, waves are reflected from the upper and lower boundary of the bathymetry and it can be observed after 20 minutes. In this case, water velocities are in the same magnitude at every time step. However, for the Case 3, maximum wave elevation observed near the upper and lower boundaries because towards southern and northern boundaries, horizontal wave movement is getting slower and the equality between V and c is observed. Then, the maximum wave height calculated as 80 cm in the Case 3.

In general, when the results of three different cases are compared, it was obtained that maximum water elevations and water velocities are observed at different time steps. The maximum water elevations are 5.2 cm at 5 minutes, 1 m at 50 minutes and 38.5 cm at 60 minutes respectively for Case 1, Case 2 and Case 3 at center of the bathymetry. The deterministic phenomenon for the maximum water elevation is the overlapping of the pressure period and wave period. In the Case 1, water surface elevations are in low levels due to the faster pressure velocity. On the other hand, in the second case, the highest water elevation was observed due to the equality of pressure velocity and wave celerity. It is also explained by Proudman resonance (Proudman, 1929) where pressure wave frequencies match up with the eigenfrequencies of the basin and then causes damaging oscillations. The present situation is exemplified by the Figure 4.8. In the example case, pressure velocity is taken as 40 m/sec. When the points where wave celerity is 40 m/sec are marked, we observed that the maximum water elevations are observed on these marked points. Finally, in the Case 3, resonance between the atmosphere and the ocean was seen earlier than the other simulations; because pressure moves slower in the present simulation.

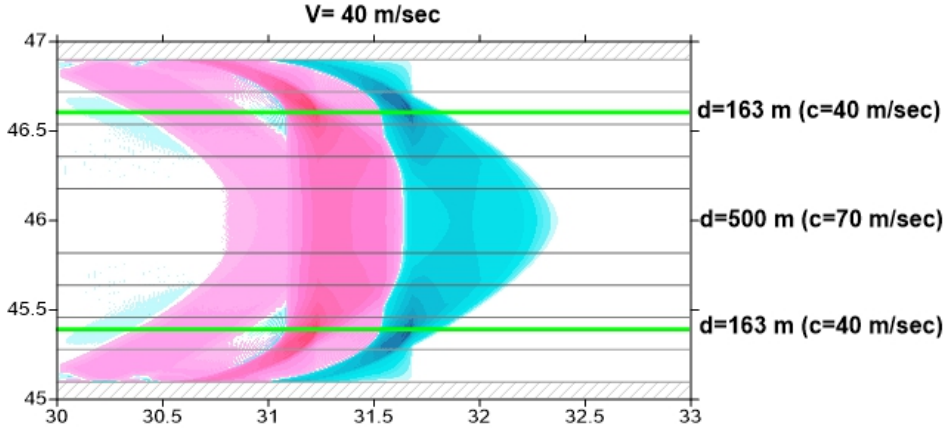

Figure 4.8. Top View of the Maximum Water Elevations on the Triangular Bathymetry (V=40 m/sec and c_{max}=70 m/sec)

4.2. Stepwise Shelf Bathymetry Simulations

4.2.1. Stepwise Shelf Bathymetry with 1:10 Shelf Slope

In the present study, bathymetry is composed of three different parts; 500 m depth flat bottom, 1/10 steep slope part from 500 m depth to 50 m depth and then 50 m depth flat bottom. The basin is bounded at the northern and the southern. The top and sectional views of the stepwise shelf bathymetry with 1/10 shelf slope are shown in the Figure 4.9 and Figure 4.10.

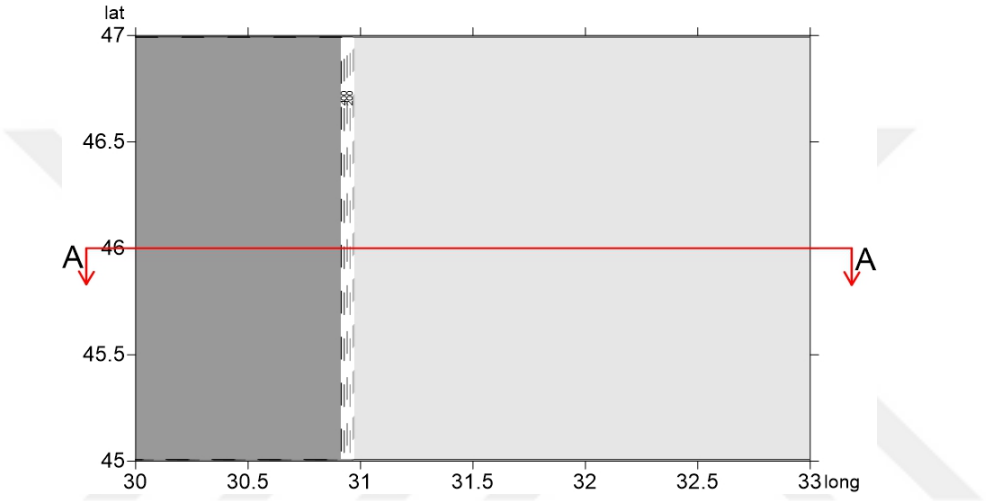

Figure 4.9. Top View of the Stepwise Bathymetry with 1:10 Shelf Slope

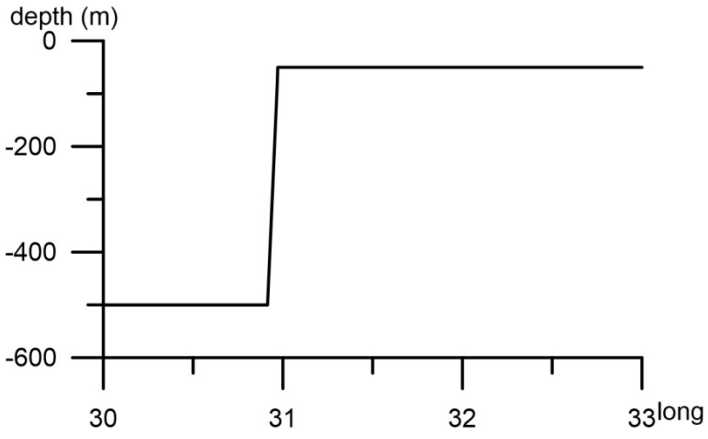

Figure 4.10. A-A Sectional View of the 1:10 Bottom Slope Stepwise Shelf Bathymetry

The initial pressure has 46.6 km width and 102000 Pascal high pressure value and it moves as a band from the west to the east with constant velocity. The top and sectional views of pressure band are shown in the Figure 4.11 and Figure 4.12. As flat and triangular bottom bathymetries, pressure data are generated with 200 m grid size.

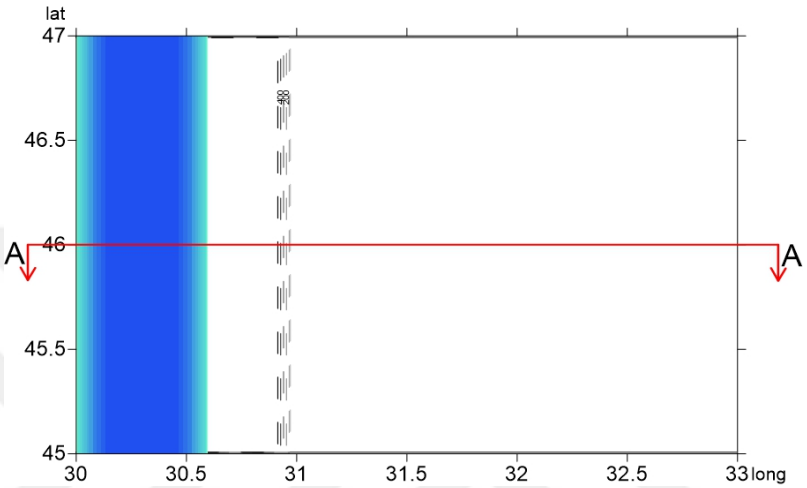

Figure 4.11. Top View of the Pressure Band on the Stepwise Shelf Bathymetry with 1:10 Shelf Slope

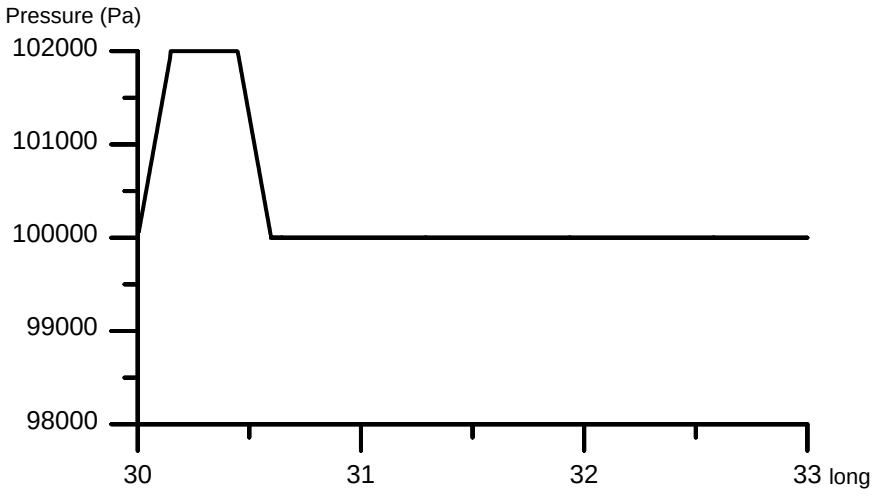

Figure 4.12. A-A Sectional View of the Pressure Band on the Stepwise Shelf Bathymetry with 1:10 Shelf Slope

Stepwise shelf bathymetry with 1/10 slope is simulated for three different cases (V is faster, equal or slower than wave celerity). The change in the sea level is calculated at t= 300, 600, 900, 1200, 1800, 2400, 3000 and 3600 seconds. Also, water velocities are calculated and presented at each time step. In the Case 1, V is 200 m/sec and it is greater than the c values. In the Figure 4.13, top and sectional views of the water elevation and water velocity on the 1/10 bottom slope stepwise shelf bathymetry for Case 1 are shown.

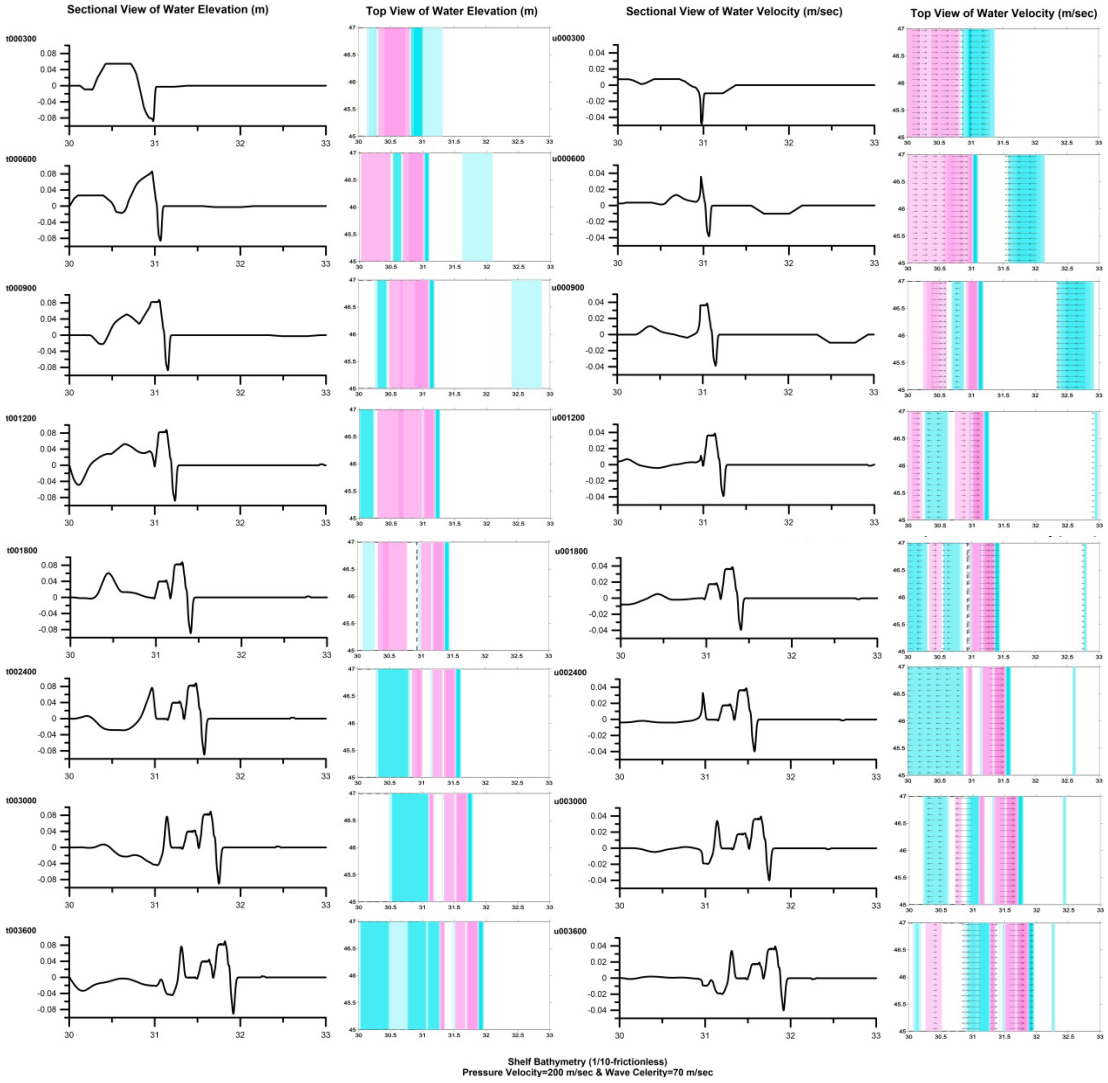

Figure 4.13. Top and Sectional Views of the Water Elevations and Water Velocities on the Stepwise Shelf Bathymetry with 1:10 Shelf Slope (Case 1, V=200 m/sec and c_{max}=70 m/sec)

When the results are considered for Case 1, the initial wave begins to move to shelf region with 5.5 cm wave height at the 5 minutes. At 10 minutes, wave height increases rapidly and its value becomes 8.6 cm. Then until end of the simulation, the wave height does not show any significant difference. At the end of the simulation maximum water elevation is computed which is 8.95 cm.

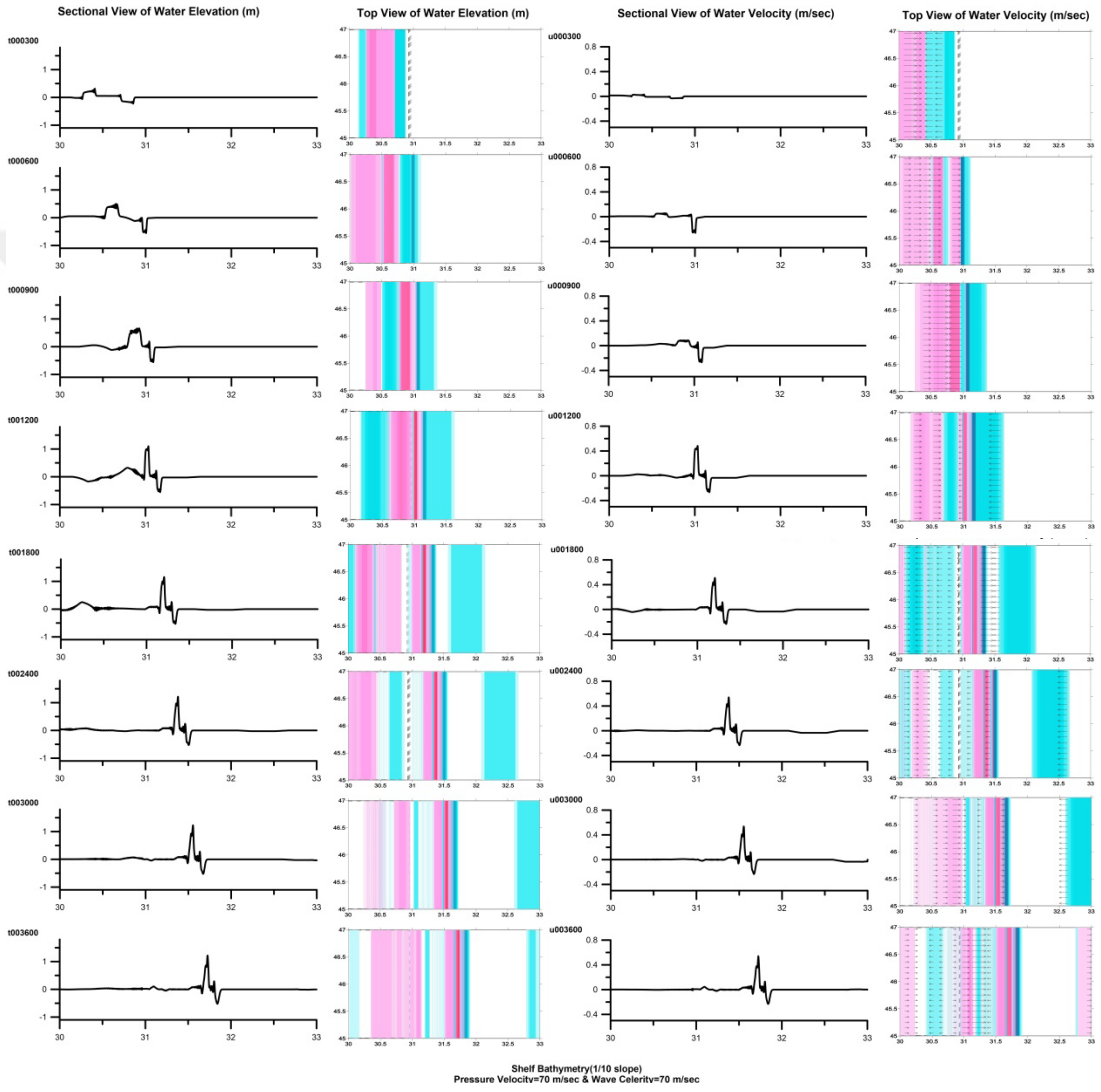

Figure 4.14. Top and Sectional Views of the Water Elevations and Water Velocities on the Stepwise Shelf Bathymetry with 1:10 Shelf Slope (Case 2, V=70 m/sec and c_{max}=70 m/sec)

Secondly, in the Case 2, the pressure velocity and maximum wave celerity are equal each other and 70 m/sec. The results for the effects of the stepwise shelf bathymetry on the water elevation and velocity for the Case 2 are shown in the following (Figure 4.14). In the Case 2, atmospheric pressure disturbance speed and speed of the free disturbance in the water are identical. Therefore, Proudman resonance occurrs and water surface elevations take their higher values. At the beginning of the simulation, the wave has 31.5 cm wave height and 3.05 cm/sec velocity. At 10 minutes, wave height is calculated as 49.5 cm. Then, at 15 minutes wave propagates over the shelf and it reaches 65.9 cm by 8.7 cm/sec velocity. Thereafter, wave height is slightly increasing until end of the simulation. At 60 minutes, maximum wave height is computed as 1.22 m. In the Case 2, steep slope effect and Proudman resonance caused higher amplifications.

In the Case 3, V is used as 40 m/sec, slower than the maximum wave celerity. The results are given in the Figure 4.15.

When the results of Case 3 are investigated due to the slower pressure velocity, wave heights are bigger than the Case 1. Specifically, at 5 minutes, initial wave amplitude is 24.4 cm and it propagates by 2.2 cm/sec velocity. Then, at 10 minutes, wave height is observed almost 30 cm. At 15 minutes, wave height beyond the shelf decreases and approximately 20 cm. At 20 minutes, wave meets by steep slope shelf then; wave height becomes 40 cm suddenly and moves by 14 cm/sec velocity. At the end of the simulation maximum water surface elevation is calculated as almost 50 cm.

In all of the three cases of the stepwise shelf bathymetry are considered, at the location where sloping part begins, the wave height increases rapidly. Among these three cases, the highest water surface elevations are observed in the Case 2 because of the equality of the V and c_{max} (so-called Proudman resonance). The minimum change in the water surface elevation is seen in the Case 1. Conversely, maximum oscillations are observed in the Case 2. On the other hand, the steep slope causes sudden increase in water surface elevation.

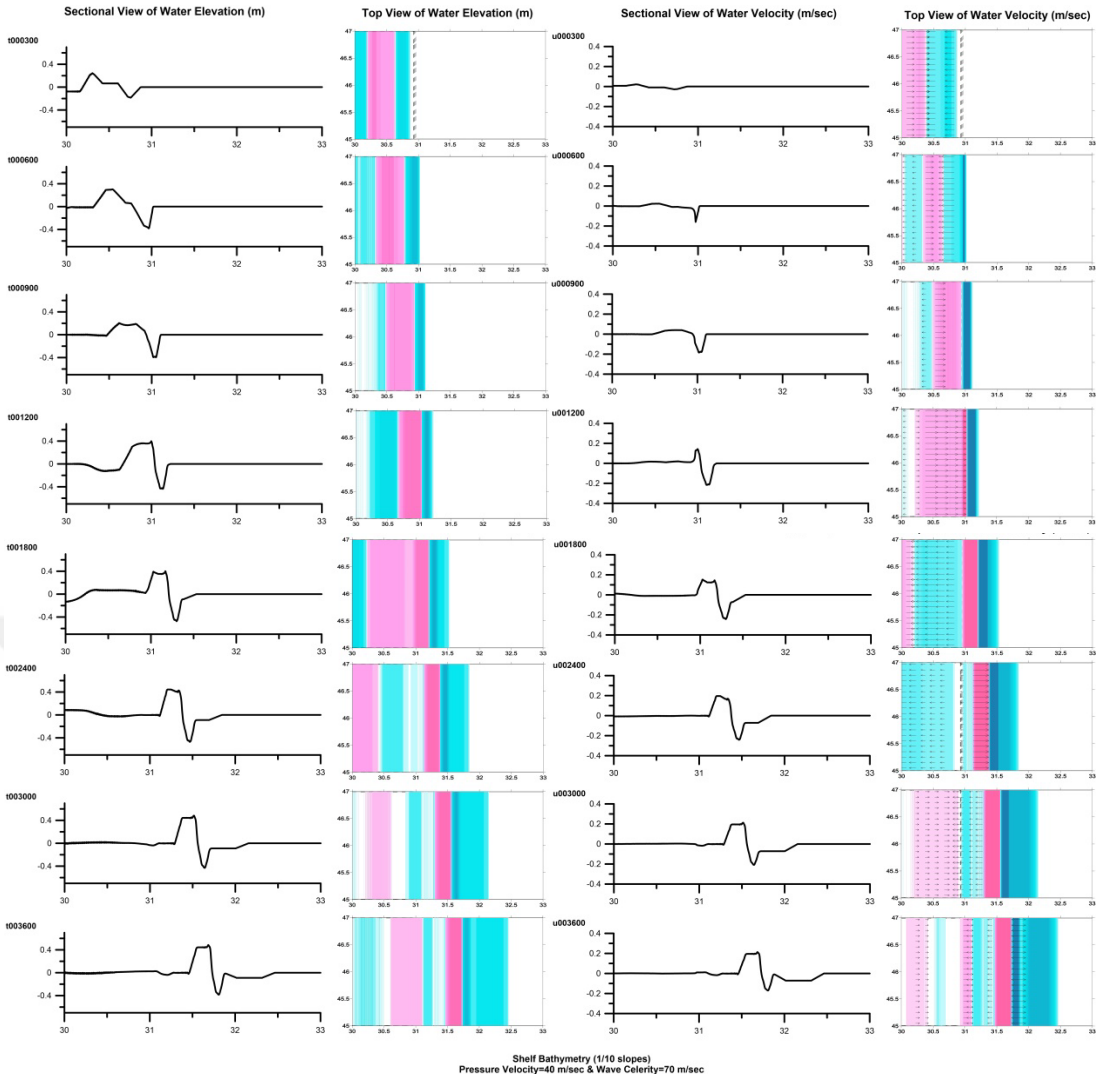

Figure 4.15. Top and Sectional Views of the Water Elevations and Water Velocities on the Stepwise Shelf Bathymetry with 1:10 Shelf Slope (Case 3, V=40 m/sec and c_{max}=70 m/sec)

4.2.2. Stepwise Shelf Bathymetry with 1:100 Shelf Slope

In the present case, the stepwise shelf bathymetry is composed of three different parts; 500 m depth flat bottom, 1/100 slope bottom from 500 m depth to 50 m depth and 50 m depth flat bottom. The basin is closed at the top and the bottom. The top and sectional views of the stepwise shelf bathymetry with 1/100 shelf slope are shown in the Figure 4.16 and Figure 4.17.

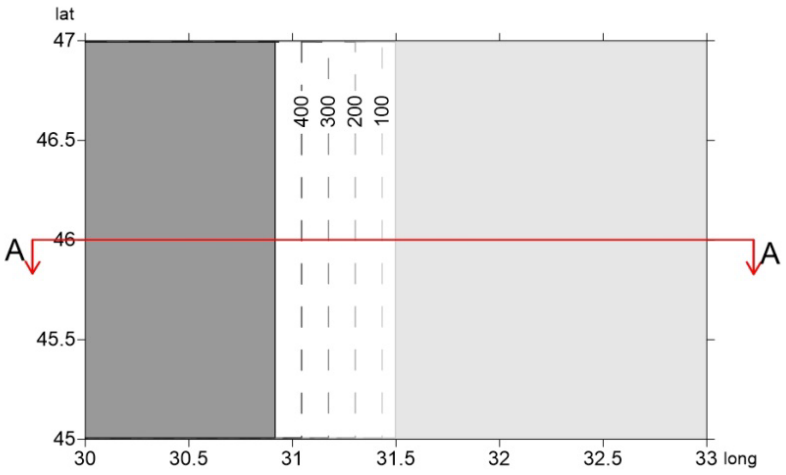

Figure 4.16. Top View of the Stepwise Bathymetry with 1:100 Shelf Slope

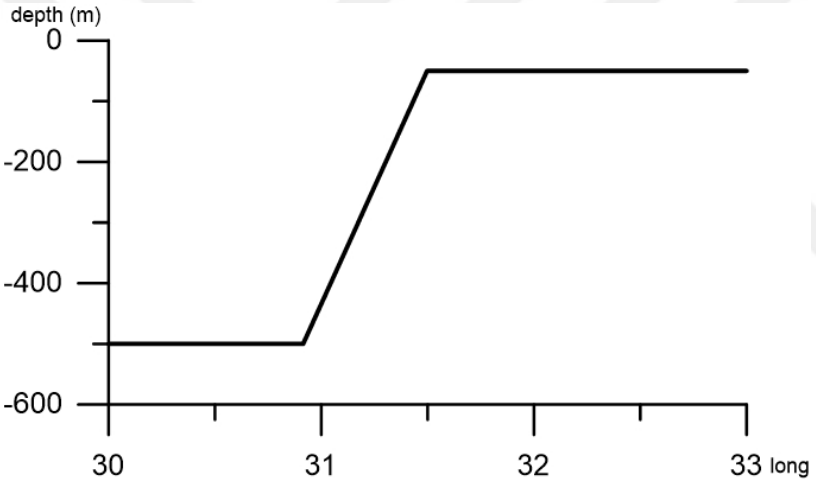

Figure 4.17. A-A Sectional View of the 1:100 Bottom Slope Stepwise Shelf Bathymetry

As an initial pressure, 46.6 km width 102000 Pascal high pressure band is used. The pressure band moves from the west to the east with fixed velocity. The top and sectional views of pressure band are shown in the Figure 4.18 and Figure 4.19. Similar to flat and triangular bottom bathymetries, stepwise shelf bathymetry and pressure data are generated using 200 m grid size.

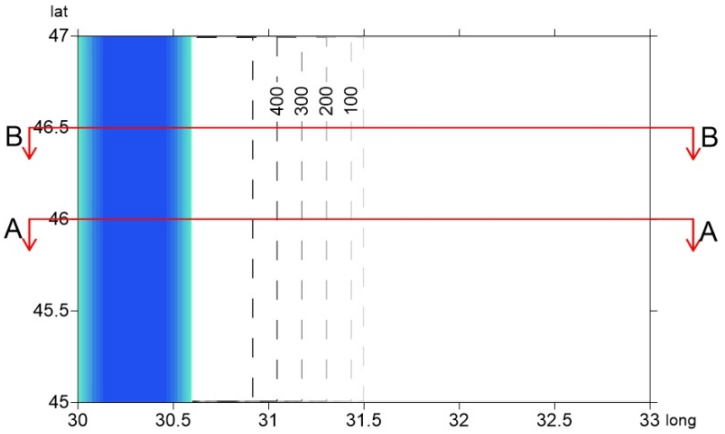

Figure 4.18. Top View of the Pressure Band on the Stepwise Shelf Bathymetry with 1:100 Shelf Slope

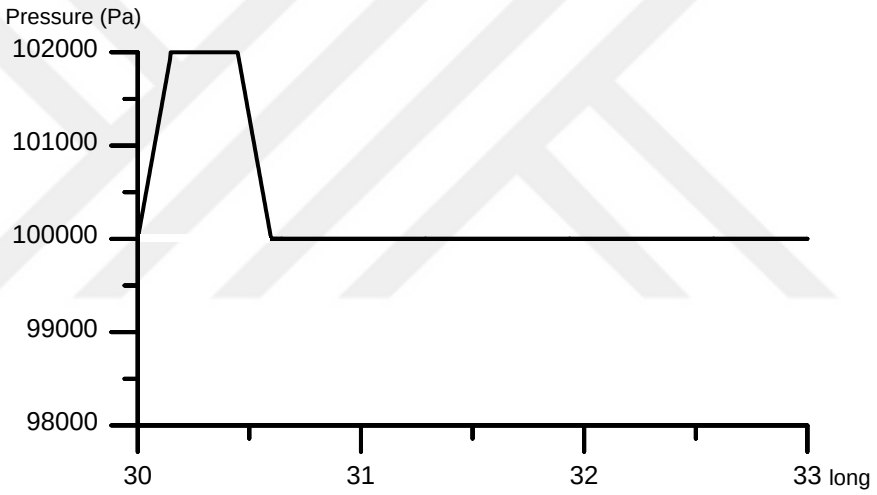

Figure 4.19. A-A and B-B Sectional View of the Pressure Band on the Stepwise Shelf Bathymetry with 1:100 Shelf Slope

Stepwise shelf bathymetry with 1/100 slope is modeled for three different cases. In this bathymetry, wave celerity shows the difference: at the 500 m depth flat section c has its maximum value, 70 m/sec; at the 50 m depth flat bottom section c has its minimum value which is 22 m/sec; and between these two flat bottom sections (1/100 bottom slope section) c changes from 70 m/sec to 22 m/sec depending on the depth. In the Case 1, V is 200 m/sec and it is bigger than the c values. In the Figure

4.20, top and sectional views of the water elevation and water velocity on the 1/100 bottom slope stepwise shelf bathymetry for Case 1 are illustrated.

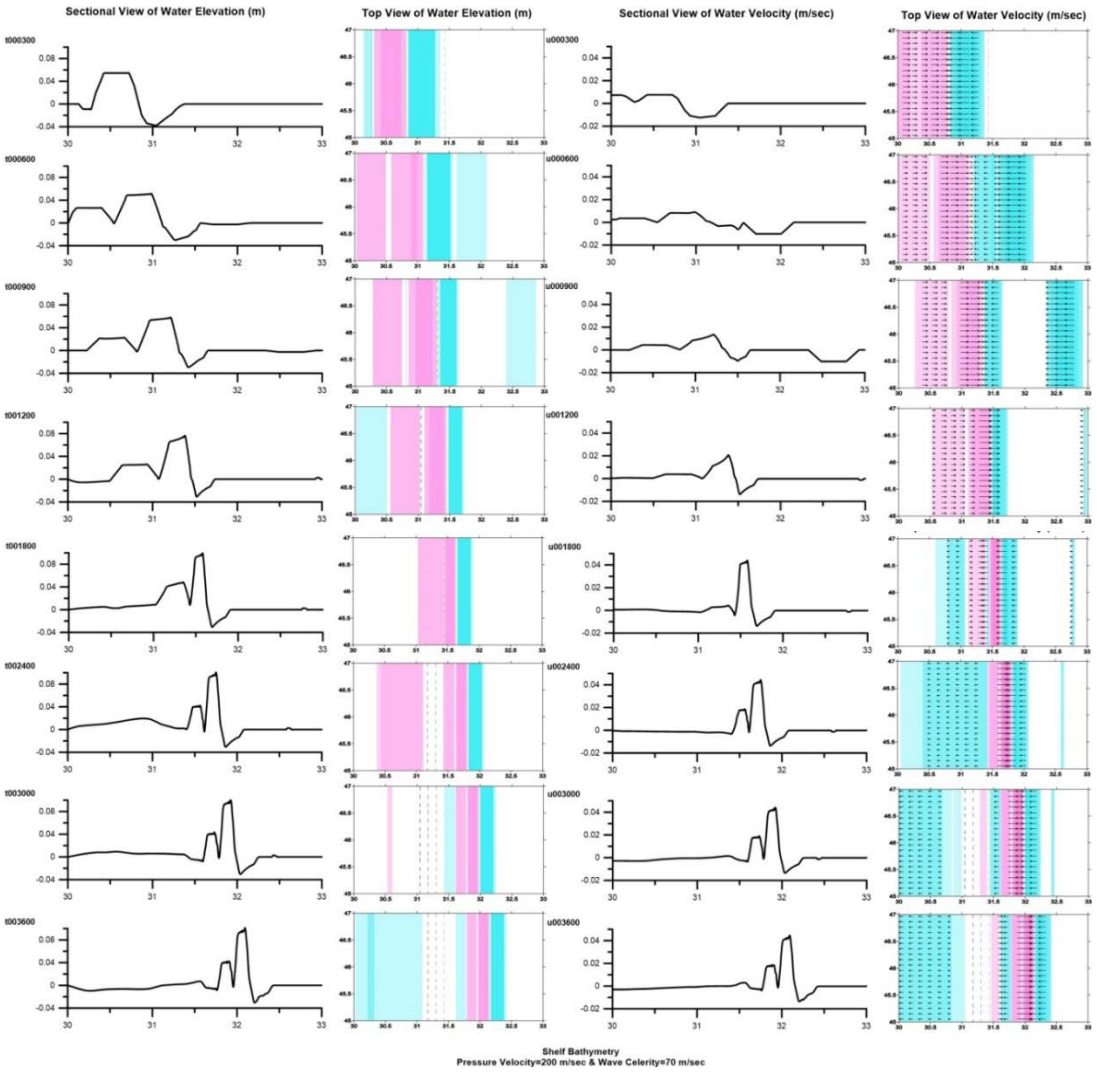

Figure 4.20. Top and Sectional Views of the Water Elevations and Water Velocities on the Stepwise Shelf Bathymetry with 1:100 Shelf Slope (Case 1, V=200 m/sec and c_{max}=70 m/sec)

When the results are investigated for Case 1, at the 5 minutes of the simulation, 5.5 cm initial maximum wave height is observed on the 500 m depth flat bottom section and it propagates towards shelf. At 10 minutes, another wave is formed behind the initial wave which has 2.6 cm wave height. After 5 minutes, initial maximum wave

height reaches up to shelf section of bathymetry and wave height is 5.82 cm. At 20 minutes, wave height becomes 7.66 cm. When wave come to shelf part of the bathymetry, it is observed that wave height and water velocity are slightly increased. Last 30 minutes of the 1 hour simulation, initial wave propagates by constant water surface elevation and velocity where maximum wave height is 10 cm by 4.4 cm/sec velocity on the 50 m depth flat bottom part. On the other hand, the wave lengths of the initial and sequent wave are getting smaller. It is due to the effect of the shelf part.

Secondly, in the Case 2, the pressure velocity and maximum wave celerity are taken as equal each other. The results for the effects of the stepwise shelf bathymetry on the water elevation and velocity for the Case 2 are shown in the Figure 4.21.

In the present case (Case 2), atmospheric pressure disturbance speed and speed of the free disturbance in the water are same. Therefore, Proudman resonance occurs and maximum water surface elevations are calculated. At the end of 5 minutes, the wave has 31.5 cm wave height and 3.05 cm/sec velocity. The swell and collapse in the water are symmetric and there are energy conservation. At 10 minutes, water surface elevation and velocity slightly increase and the values are 49.6 cm and 5.68 cm/sec. These values reach up 65.3 cm and 8.45 cm/sec, 5 minutes later. At 20 minutes, wave meet by sloping part of the bathymetry with 86.5 cm wave height with 15 cm/sec velocity. Then at 30 minutes, wave elevation increases more rapidly due to the shelf effect and it is 1.53 m by velocity of 0.56 m/sec. At the end of the simulation, maximum water elevation is 1.77 m. When the wave meets with sloping part, wave length is getting smaller while amplification is increasing.

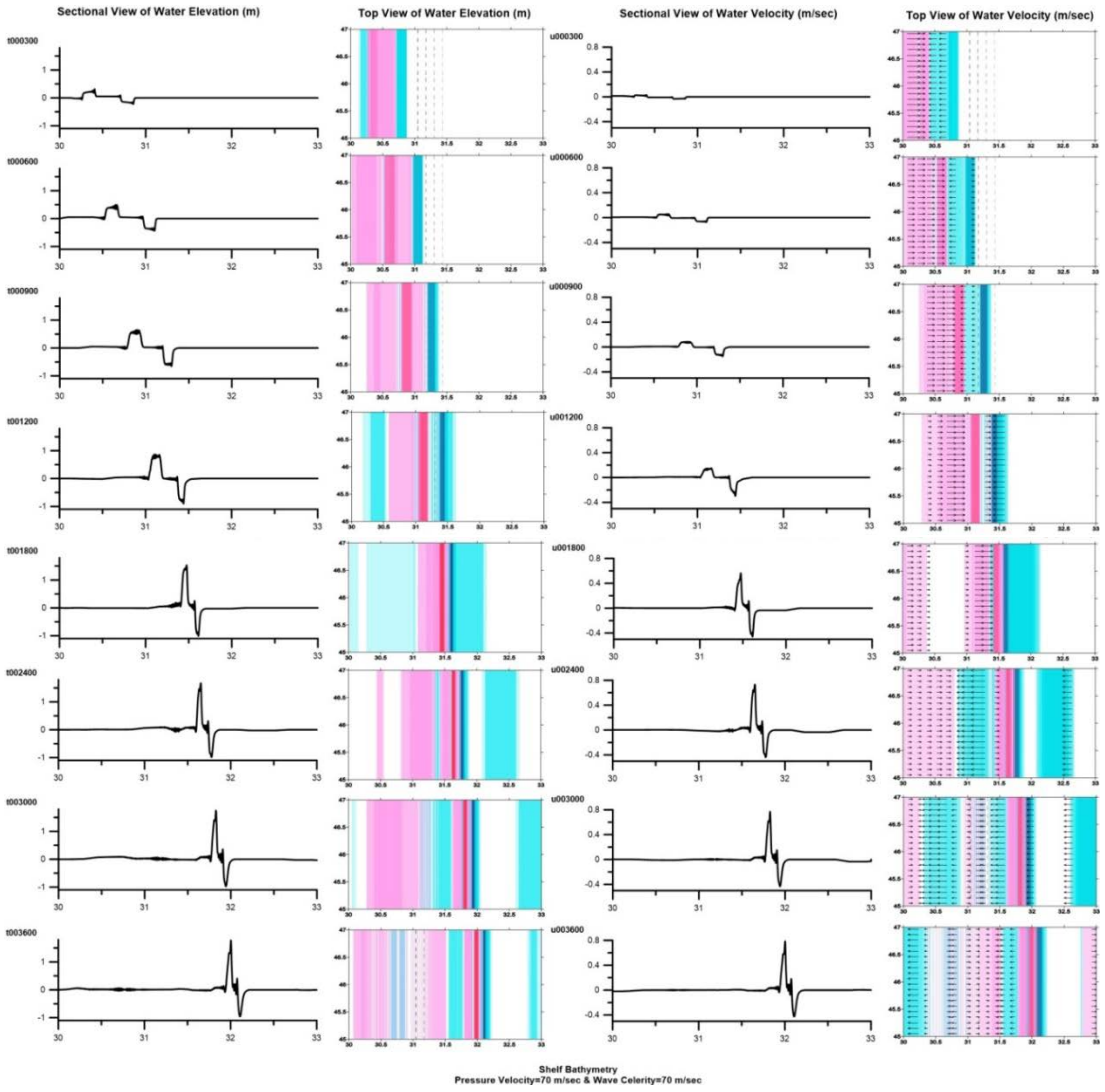

Figure 4.21. Top and Sectional Views of the Water Elevations and Water Velocities on the Stepwise Shelf Bathymetry with 1:100 Shelf Slope (Case 2, V=70 m/sec and c_{max}=70 m/sec)

In the Case 3, V is used as 40 m/sec, as not fast as the maximum wave celerity. The results are illustrated in the Figure 4.22.

The results of Case 3 are similar to Case 1 in terms of shape, but they are different from each other quantitatively. In the Case 3, due to the slower pressure velocity, wave amplitudes are observed higher than the Case 1. Specifically, at 5 minutes, the wave amplitude attains to 24.4 cm and it propagates by 2.2 cm/sec velocity.

Thereafter, 20 minutes later, water surface elevation is observed as 30 cm. Then at 40 minutes, wave height increases more rapidly due to the shelf effect and it is 55.8 cm by velocity of 16.5 cm/sec. At the end of the 60 minutes simulation, the maximum water surface elevation reaches up to 70 cm.

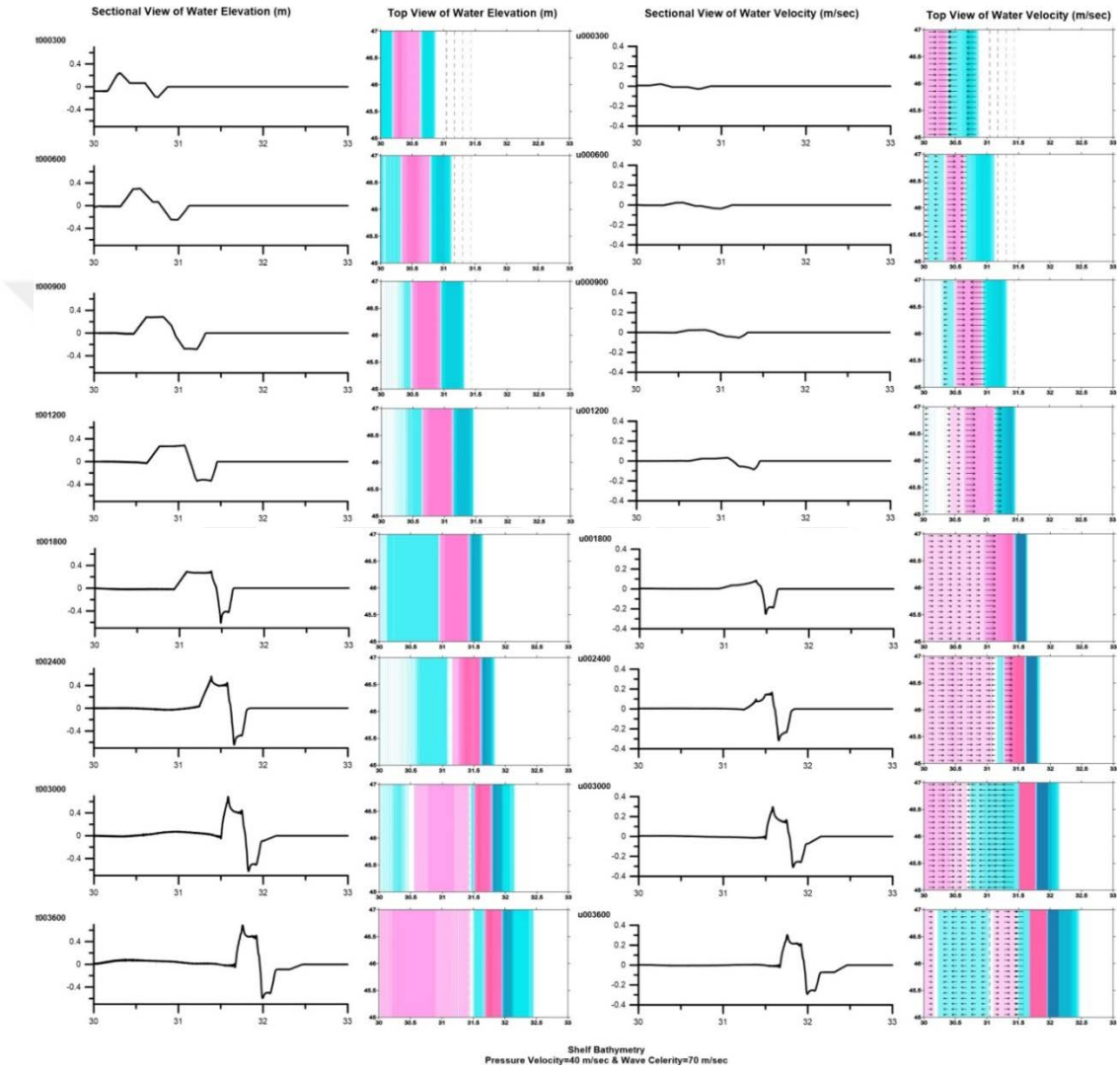

Figure 4.22. Top and Sectional Views of the Water Elevations and Water Velocities on the Stepwise Shelf Bathymetry with 1:100 Shelf Slope (Case 3, V=40 m/sec and c_{max}=70 m/sec)

In all of the three cases of the stepwise shelf bathymetry, water surface elevation increases towards to the end of the simulation. At the location where sloping part begins, the increase rises rapidly. Among these three cases, the highest water surface elevations are observed in the Case 2 because of the equality of the V and c_{max}. The minimum change in the water surface elevation is seen in the Case 1. In the Case 2, the water surface elevation is almost 18 times of the maximum water surface elevation in the Case 1 and it is nearly 2.5 times of the water surface elevations where the pressure moves slower than the maximum wave celerity.

4.2.3. Stepwise Shelf Bathymetry with 1:200 Shelf Slope

This stepwise shelf bathymetry has three different parts; 500 m depth flat bottom, 1/200 slope bottom 500 m depth to 50 m depth and flat bottom with 50 m depth. The basin is bounded from northern and southern boundaries. The top and sectional views of the stepwise shelf bathymetry with 1:200 shelf slope are shown in the Figure 4.23 and Figure 4.24.

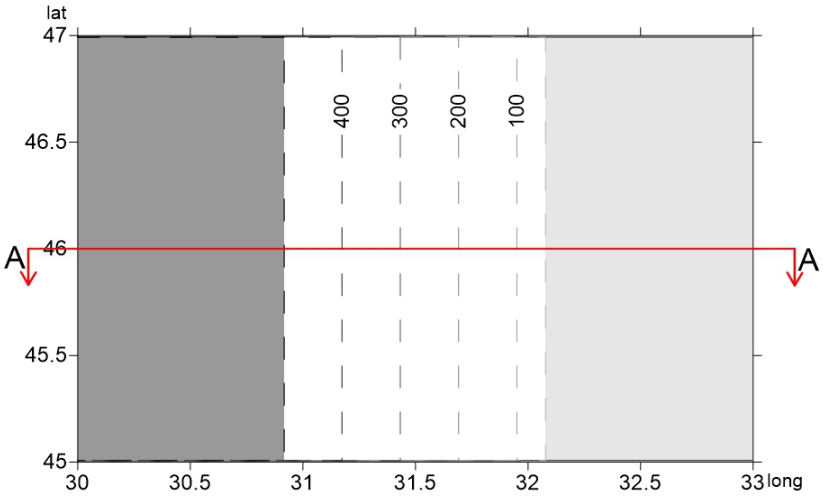

Figure 4.23. Top View of the Stepwise Shelf Bathymetry with 1:200 Shelf Slope

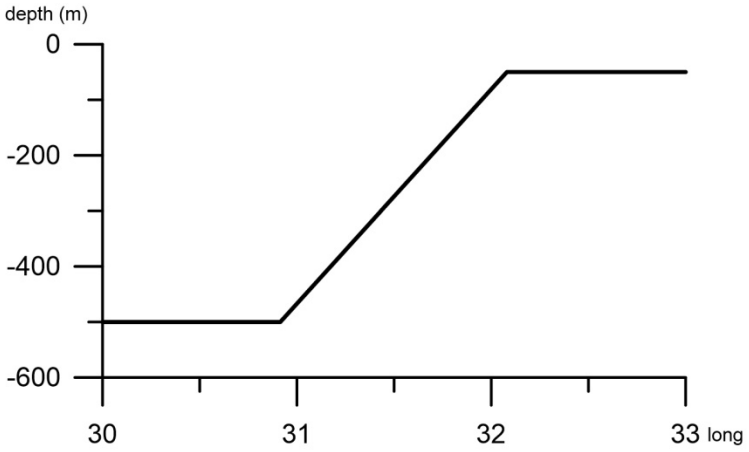

Figure 4.24. A-A Sectional View of the Stepwise Shelf Bathymetry with 1:200 Shelf Slope

The initial pressure band impulse which is given at the beginning of the simulation with a 102000 Pascal high pressure has 46.6 km width. Also, the pressure band propagates by specified constant velocities from left to right. Then, the top and sectional views of the pressure band on the stepwise shelf bathymetry with 1/200 shelf slope are shown in the Figure 4.25 and 4.26.

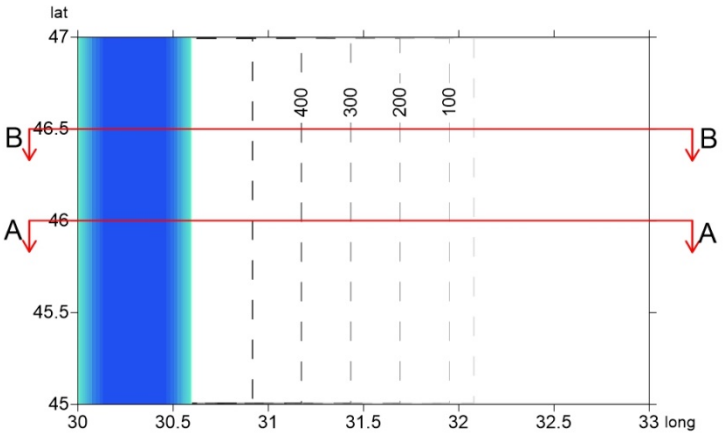

Figure 4.25. Top View of the Pressure Band on the Stepwise Shelf Bathymetry with 1:200 Shelf Slope

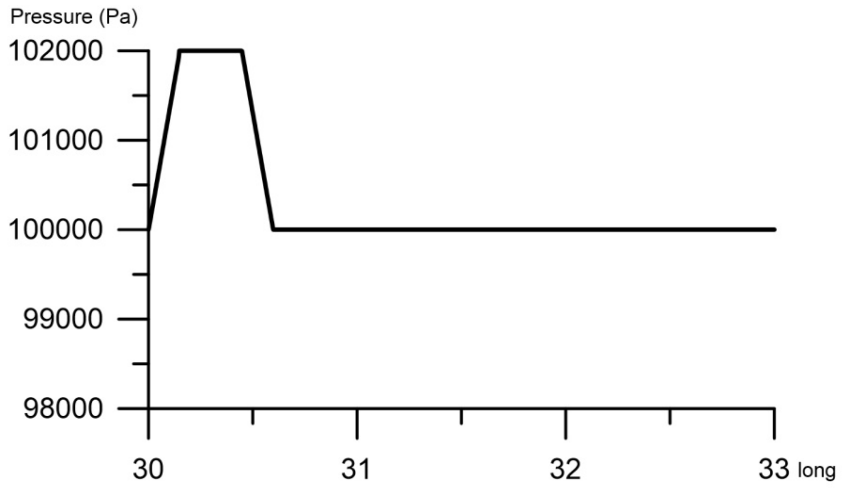

Figure 4.26. A-A and B-B Sectional View of the Pressure Band on the Stepwise Shelf Bathymetry with 1:200 Shelf Slope

Three different cases are conducted on the stepwise shelf bathymetry with 1:200 shelf slope (for the pressure velocities are 200 m/sec, 70 m/sec and 40 m/sec). Sea level fluctuations and water velocities are computed at different time steps (300, 600, 900, 1200, 1800, 2400, 3000 and 3600 seconds). In the bathymetry, wave celerity shows the variety regarding to the water depth. The maximum wave celerity (c) is 70 m/sec and wave celerity varies between 70 m/sec and 22 m/sec. In the first simulation (Case 1), pressure velocity which is 200 m/sec is greater than the wave celerity. The top and sectional views of the water surface elevations and wave velocities are given in the Figure 4.27.

According to the results of the Case 1, initial wave at 5 minutes due to the atmospheric pressure forcing is 5.5 cm which moves on 500 m flat bottom part of the shelf bathymetry. After 5 minutes, another wave is formed behind this wave which has almost half of the amplitude of initial wave. At 15 minutes of the simulation, initial wave approaches to beginning of the sloping part of the bathymetry and it has wave height of 5.6 cm. Then, at 20 minutes, maximum wave amplitude is calculated as 6 cm. While the wave propagates towards the eastern part of the bathymetry, wave height is slightly amplified by increasing water velocity. At the end of the simulation (at 60 minutes), maximum wave height is observed which is 10 cm. In this case, due

to faster V, wave height increases on a small scale. Therefore, shelf effect cannot be observed clearly.

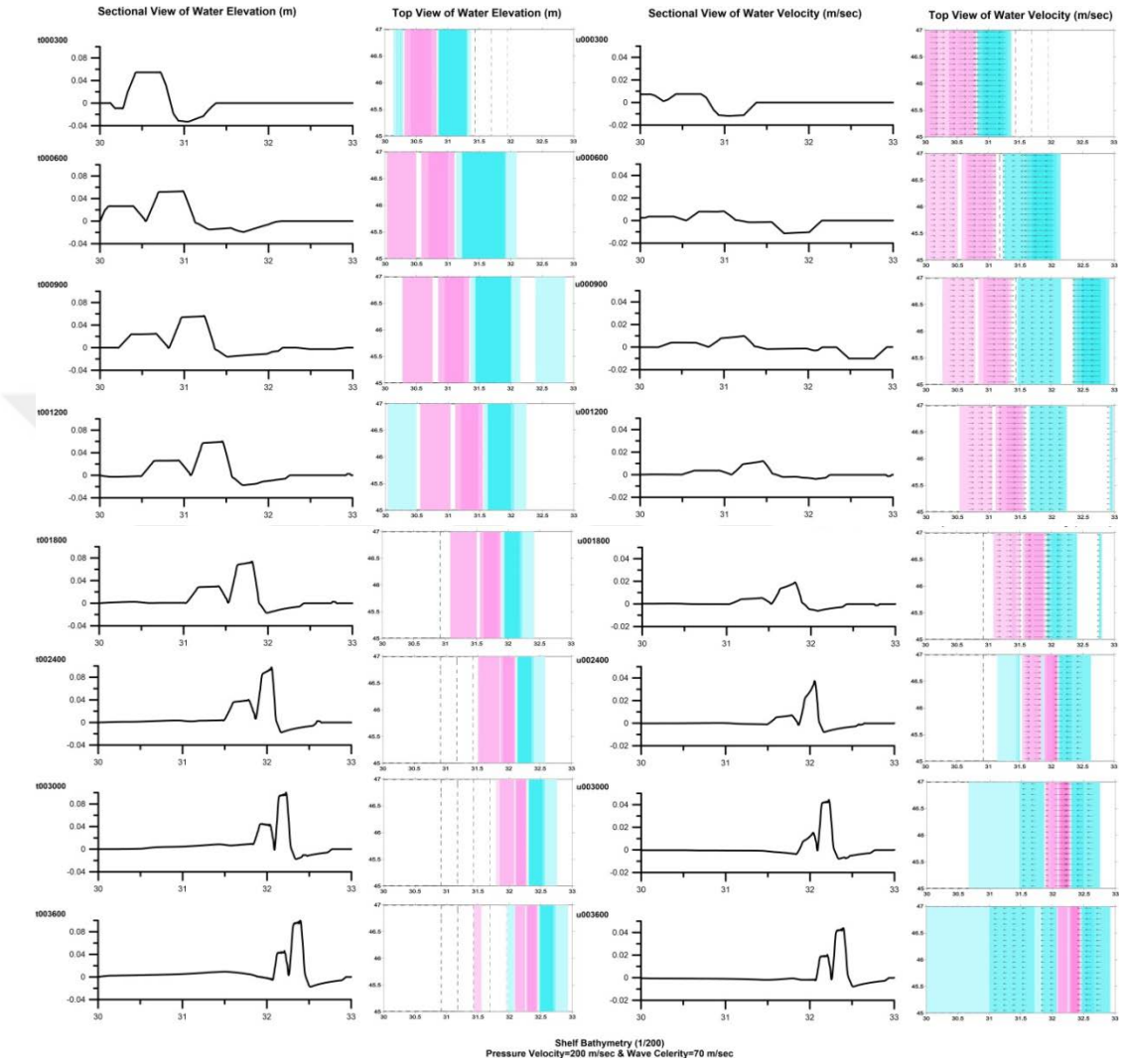

Figure 4.27. Top and Sectional Views of the Water Elevations and Water Velocities on the Stepwise Shelf Bathymetry with 1:200 Shelf Slope (Case 1, V=200 m/sec and c_{max}=70 m/sec)

As a second simulation (Case 2), same magnitudes of pressure velocity and wave celerity are given to the numerical model. Then the results are presented in the Figure 4.28.

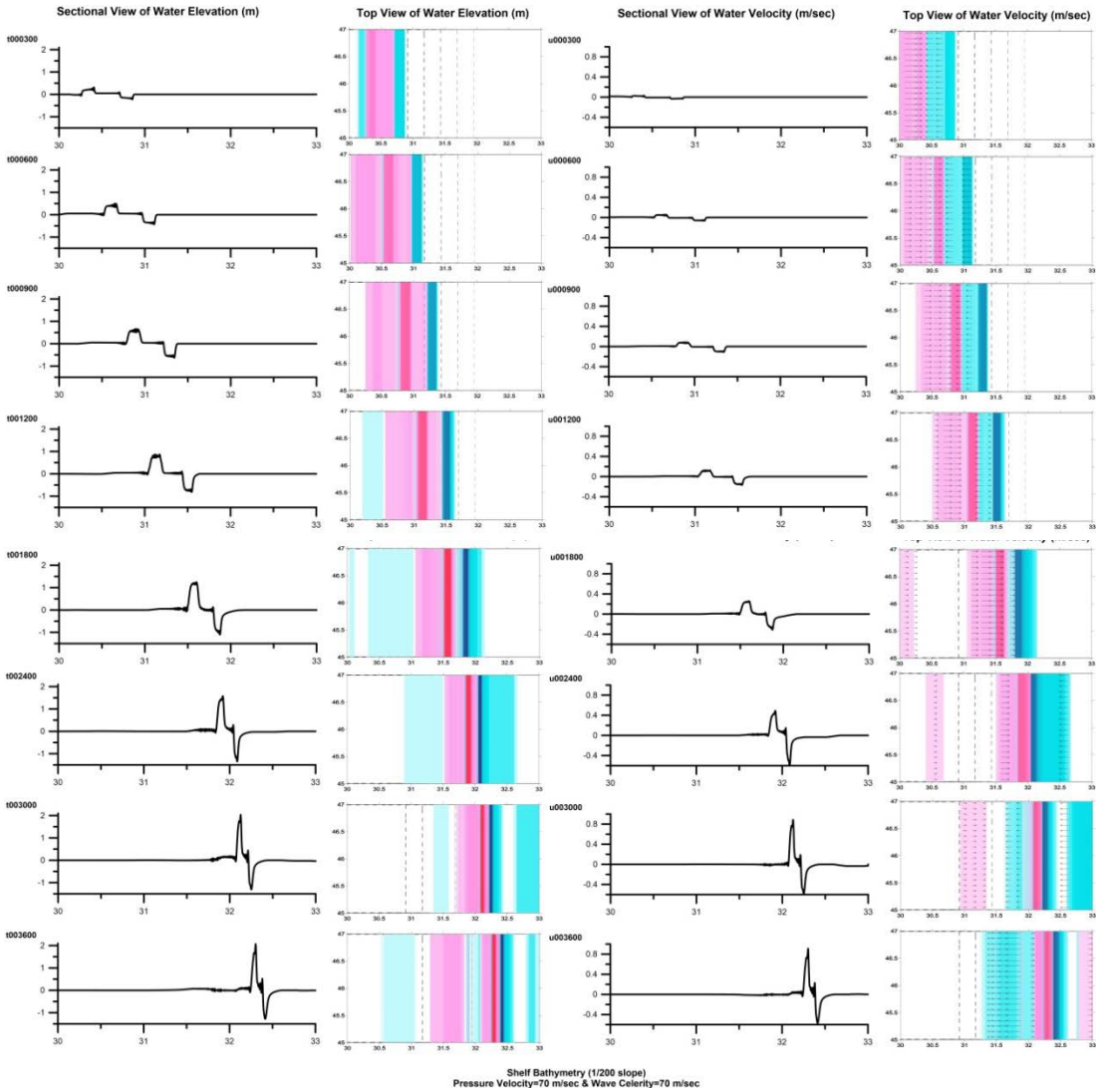

Figure 4.28. Top and Sectional Views of the Water Elevations and Water Velocities on the Stepwise Shelf Bathymetry with 1:200 Shelf Slope (Case 2, V=70 m/sec and c_{max}=70 m/sec)

In the Case 2, due to resonance occurrence, the highest wave amplitudes are observed. The initial wave at 5 minutes generated by the atmospheric pressure is 31.5 cm. At 10 minutes, maximum wave height of 50 cm propagates by 6 cm/sec velocity towards right. At 15 minutes, wave height reaches approximately 65 cm and at 20 minutes, it is roughly calculated as 86 cm. After 20 minutes of simulation, wave becomes to move on the sloping part of the bathymetry. Then at 30 minutes, wave

height is 1.25 m by 26 cm/sec velocity. At 60 minutes, the maximum wave height of 2.1 m is observed on the 50 m depth flat bottom part of the bathymetry.

The results of the final simulation (Case 3) where V is 40 m/sec on the stepwise bathymetry with 1:200 shelf slope are illustrated in the Figure 4.29.

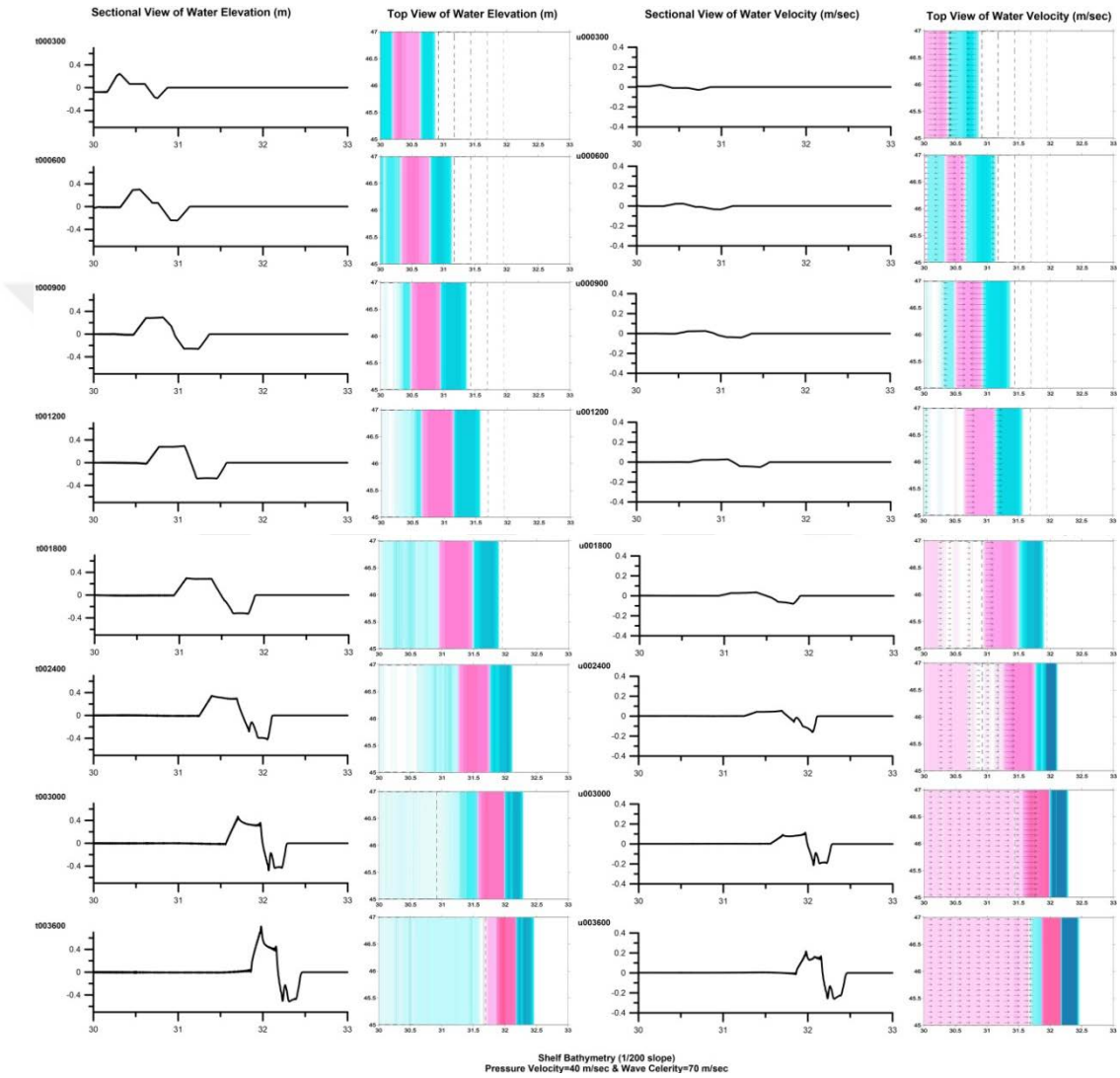

Figure 4.29. Top and Sectional Views of the Water Elevations and Water Velocities on the Stepwise Shelf Bathymetry with 1:200 Shelf Slope (Case 3, V=40 m/sec and c_{max}=70 m/sec)

In general, in the Case 3, water surface elevations are observed greater than elevations in the Case 1. At 5 minutes, initial wave generated due to the high atmospheric pressure forcing is 24 cm. At 10 minutes, maximum water surface elevation is calculated as 30 cm and at 15 minutes, 20 minutes and 30 minutes of the simulation it remains same. At 40 minutes, wave height is 34 cm by 5.5 cm/sec velocity. Thereafter, wave height reaches 47 cm at 50 minutes due to shelf effect. At the end of the simulation, at 60 minutes, water surface elevation has its maximum value which is 80 cm.

Briefly, with stepwise shelf bathymetry simulations, effects of different bottom slope effects are investigated. For the all cases (V is greater, equal and smaller than c), the first 20 minutes of the simulation of 1/100 and 1/200 shelf slope bathymetries, there are not an important difference in the results of water surface elevations. For the Case 1, the effects of the 1/100 and 1/200 shelf slopes are almost same. It means that due to fast high atmospheric pressure movement, small wave heights observed. Therefore, the effects of shelf slope on the water elevations are insignificant. In the Case 2, at 30 minutes, wave height observed on 1/100 shelf slope is greater than the wave height on 1/200 shelf slope bathymetry. Conversely, at 60 minutes, while the wave height reaches 2.1 m on the 1/200 bottom slope, it remains 1.7 m on the 1/100 bottom slope stepwise shelf bathymetry. Similarly, in the Case 3, while at 40 minutes, wave height is bigger on the 1/100 shelf slope bathymetry, it becomes higher on the 1/200 shelf slope at 60 minutes. On the other hand, when 1/10 steepest slope is compared with the other shelf slope bathymetries, for the all cases the smallest maximum wave heights are calculated in the 1/10 shelf slope bathymetry simulations. Therefore, the general outcome obtained in a series of simulations regarding to different shelf slopes is the milder slopes can cause higher wave amplifications.

4.3. Simulations of Pressure Movement Perpendicular to Shoreline

The generation and behavior of the waves generated by the pressure movement (i) towards the shore on upward sloping bathymetry and (ii) towards the sea on downward sloping bathymetry are also investigated by simulations. The problems of pressure movement perpendicular to the shoreline can be combined in typical bathymetrical conditions and can be simulated in a single run. In the following, two cases are described and the results of simulations are presented.

The upward sloping bathymetry and downward sloping bathymetry are simulated as a single bathymetry where the latitudinal land is located in the middle of these two bathymetries with 12 km width. From the land to both east and west directions, water depth increases by 1/200 slope to 500 m water depth. The bathymetry is symmetrical in both two directions and the top and sectional views of the bathymetry are shown in Figures 4.30 and 4.31. While the pressure moves from left to right, then the left half of the bathymetry in the Figure 4.30 represents the pressure movement to the shore on upward sloping bathymetry. Similarly, the left half of the bathymetry in the figure represents the pressure movement to the sea on downward sloping bathymetry.

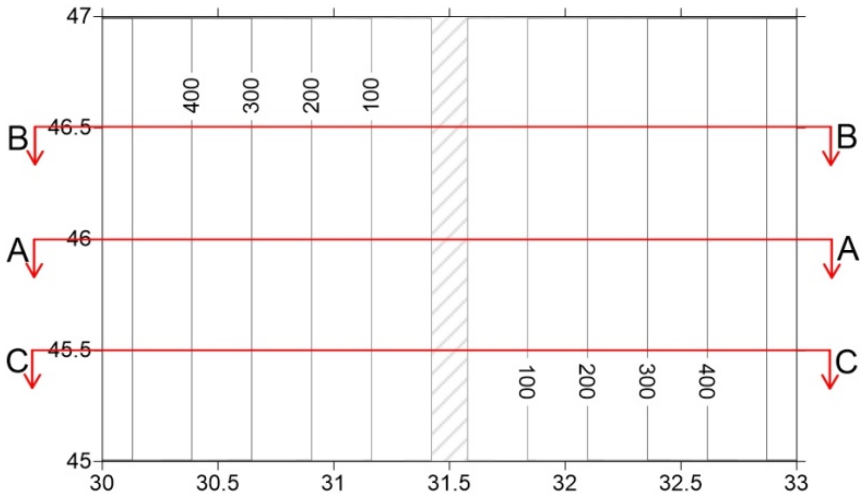

Figure 4.30. Top View of the Upward and Downward Sloping Bathymetry

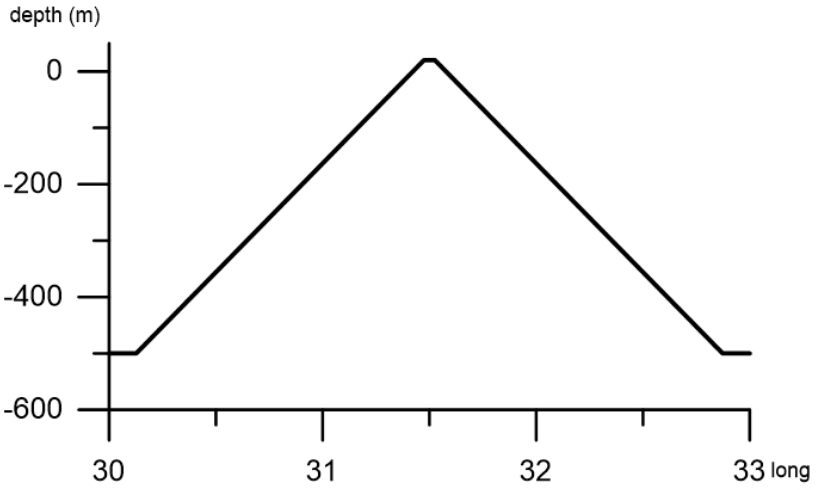

Figure 4.31. Sectional View of the Upward and Downward Sloping Bathymetry

In the simulations, 46.2 km width 102000 Pascal high pressure band was given as an initial pressure. Then, it moves from west to east by the specified velocity. The top and sectional views of pressure band are shown in the Figure 4.32 and 4.33.

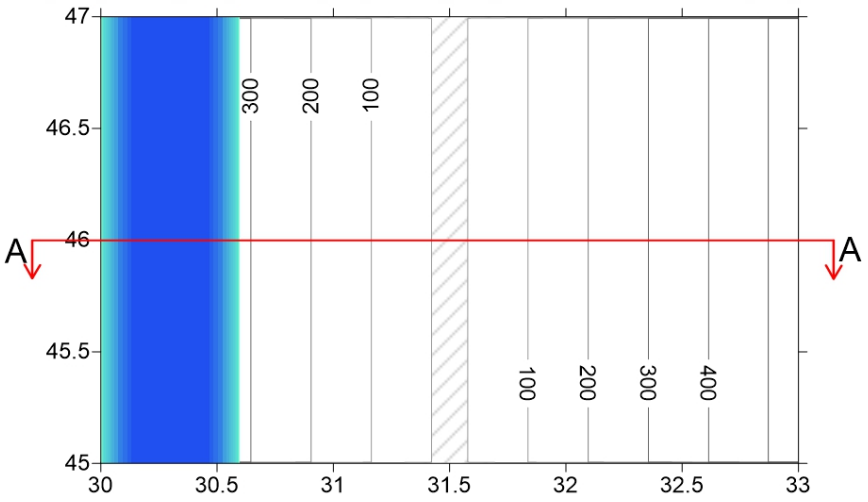

Figure 4.32. Top View of the Pressure Band on the Upward and Downward Sloping Bathymetry

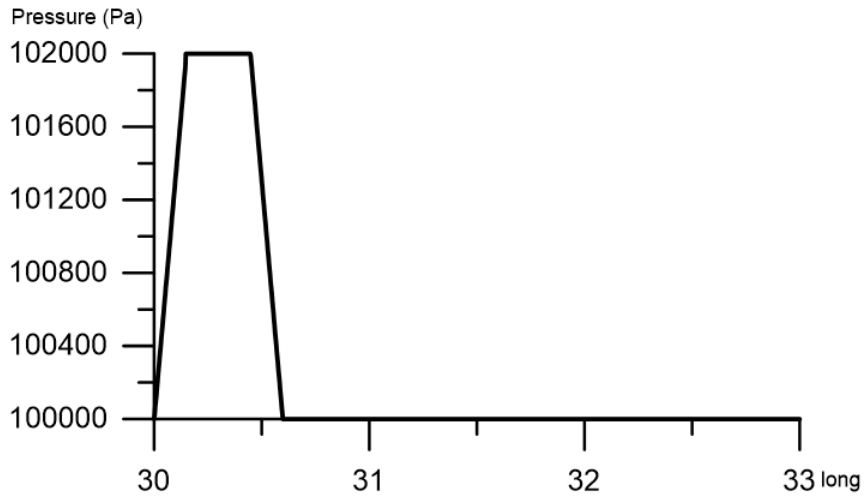

Figure 4.33. A-A Sectional View of the Pressure Band on the Upward and Downward Sloping Bathymetry

The upward and downward sloping bathymetry are studied for three different conditions which are determined according to pressure velocity. In all cases, maximum wave celerity equals to 70 m/sec and it decreases while wave is propagating to the shore. Similarly, while wave is propagating from shore to sea, the wave celerity reaches its maximum value by proportionally increase. In the case 1, pressure velocity is selected as 200 m/sec and it propagates towards to left, then the results of the water surface elevations and water velocity is obtained after 60 minutes simulation and they are given in the Figure 4.34.

At the beginning of the simulation, the generated wave is too weak and it has 5.5 cm wave height at 5 minutes. Until 40 minutes of the simulation, the increase in the water surface elevation is too small. At 40 minutes of the simulation, amplification is observed at the left half of the bathymetry where wave height shows rapid increase to 21 cm due to the arrival of the wave to the shore. Then, wave reflects from the land and shows the decrease in the opposite direction of the pressure propagation. Also, at the right side of the land, there is any significant change observed; meanwhile, the maximum elevation is observed at the left of the land. On the other hand, the water velocities during the simulation are very small except the water velocity at the 40 minutes of the simulation. At that time, velocity increases, because the water depth is

getting smaller and wave meet the land. In addition, the pressure band reaches to the right half of the bathymetry after 10 minutes of the beginning of the simulation where small fluctuations (small amount of collapse) are observed.

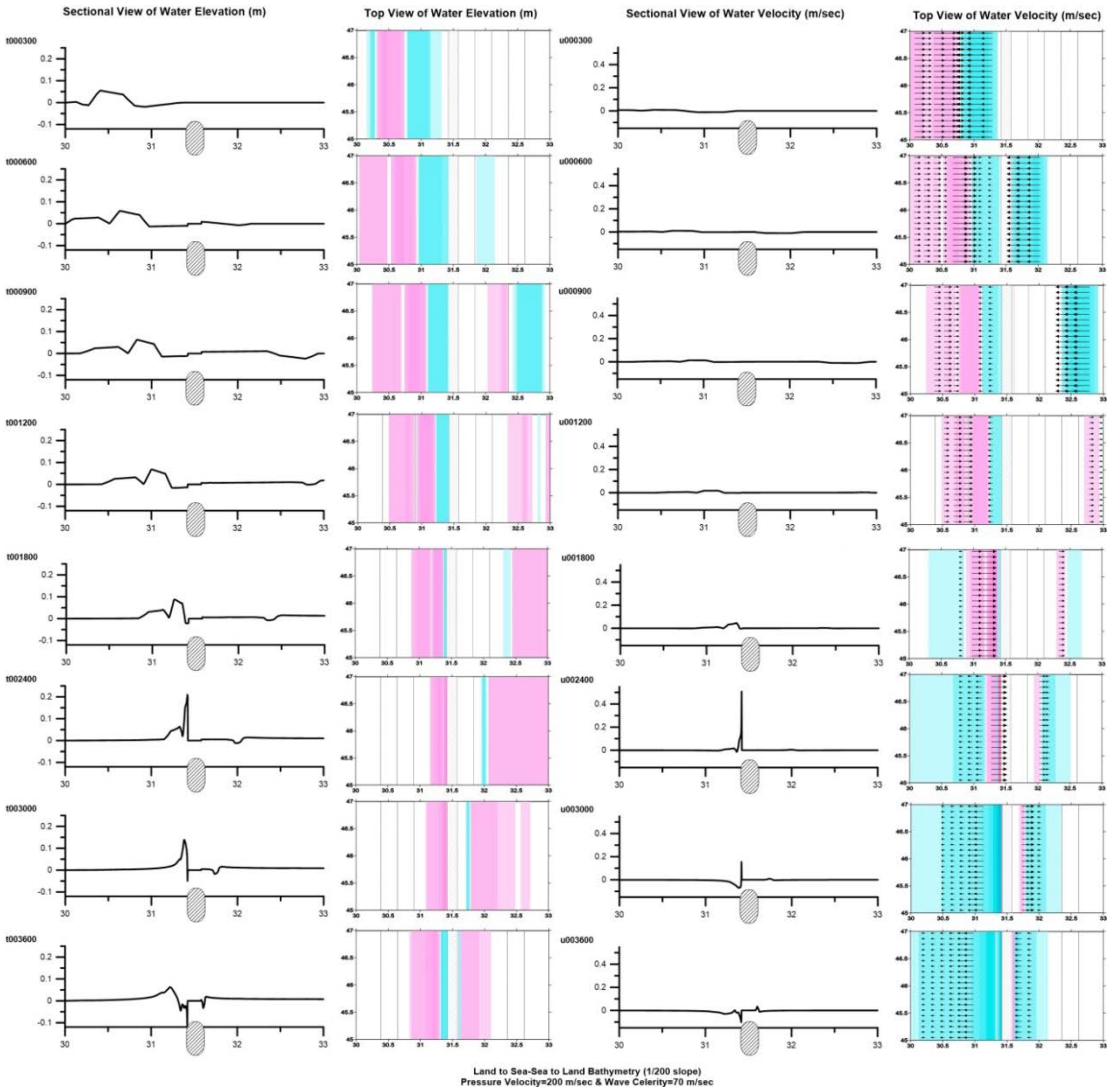

Figure 4.34. Top and Sectional View of the Water Elevation and Water Velocity on the Upward and Downward Sloping Bathymetry (Case 1, V=200 m/sec and c_{max}=70 m/sec)

In the Case 2, the pressure band moves by 70 m/sec constant velocity. The resonance between the pressure velocity and wave celerity occurs where V and c_{max} are the same. The simulation results for the Case 2 are given in the Figure 4.35.

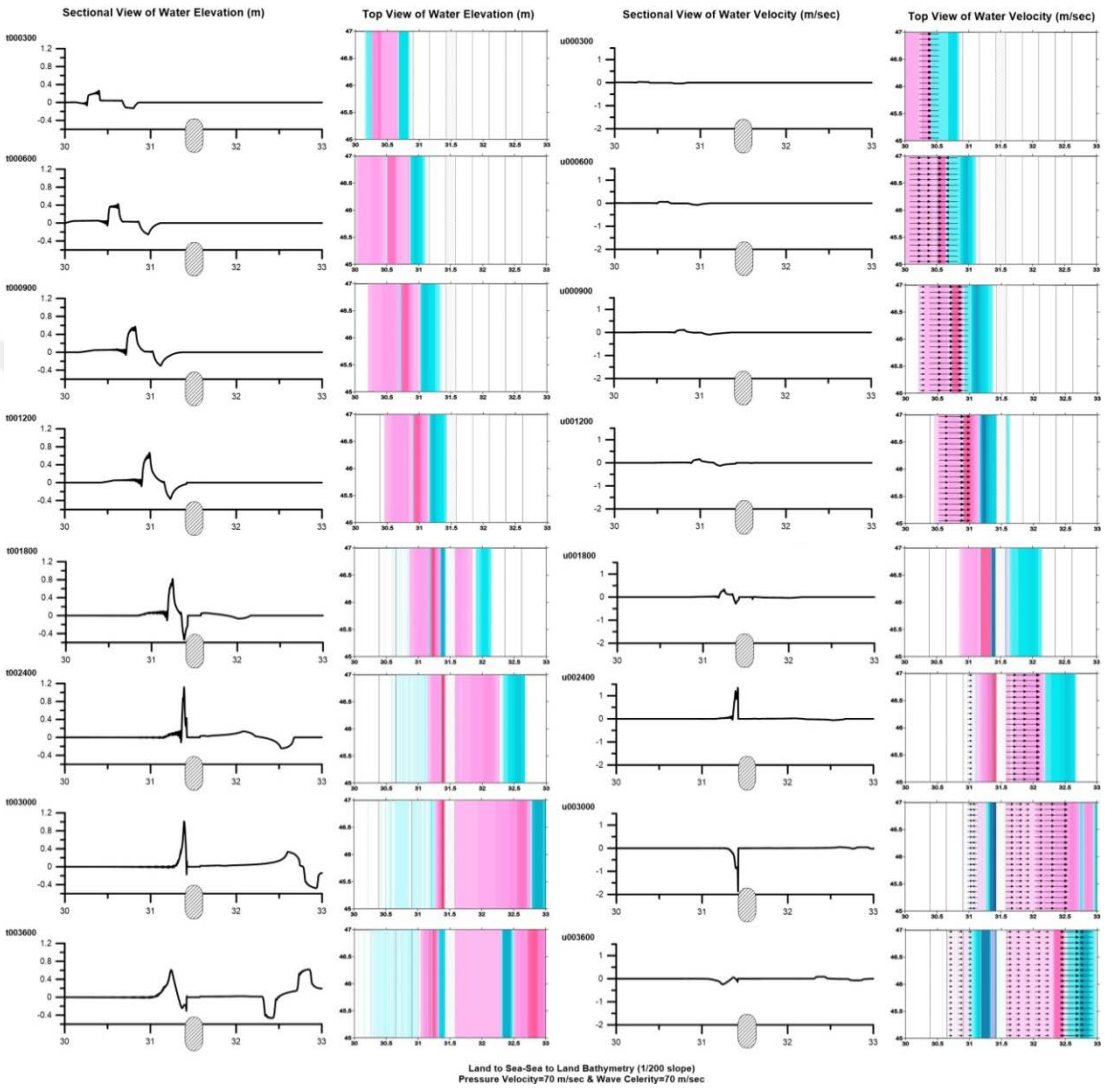

Figure 4.35. Top and Sectional View of the Water Elevation and Water Velocity on the Upward and Downward Sloping Bathymetry (Case 2, V=70 m/sec and c_{max}=70 m/sec)

The first observed maximum water elevation is 26.5 cm. The water surface elevations continue to increase until the wave encounters the shore. The maximum

wave height is observed as 1.12 m at 40 minutes. Afterward, the wave reflects from the land to the reverse direction. When waves encounter the shore, water velocity has its maximum value is 1.35 m. On the other hand, pressure band pass the land at 30 minutes. Therefore, the depression in the water surface elevation is observed in the downward sloping bathymetry. After 50 minutes, hilliness in the water surface is observed at the right half of the bathymetry because of that the collapse in the water reflected from the eastern boundary.

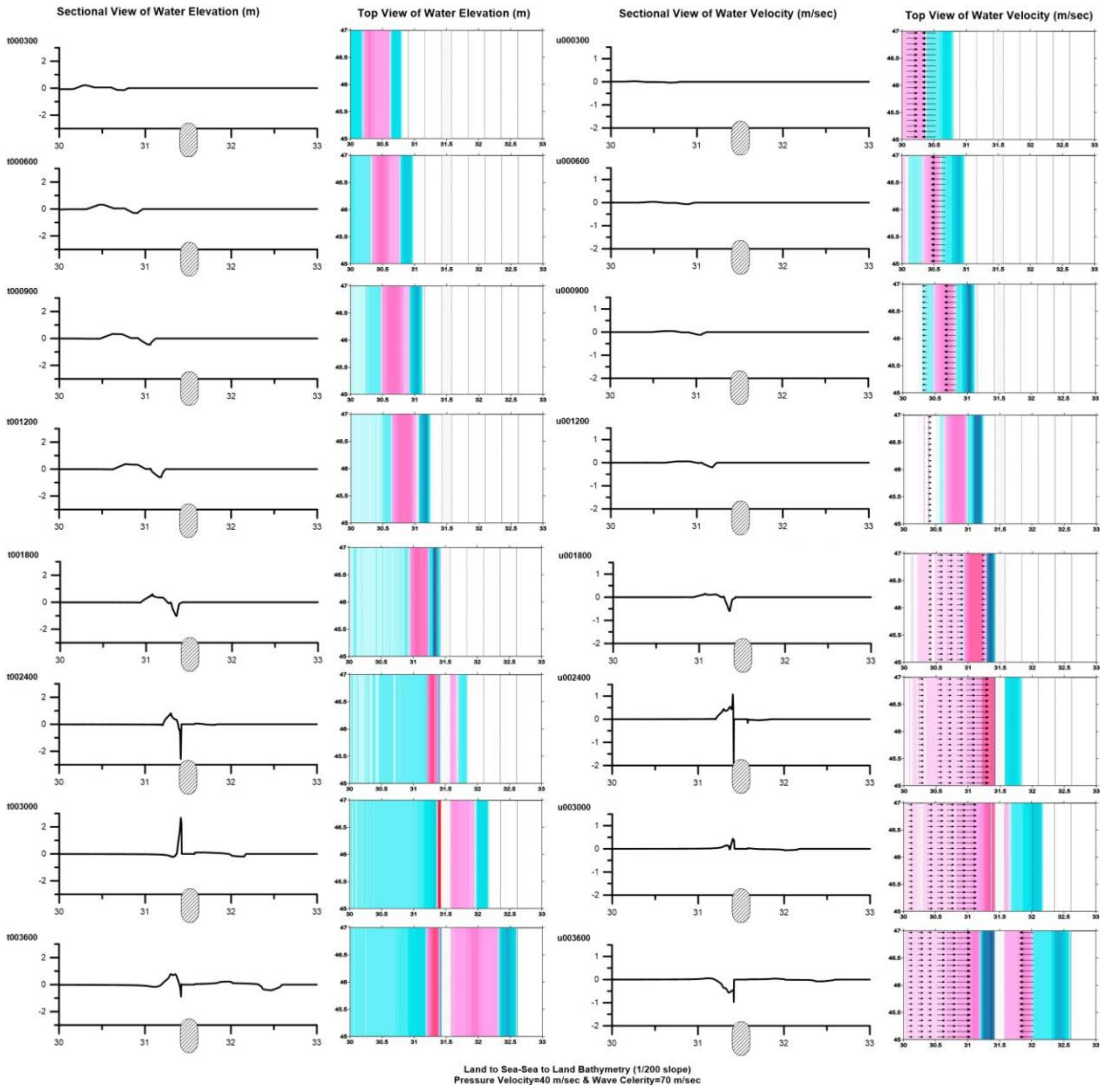

Figure 4.36. Top and Sectional View of the Water Elevation and Water Velocity on the Upward and Downward Sloping Bathymetry (Case 3, V=40 m/sec and c_{max}=70 m/sec)

In the Case 3, the pressure band velocity is slower than maximum wave celerity which is 40 m/sec. Then, the results are shown in the Figure 4.36.

In this case, the initial water surface elevation is 22.7 cm at 5 minutes. Then, at 40 minutes, the wave hit the shore by 1.07 m/sec velocity and 81.8 cm wave height. The wave reflects from the land 10 minutes later. Due to this reflection, wave goes back and reaches the 2.68 m wave height. However, the velocity of the wave decreased after the reflection. Furthermore, pressure band cross over the land in 50 minutes. Hence, slight collapse in the water surface is observed at 50 minutes.

When the all of these cases are considered, the followings can be concluded. First of all, for the upward sloping bathymetry, the first point where the wave observed is more far away from the shore in the Case 3. Then, this point is getting closer to the land in the Case 2 and Case 1. The closer point is observed in Case 1. Secondly, the maximum wave amplitude is 1.12 m which is seen in Case 2 while wave is propagating over upward sloping bathymetry. However, due to the reflection from the shore, 2.68 m wave height is observed in the Case 3 which propagates by slower velocity in the opposite direction. Finally, collapse in the water surface is seen at 10 minutes, 30 minutes and 50 minutes in Case 1, Case2 and Case 3, respectively. In general, while wave propagates towards shore on upward sloping bathymetry, there is amplification in the water surface. Conversely, during the propagation towards the seaside, the wave cannot amplify.

As a general conclusion of this chapter, maximum water elevations of test results for all bathymetric shapes are given in the following table (Table 4.1).

Table 4.1. Maximum water elevations for all bathymetric shapes and cases

Bathymetries	CASE 1	CASE 2	CASE 3
Flat Bottom	6 cm	80 cm	30 cm
Triangular	5.2 cm	100 cm	80 cm
1/10 shelf slope	8.9 cm	122 cm	48.4 cm
1/100 shelf slope	10 cm	177 cm	70 cm
1/200 shelf slope	10 cm	210 cm	80 cm
U-D Sloping	21 cm	112 cm	268 cm

CHAPTER 5

CONCLUSIONS

Abnormal tsunami-like long waves are regularly observed at certain locations all over the world by causing economical loss, injury and death. They can show similarities with ordinary tsunamis in terms of physical characteristics (e.g. wave period, height) and destroying results. However, the generation mechanisms are different from each other. At the first stage of this study, the recent observations of these types of water surface fluctuations and wave amplifications are reviewed. It is seen that the main reasons of these events are related to meteorological parameters and local morphological conditions.

In order to investigate the effects of atmospheric pressure movement on the possible sea water level anomalies and coastal amplifications (in a seismically calm region without storm), different tests are conducted and results are presented, compared and discussed. Because of that the most probable cause of sea level differences is the atmospheric pressure disturbances; high atmospheric pressure movement is used as an input in the tests. Also, in the tests, it is assumed that air pressure moves as a band with a specified constant velocity from west to east on a different shape of bathymetries. Also, bathymetric shapes have important role on the wave amplification aside from coincidence of air pressure propagation velocity (V) and wave celerity (c). The abrupt changes in the depth near the shore can cause amplification.

In general, when the atmospheric pressure forcing is known, meteotsunamis can be easily modeled by two-dimensional wave equations. In the test studies, numerical model NAMI DANCE-P which solves the sets of 2D non-linear shallow water equations with atmospheric pressure terms in Cartesian coordinates is used to compute water surface elevations, directions and magnitudes of water velocities and momentum fluxes. The tsunami simulation and visualization code NAMI DANCE-P is recently developed as a new version of NAMI DANCE. To verify the new model, the numerical tests are conducted using regular shaped (500m deep, flat bottom) bathymetry and different speed of high pressure movement. The results are compared with the respective analytic solutions of sets of Euler equations for ideal fluid on the non-rotated Earth including atmospheric pressure term. The results of numerical and analytic calculations are found in fairly well agreement which points out that numerical model gives acceptable results.

After verification, numerous simulations are performed on five different bathymetric shapes: (i) triangular bathymetry, (ii) shelf bathymetry with 1:10 bottom slopes, (iii) shelf bathymetry with 1:100 bottom slopes, (iv) shelf bathymetry with 1:200 bottom slopes, (v) upward sloping and (vi) downward sloping bathymetry. For each bathymetry, three different air pressure velocities (200 m/sec, 70 m/sec and 40 m/sec) are determined and given as an input to the simulations. Regarding to outcomes obtained from numerical model, the maximum wave heights are seen in the regions where the ratio of pressure velocity to surface wave speed (V/c) equals to 1. These equality means that the wave number and period of the pressure force equals to wave number and period of the surface wave in the ocean (so-called Proudman resonance condition, Proudman, 1929). On the other hand, according to the numerical results, how the basin shapes affect the wave amplification is also discussed.

The main concluding remarks obtained from this study are given in the following.

- One of the governing parameters which causes the sea level fluctuations is the relation between the pressure speed and wave speed. When the pressure velocity is bigger than wave celerity, wave evolves and propagates with certain amplitudes. However, in this case due to that pressure leaves the bathymetry very quickly, water level oscillations cannot grow to the significant levels. On the other hand, when the pressure velocity is slower than the surface wave celerity, wave evolves to certain amplitude (higher amplitudes than the former case) and propagates faster than the forcing parameter (pressure). Besides, when the air pressure speed and surface wave speed are the same, wave develops and propagates with the highest amplitude.

- Another important factor which leads to wave amplification is the bathymetric conditions and morphology. Firstly, in the case of the triangular bathymetry maximum wave height is obtained as 93.8 cm (approximately 1 meter) in the case of equality of V and c_{max}. Also, wave moves faster in the deeper part of the bathymetry (middle of the bathymetry) and movement is getting slower towards to northern and southern slopes (to the borders) of the bathymetry. Secondly, on the stepwise shelf bathymetry, the maximum wave height is observed as 1.53 m when the wave meets by the shelf.

- Finally, on the upward and downward sloping bathymetry, two main different behaviors are seen. One of them observed when pressure propagates towards to the shore in where wave amplifies near the land. The other behavior is seen while air pressure is moving in the direction of the shore to the deep sea where water surface elevations have insignificant levels. Towards deep water, wave cannot amplify. Therefore, these results are important to understand the effect of the bathymetric shape. In the tests, the maximum wave height is 2.68 m which is computed when pressure moves towards shore on upward

sloping bathymetry. The additional amplification is also observed because of the superposition of incoming and reflected waves near the shore.

- Another outcome is the effect of the shelf slope. The bottom slope has also an important effect on the wave amplification. When the wave reaches to sloping bottom and propagates on the shelf, wave height and water velocity increase. According to test results, for the same atmospheric pressure velocities, the amplification over the stepwise shelf bathymetry with 1/200 shelf slope is greater than the stepwise shelf bathymetry with 1/100 bottom slope and 1/10 bottom slope bathymetries. Therefore, amplification is higher on milder slopes of the shelves.

- The new version of tsunami simulation and visualization code NAMI DANCE-P is capable of to be applied to generation and propagation of long wave due to the atmospheric disturbances.

Future Recommendations:

The test studies are performed on the regular shaped bathymetries to clarify the fundamental concepts related to the meteotsunamis. After that, irregular shape bathymetries can be modeled as a further step to understand the real meteotsunami events more precisely. In addition, effects of different pressure impulses and velocities can also be investigated and simulated by the irregular shaped bathymetries.

In nature, atmospheric pressure occurs everywhere every time on the Earth, therefore the regular high pressure band is used for just estimation of the general concept of the meteorological origin events. To obtain more realistic results, non-uniform pressure distributions and their propagation should be used over the regular or irregular shaped bathymetries. Also, long, narrow and shallow bays can be investigated specifically.

While approaching to reality, NAMI DANCE-P needs to complex improvements. One of them is the dispersion relation. Originally, numerical model generates non-dispersive solutions; however more realistic approach can also be developed when dispersion term is used in the numerical solution. It is related to that wave has variable frequencies while it is propagating. In this case, different parameters should be used by calculating *c* such as wave number and wave amplitude in addition to water depth. Furthermore, one of the recently observed case studies can be modeled by using the new-developed numerical model.

REFERENCES

Airy, G. B. (1878). On the tides at Malta. *Philosophical Transactions of the Royal Society of London, 169*, 123-138.

Antonopoulos, J. (1992). The tsunami of 426 BC in the Maliakos gulf, eastern Greece. *Natural hazards*, *5*(1), 83-93.

Bailey, K., DiVeglio, C., & Welty, A. (2014) An Examination of the June 2013 East Coast Meteotsunami Captured By NOAA Observing Systems (NOAA Technical Report NOS CO-OPS 079). *NOAA.Gov*. National Oceanic and Atmospheric Administration

Bechle, A. J., & Wu, C. H. (2014). The Lake Michigan meteotsunamis of 1954 revisited. *Natural hazards*, *74*(1), 155-177.

Broeze, J., & Van Daalen, E. F. (1992). Radiation boundary conditions for the two-dimensional wave equation from a variational principle. *Mathematics of Computation*, *58*(197), 73-82.

Candella, R. N. (2009). Meteorologically induced strong seiches observed at Arraial do Cabo, RJ, Brazil. *Physics and Chemistry of the Earth, Parts A/B/C*, *34*(17), 989-997.

Cho, K. H., Choi, J. Y., Park, K. S., Hyun, S. K., Oh, Y., & Park, J. Y. (2013). A synoptic study on tsunami-like sea level oscillations along the west coast of Korea using an unstructured-grid ocean model. *Journal of Coastal Research*, *65*(sp1), 678-683.

Churchill, D. D., Houston, S. H., & Bond, N. A. (1995). The Daytona Beach Wave of 3-4 July 1992: a shallow-water gravity wave forced by a propagating squall line. *Bulletin of the American Meteorological Society*, *76*(1), 21-32.

Donn, W. L. (1959). The Great Lakes storm surge of May 5, 1952. *Journal of Geophysical Research*, *64*(2), 191-198.

Dragani, W. C., D'Onofrio, E. E., Grismeyer, W., Fiore, M. M., & Campos, M. I. (2009). Atmospherically-induced water oscillations detected in the Port of Quequén, Buenos Aires, Argentina. *Physics and Chemistry of the Earth, Parts A/B/C*, *34*(17), 998-1008.

Ewing, M., Press, F., & Donn, W. L. (1954). An explanation of the Lake Michigan wave of 26 June 1954. *Science*, *120*(3122), 684-686.

Eze, C. L., Uko, D. E., Gobo, A. E. T., Sigalo, F. B., & Israel-Cookey, C. (2009). Mathematical Evaluation of Tsunami Propagation. *Research Journal of Applied Sciences*, *4*(6), 213-216.

Greenspan, H. P. (1956). The generation of edge waves by moving pressure distributions. *Journal of Fluid Mechanics*, *1*(06), 574-592.

Hibiya, T., & Kajiura, K. (1982). Origin of theAbiki phenomenon (a kind of seiche) in Nagasaki Bay. *Journal of the Oceanographical Society of Japan*,*38*(3), 172-182.

Imamura, F. (1996). *Review of Tsunami Simulation with a Finite Difference Method*, Long-Wave Runup Models, Proceedings of the International Workshop, Friday Harbour, 153 USA, 12-17 September 1995 by World Scientific Publishing Co Pte Ltd., Eds. Yeh, H., Liu, P. and Synolakis, C., pp. 25-42

Imamura, F., Yalciner, A. C., & Ozyurt, G. (2006). Tsunami modelling manual. *UNESCO IOC international training course on Tsunami Numerical Modelling*.

Kian, R., Yalciner, A. C., & Zaytsev, A. (2014). Evaluating the performance of tsunami propagation models. *Bauhaus summer school in Forecast Engineering, Weimar, Germany*, 17-29.

Kian, R., Yalciner, A.C., Zaytsev, A., & Aytore, B. (2015, April). Tsunami Induced Resonance in Enclosed Basins; Case Study of Haydarpasa Port In Istanbul. In *EGU General Assembly Conference Abstracts* (Vol. 17, p. 154).

Kirby, J. T., Wei, G., Chen, Q., Kennedy, A. B., & Dalrymple, R. A. (1998).*FUNWAVE 1.0: fully nonlinear Boussinesq wave model-Documentation and user's manual*. University of Delaware.

Lipa, B., Parikh, H., Barrick, D., Roarty, H., & Glenn, S. (2014). High-frequency radar observations of the June 2013 US East Coast meteotsunami. *Natural hazards*, *74*(1), 109-122.

Liu, P. L.-F., Cho, Y.-S. Yoon, S.B., Seo. S.N. (1994). Numerical Simulations of the 1960 Chilean Tsunami Propagation and Inundation at Hilo, Hawaii, Recent Development in Tsunami Research, pages 99–115, Kluwer Academic Publishers, 1994.

Liu, P. L.-F., Woo, S-B., Cho, Y.-S. (1998). *Computer Programs for Tsunami Propagation and Inundation*, Technical report, Cornell University, 1998

Marcos, M., Monserrat, S., Medina, R., & Vidal, C. (2003). Influence of the atmospheric wave velocity in the coastal amplification of meteotsunamis. In*Submarine Landslides and Tsunamis* (pp. 243-249). Springer Netherlands.

Mellor, G. L. (1991). An equation of state for numerical models of oceans and estuaries. *Journal of Atmospheric and Oceanic Technology*, *8*(4), 609-611.

Mercer, D., Sheng, J., Greatbatch, R. J., & Bobanović, J. (2002). Barotropic waves generated by storms moving rapidly over shallow water. *Journal of Geophysical Research: Oceans*, *107*(C10).

Metin, A.D., Pelinovsky, E., Zaytsev, A., Ozyurt Tarakcioglu, G., & Yalciner, A.C. (2016). Behavior and Amplification of Long Waves Generated by Atmospheric Pressure Disturbances. (pp. 185-186). In *Türkiye Deniz Bilimleri Konferansı*, 31May-3Jun 2016, Ankara.

Metin, A.D., Yalciner, A.C., Ozyurt Tarakcioglu, G., & Zaytsev, A. (2015). Generation and Propagation of Long Waves due to Spatial and Temporal Pressure Distributions. In *2015 AGU Fall Meeting*. Agu.

Monserrat, S., & Rabinovich, A. B. (2006). Meteotsunamis: atmospherically induced destructive ocean waves in the tsunami frequency band. *Natural Hazards and Earth System Science*, *6*(6), 1035-1051.

Monserrat, S., Ibbetson, A., & Thorpe, A. J. (1991). Atmospheric gravity waves and the 'rissaga'phenomenon. *Quarterly Journal of the Royal Meteorological Society*, *117*(499), 553-570.

Monserrat, S., Vilibić, I., Rabinovich, A. B. Meteotsunamis: atmospherically induced destructive ocean waves in the tsunami frequency band: Natural Hazards and Earth System Science, Copernicus Publications on behalf of the European Geosciences Union, 2006, 6 (6), pp.1035- 1051. <hal-00299394>

Munk, W., Snodgrass, F., & Carrier, G. (1956). Edge waves on the continental shelf. *Science*, *123*(3187), 127-132.

NAMI DANCE Manual (2010). Developed by Zaytsev, C., Yalciner, Pelinovsky, Kurkin. Tsunami Simulation/Visualization Code NAMI DANCE versions 4.9. http://www.namidance.ce.metu.edu.tr

Papadopoulos, G. A. (1993). On some exceptional seismic (?) sea-waves in the Greek archipelago. *Science of Tsunami Hazards, 11*, 25-34.

Park, Y. H. (1986). Water characteristics and movements of the Yellow Sea Warm Current in summer. *Progress in Oceanography*, *17*(3), 243-254.

Pasquet, S., & Vilibić, I. (2013). Shelf edge reflection of atmospherically generated long ocean waves along the central US East Coast. *Continental Shelf Research*, *66*, 1-8.

Pattiaratchi, C. B., & Wijeratne, E. M. S. (2015). Are meteotsunamis an underrated hazard?. *Phil. Trans. R. Soc. A*, *373*(2053), 20140377.

Paxton, C. H., & Sobien, D. A. (1998). Resonant interaction between an atmospheric gravity wave and shallow water wave along Florida's west coast. *Bulletin of the American Meteorological Society*, *79*(12), 2727-2732.

Proudman, J. (1929). The Effects on the Sea of Changes in Atmospheric Pressure. *Geophysical Journal International*, *2*(s4), 197-209.

Rabinovich, A. B. (2009). Seiches and harbor oscillations. *Handbook of coastal and ocean engineering*, 193-236.

Rabinovich, A. B., & Monserrat, S. (1996). Meteorological tsunamis near the Balearic and Kuril Islands: descriptive and statistical analysis. *Natural Hazards*, *13*(1), 55-90.

Ranguelov, B., Tinti, S., Pagnoni, G., Tonini, R., Zaniboni, F., & Armigliato, A. (2008). The nonseismic tsunami observed in the Bulgarian Black Sea on 7 May 2007: was it due to a submarine landslide?. *Geophysical Research Letters*, *35*(18).

Sallenger Jr, A. H., List, J. H., Gelfenbaum, G., Stumpf, R. P., & Hansen, M. (1995). Large wave at Daytona Beach, Florida, explained as a squall-line surge. *Journal of Coastal Research*, 1383-1388.

Šepić, J., Međugorac, I., Janeković, I., Dunić, N., & Vilibić, I. (2016). Multi-Meteotsunami Event in the Adriatic Sea Generated by Atmospheric Disturbances of 25–26 June 2014. *Pure and Applied Geophysics*, 1-22.

Šepić, J., Vilibić, I., & Belušić, D. (2009). Source of the 2007 Ist meteotsunami (Adriatic Sea). *Journal of Geophysical Research: Oceans*,*114*(C3).

Šepić, J., Vilibić, I., & Strelec Mahović, N. (2012). Northern Adriatic meteorological tsunamis: observations, link to the atmosphere, and predictability. *Journal of Geophysical Research: Oceans*, *117*(C2).

Šepić, J., Vilibić, I., Rabinovich, A. B., & Monserrat, S. (2015). Widespread tsunami-like waves of 23-27 June in the Mediterranean and Black Seas generated by high-altitude atmospheric forcing. *Scientific reports*, *5*.

Skamarock, W. C., Klemp, J. B., Dudhia, J., Gill, D. O., Barker, D. M., Wang, W., & Powers, J. G. (2005). *A description of the advanced research WRF version 2* (No. NCAR/TN-468+ STR). National Center For Atmospheric Research Boulder Co Mesoscale and Microscale Meteorology Div.

Tanaka, K. (2010). Atmospheric pressure-wave bands around a cold front resulted in a meteotsunami in the East China Sea in February 2009. *Nat Hazards Earth Syst Sci*, *10*, 2599-2610.

Titov, V.V. and Synolakis, C.E. (1998). *Numerical modeling of tidal wave run-up*, Journal of Waterway, Port, Coastal and Ocean Engineering, Vol. 124 (4), pp. 157-171.

Vilibić, I., & Šepić, J. (2009). Destructive meteotsunamis along the eastern Adriatic coast: overview. *Physics and Chemistry of the Earth, Parts A/B/C,34*(17), 904-917.

Vilibić, I., Monserrat, S., Rabinovich, A., & Mihanović, H. (2008). Numerical modelling of the destructive meteotsunami of 15 June, 2006 on the coast of the Balearic Islands. *Pure and Applied geophysics*, *165*(11-12), 2169-2195.

Vilibić, I., Šepić, J., Ranguelov, B., Mahović, N. S., & Tinti, S. (2010). Possible atmospheric origin of the 7 May 2007 western Black Sea shelf tsunami event. *Journal of Geophysical Research: Oceans*, *115*(C7).

Vučetić, T., Vilibić, I., Tinti, S., & Maramai, A. (2009). The Great Adriatic flood of 21 June 1978 revisited: An overview of the reports. *Physics and Chemistry of the Earth, Parts A/B/C*, *34*(17), 894-903.

Wang, X., Li, K., Yu, Z., & Wu, J. (1987). Statistical characteristics of seiches in Longkou Harbour. *Journal of physical oceanography*, *17*(7), 1063-1065.

Watts, P., Grilli, S. T., Kirby, J. T., Fryer, G. J., & Tappin, D. R. (2003). Landslide tsunami case studies using a Boussinesq model and a fully nonlinear tsunami generation model. *Natural Hazards And Earth System Science*, *3*(5), 391-402.

Wu, T. Y. (1981). Long waves in ocean and coastal waters. *Journal of Engineering Mechanics*, *107*(EM3), 501-522.

Yalciner, A. C., Kian, R., Aytore, B., & Zaytsev, A. (2015). Harbors and Tsunami Threat; A case study in the Sea of Marmara. *E-proceedings of the 36th IAHR World Congress 28 June – 3 July, 2015, The Hague, the Netherlands*

Zhang, Y. J., Ye, F., Stanev, E. V., & Grashorn, S. (2016). Seamless cross-scale modeling with SCHISM. *Ocean Modelling*, *102*, 64-81.

APPENDIX A

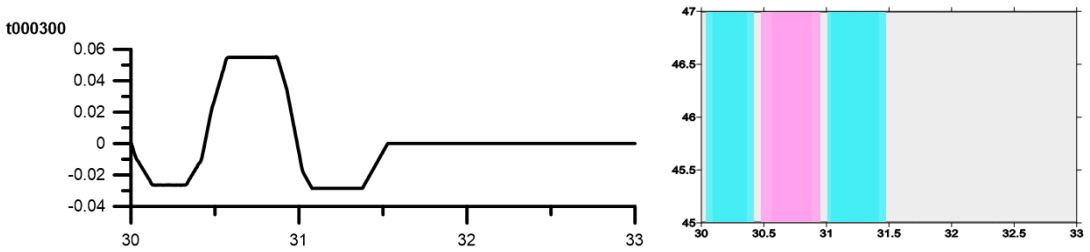

Figure A.1. Top and Sectional View of Water Elevation on Flat Bathymetry at 5 minutes for Case 1 (V=200 m/Sec and c=70 m/sec)

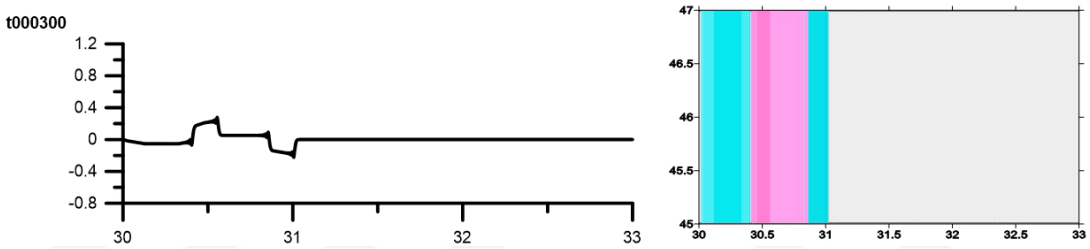

Figure A.2. Top and Sectional View of Water Elevation on Flat Bathymetry at 5 minutes for Case 2 (V=70 m/Sec and c=70 m/sec)

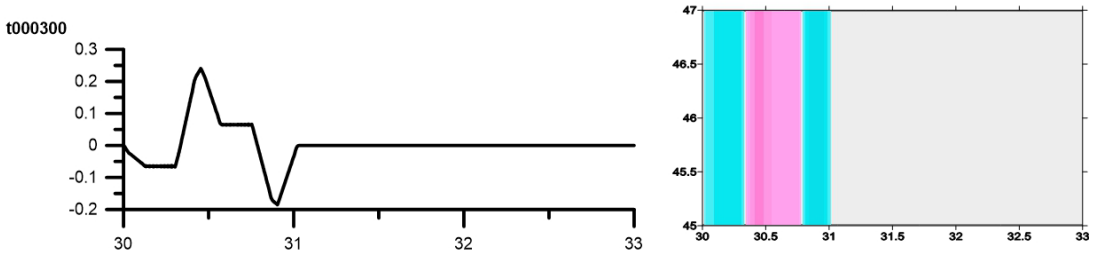

Figure A.3. Top and Sectional View of Water Elevation on Flat Bathymetry at 5 minutes for Case 3 (V=40 m/Sec and c=70 m/sec)

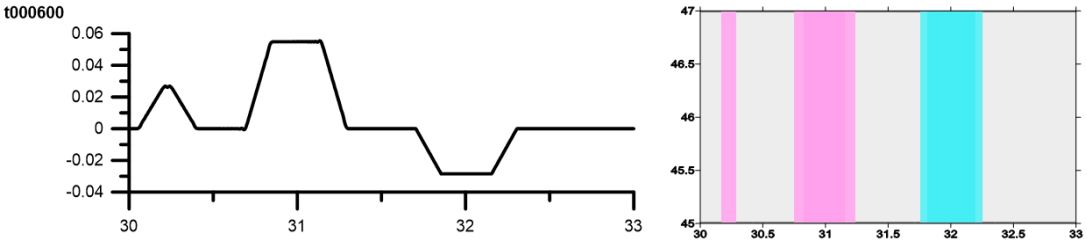

Figure A.4. Top and Sectional View of Water Elevation on Flat Bathymetry at 10 minutes for Case 1 (V=200 m/Sec and c=70 m/sec)

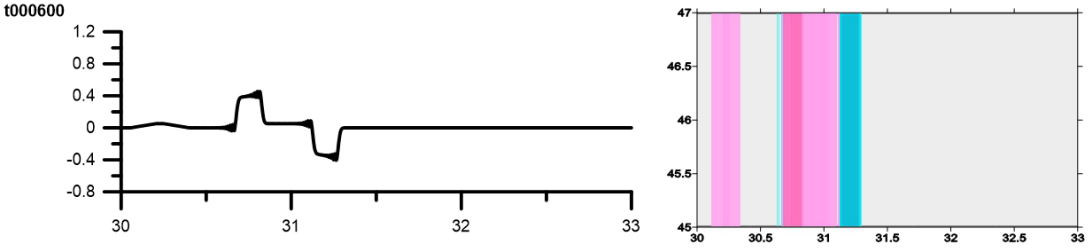

Figure A.5. Top and Sectional View of Water Elevation on Flat Bathymetry at 10 minutes for Case 2 (V=70 m/Sec and c=70 m/sec)

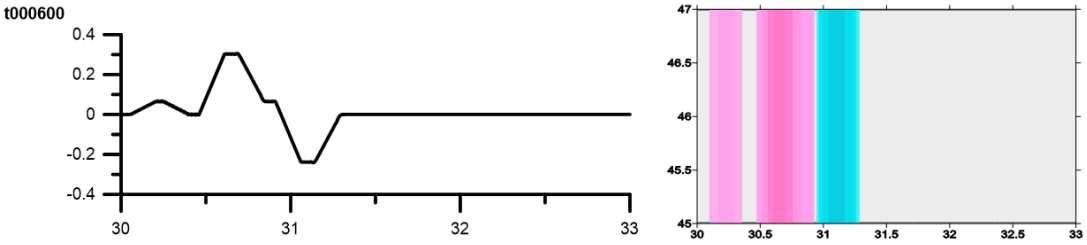

Figure A.6. Top and Sectional View of Water Elevation on Flat Bathymetry at 10 minutes for Case 3 (V=40 m/Sec and c=70 m/sec)

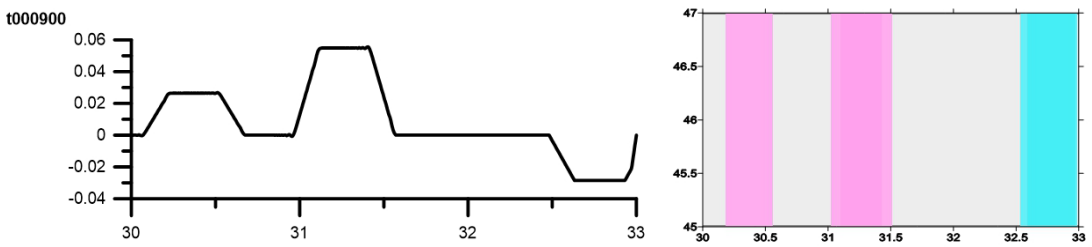

Figure A.7. Top and Sectional View of Water Elevation on Flat Bathymetry at 15 minutes for Case 1 (V=200 m/Sec and c=70 m/sec)

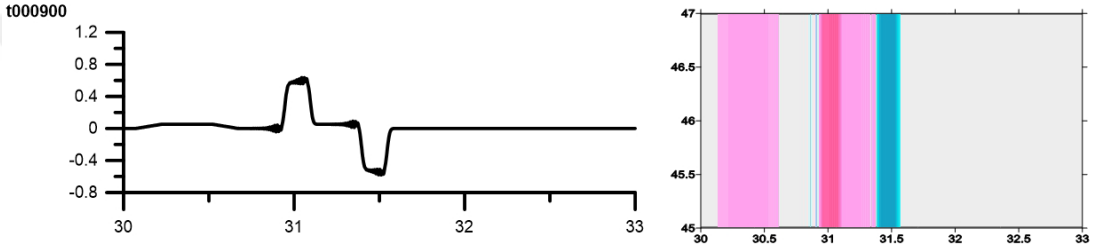

Figure A.8. Top and Sectional View of Water Elevation on Flat Bathymetry at 15 minutes for Case 2 (V=70 m/Sec and c=70 m/sec)

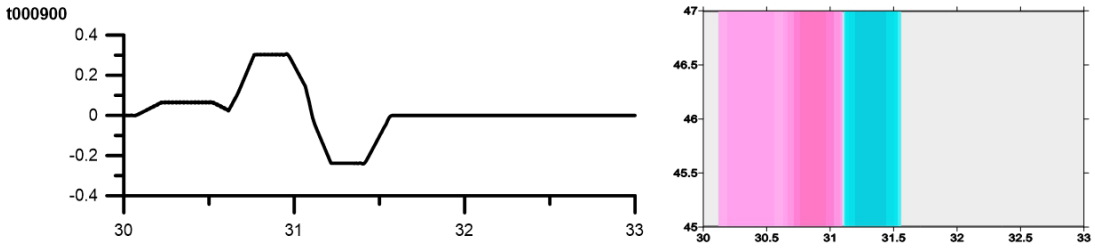

Figure A.9. Top and Sectional View of Water Elevation on Flat Bathymetry at 15 minutes for Case 3 (V=40 m/Sec and c=70 m/sec)

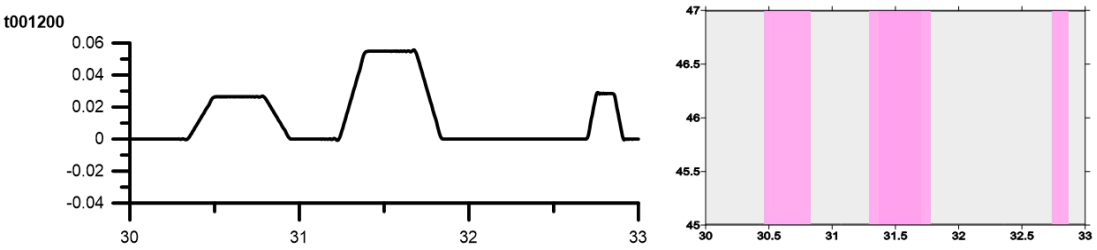

Figure A.10. Top and Sectional View of Water Elevation on Flat Bathymetry at 20 minutes for Case 1 (V=200 m/Sec and c=70 m/sec)

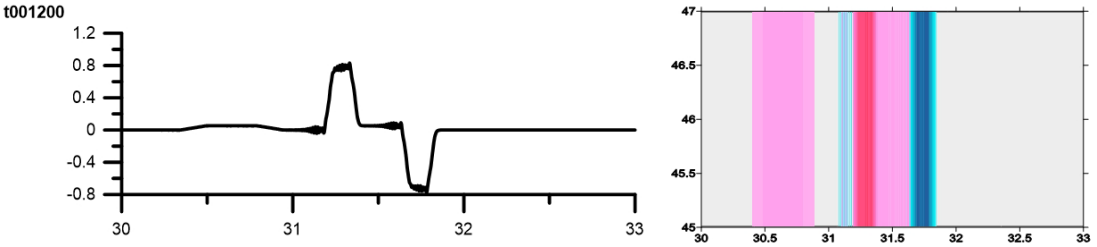

Figure A.11. Top and Sectional View of Water Elevation on Flat Bathymetry at 20 minutes for Case 2 (V=70 m/Sec and c=70 m/sec)

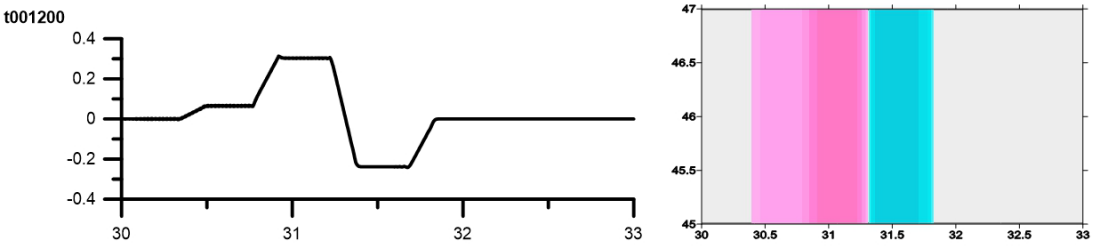

Figure A.12. Top and Sectional View of Water Elevation on Flat Bathymetry at 20 minutes for Case 3 (V=40 m/Sec and c=70 m/sec)